# Fluid Mechanics of Intrathecal Drug Delivery

THÈSE N$^{O}$ 4061 (2008)

PRÉSENTÉE LE 27 JUIN 2008
À LA FACULTÉ DES SCIENCES ET TECHNIQUES DE L'INGÉNIEUR
LABORATOIRE DE MÉCANIQUE DES FLUIDES
PROGRAMME DOCTORAL EN MÉCANIQUE

ÉCOLE POLYTECHNIQUE FÉDÉRALE DE LAUSANNE

POUR L'OBTENTION DU GRADE DE DOCTEUR ÈS SCIENCES

PAR

Radboud Michael NELISSEN

M.Sc. in applied physics, University of Twente, Enschede, Pays-Bas
et de nationalité néerlandaise

acceptée sur proposition du jury:

Prof. D. Favrat, président du jury
Prof. P. Monkewitz, Dr N. Borhani, directeurs de thèse
Prof. E. Buchser, rapporteur
Prof. D. Poulikakos, rapporteur
Prof. M. Swartz, rapporteur

ÉCOLE POLYTECHNIQUE
FÉDÉRALE DE LAUSANNE
Suisse
2008

# Acknowledgements

This thesis would not have been possible without the funding of CTI Medtech, Medtronic Europe SA, and the help of many. I would like to thank Peter Monkewitz for giving me the freedom and the means to explore my subject, whilst gently pushing me in the right direction. I owe gratitude to Navid Borhani for the many brainstorming sessions which were instrumental in designing my experiment as well as for his critical evaluation of the presentations that I did. I would especially like to thank Eric Buchser who besides initiating the project has generated considerable interest in the clinical world. It was always a pleasure to go to the Morges hospital and discuss progress and new ideas. I would also like to thank the defense committee members, namely prof. Melody Swartz and prof. Dimos Poulikakos, for the pleasant discussion and good ideas.

Trong-Vien Truong has helped me tremendously by making the CAD drawings of my experiment and advising on experimental techniques. I want to thank the students that were involved in this project, especially Friedemann for his dedication when my own deadlines were fast approaching. My experiment was manufactured to the highest standards thanks to the many people at our institute's machine shop. I especially thank Bernard Savary and Marc Salle for making pieces, giving ideas, correcting my errors, and accepting the occasional 'need-that-yesterday' rush jobs. I would also like to thank Eva Gasser for her kind help with all things administrative.

I have sometimes experienced my thesis as a solitary exercise, but only in the late hours of the evening or during the weekend when Andrew, Chris, David, Etienne, Flavio, Marc-Antoine, Orestis, Richard, and Roland were doing the laundry or "working at home". I'll miss the banana/M&M's/squash/coffee/beer breaks. I am not sure we have made this world a better place with our regular discussions on the pretty pictures in the morning newspapers, but at least we tried. Emeric, I can't wait to receive the 49%, even though I know it won't come close to covering my own debt. Anyway, we would have made a great couple!

Mam, pap, Ljiljana, André, Wyke, Hiske, Harald, Wouter, and other friends who I have not mentioned explicitly, your encouragement and support is very dear to me. I feel privileged and lucky to be able to count on you. Sanja, there are many ways to beat around the bush (and unfortunately for you I know them all), but this thesis would not have been possible without you. Je t'aime fort, enfin, quand même!

# Abstract

The aim of this principally experimental study is to understand from fluid mechanic principles why an insignificant anesthetic dose administered as a short bolus into the cerebrospinal fluid inside the subarachnoid space provides greater pain relief than a larger dose continuously injected over a longer period. The subarachnoid space is modeled as an annular gap of constant or slowly varying cross section into which a catheter is introduced. The cerebrospinal fluid is replaced by water of 37°C which has very similar properties. This fluid in the annular gap is subjected to oscillations of amplitude and frequency (heart frequency) typically found in the subarachnoid space. The anesthetic is replaced by a fluorescent dye injected through the catheter. To study its dispersion, we have developed a 400 Hz laser scanning setup with which we perform quasi-instantaneous, quantitative 3D laser induced fluorescence (LIF) as well as 2D particle image velocimetry (PIV). The experiments are supplemented by an analytical axi-symmetric model as well as an exploratory numerical model to help interpret the results. The study has identified steady streaming (a nonlinear effect associated with the fluid oscillation) and enhanced diffusion (an effect associated with oscillating shear flow) as the principal agents of dye (anesthetic) dispersion. Besides the slowly varying cross section, the catheter tip has been identified as an important cause for steady streaming. In an attempt to identify optimal injection parameters of use for clinicians, a rough parametric model of the primary factors influencing drug spread (fluid oscillation frequency and amplitude, geometry, and injection rate) has been constructed.

**Keywords**: intrathecal drug delivery; injection rate; enhanced diffusion; steady streaming; laser induced fluorescence; particle image velocimetry.

# Version abrégée

Le but de cette étude, principalement expérimentale, est de comprendre pourquoi une très faible dose d'anesthésique administrée en un rapide bolus dans le liquide céphalo-rachidien produit une plus grande diminution de la douleur qu'une dose plus importante administrée sur une plus longue période. L'espace sous-arachnoïde est modélisé par un volume annulaire de section transversale constante ou variant lentement dans lequel on a introduit un cathéter. Le liquide céphalo-rachidien est remplacé par de l'eau à 37°C qui possède des propriétés similaires. Ce fluide est soumis à des oscillations d'amplitude et de fréquence comparables à celles rencontrées dans l'espace sous-arachnoïde. L'anesthésique est, quant à lui, remplacé par un colorant fluorescent injecté dans le modèle par le cathéter. Pour étudier la dispersion, un système de balayage laser fonctionnant a 400 Hz a été mis en place afin de réaliser une étude quantitative tridimensionnelle quasi-instantanée par fluorescence induite par laser (LIF) ainsi qu'une étude bidimensionnelle par vélocimétrie d'image de particules (PIV). Ces mesures expérimentales sont complétées par une modélisation analytique du cas axisymétrique ainsi que par un modèle numérique préliminaire afin d'appuyer l'interprétation des résultats. L'étude a mis en évidence un écoulement redressé ou "steady streaming" (effet non linéaire associé avec les oscillations du fluide) ainsi qu'une diffusion augmentée ou "enhanced diffusion" (effet associé au cisaillement dans un écoulement oscillant) comme étant les deux principaux agents responsables de la dispersion du colorant (i.e. de l'anesthésique). En plus de la variation lente de la section transversale, l'extrémité du cathéter a été identifiée comme une cause importante de l'apparition de l'écoulement redressé. Dans le but d'identifier les paramètres d'injection optimaux pour une utilisation clinique, un modèle paramétrique préliminaire basé sur les principaux facteurs a été établi. Les facteurs déterminant la dispersion de l'anesthésique sont la fréquence et l'amplitude des oscillations du fluide, la géométrie locale et le taux d'injection.

**Mots clés**: administration intrathécale; taux d'injection; diffusion augmentée; écoulement redressé; fluorescence induite par laser; vélocimétrie d'image de particules.

# Contents

**Abstract** iii

**Version abrégée** v

**Contents** ix

**List of Figures** xiii

**List of Tables** xv

**1 Introduction to Intrathecal Drug Delivery** 1
1.1 Intrathecal Drug Delivery . . . 1
1.2 Literature on ITDD . . . 2
1.3 Research Questions . . . 3
1.4 Scope . . . 4

**2 Clinical trial** 7
2.1 Introduction . . . 7
2.2 Patients and methods . . . 8
2.3 Results . . . 10
  2.3.1 VAS Measurements . . . 10
  2.3.2 Dermatome Measurements . . . 10
  2.3.3 Cardiovascular and Respiratory Changes . . . 11
2.4 Discussion . . . 12
2.5 Conclusion . . . 14

**3 Dispersion Mechanisms in ITDD** 17
3.1 Cerebrospinal Fluid (CSF) Oscillation . . . 17
3.2 Geometry of the Subarachnoid Space . . . 18
3.3 Molecular Diffusion . . . 19
3.4 Enhanced Diffusion . . . 20
3.5 Steady Streaming . . . 24
3.6 Injection Jet . . . 25
3.7 Drug Buoyancy . . . 25
3.8 Absorption into the Spinal Cord . . . 26
3.9 Summary . . . 27

**4 Setup** 29
4.1 Model and Material . . . 29
4.2 Optical Scanning System . . . 31

**I Steady Streaming in ITDD** **35**

**5 Introduction** **37**

**6 Steady Streaming Theory** **39**
6.1 Introduction . . . . . 39
6.2 Annular Gap with Slowly Varying Cross Section . . . . . 40
6.3 Key Features of Axi-symmetric Steady Streaming . . . . . 42

**7 Numerical Investigation of Steady Streaming** **45**
7.1 Introduction . . . . . 45
7.2 Case I: Straight Annular Gap with Injection Catheter . . . . . 45
7.3 Case II: Geometry From Visible Human Database . . . . . 46
7.4 Numerical Method and Validation . . . . . 47
7.5 Results: Case I . . . . . 48
7.6 Results: Case II . . . . . 51
7.7 Summary of the Numerical Study . . . . . 55

**8 Experimental Investigation of Steady Streaming** **57**
8.1 Notes on the Setup . . . . . 57
8.2 Procedure . . . . . 58
8.3 PIV Results . . . . . 59
8.4 Summary of the PIV study . . . . . 63

**9 Conclusions** **65**

**II Mixing phenomena in ITDD** **67**

**10 Introduction** **69**

**11 Quantitative LIF** **71**
11.1 Introduction . . . . . 71
11.2 Setup . . . . . 71
11.3 Corrections for Image Distortions . . . . . 72
11.3.1 Lens Aberrations . . . . . 72
11.3.2 Image Distortions . . . . . 74
11.3.3 Scanner Speed $\dot{\xi}$ . . . . . 75
11.4 Complex LIF Behavior . . . . . 76
11.4.1 Collisional Quenching . . . . . 76
11.4.2 Static Quenching . . . . . 77
11.4.3 Laser Beam Scattering . . . . . 79
11.5 Calibration Measurements . . . . . 81
11.5.1 Procedure . . . . . 81
11.5.2 Amplitude Dependence . . . . . 81
11.5.3 Absorption . . . . . 82
11.5.4 Error Analysis . . . . . 82

11.6 Increasing Dynamic Range . . . . 84
11.7 Summary . . . . 84

**12 Experimental Investigation of Mixing in ITDD 87**
12.1 Introduction . . . . 87
12.2 Procedure . . . . 88
12.3 Analysis . . . . 90
  12.3.1 Parametric Modeling . . . . 90
  12.3.2 Data Reduction . . . . 92
12.4 Straight Tube and Catheter . . . . 93
  12.4.1 Qualitative Observations . . . . 93
  12.4.2 Bulk movement . . . . 94
12.5 Mixing Parameter $\Phi$ . . . . 96
12.6 Varying Outer Wall and Catheter . . . . 98
12.7 Axial Spread $\bar{C}(z,t)$ . . . . 103
  12.7.1 Qualitative Observations . . . . 104
  12.7.2 Influence of Characteristic Length $L$ and Catheter Position . . . . 104
  12.7.3 Influence of the amplitude of the varying cross section $\Delta r_o$ . . . . 105
  12.7.4 Measured Diffusion Coefficient $D_{\text{exp}}$ . . . . 105
12.8 The Dye's Envelope . . . . 108
  12.8.1 Dispersion Above the Catheter Tip . . . . 109
  12.8.2 Growth Rate of the Envelope . . . . 111
12.9 Total Measured Mass in the Control Volume $m_{\text{CV}}$ . . . . 112
  12.9.1 The Influence of the Detection Threshold . . . . 112
  12.9.2 Primary Effect of $A_{\text{osc}}$ on $m_{\text{CV}}$ . . . . 112
  12.9.3 Primary Influence of $f_{\text{osc}}$ on $m_{\text{CV}}$ . . . . 113
  12.9.4 Primary Influence of $Q_{\text{inj}}$ on $m_{\text{CV}}$ . . . . 114
  12.9.5 Primary Influence of $\epsilon$ on $m_{\text{CV}}$ . . . . 114
  12.9.6 The Maximum of $m_{\text{CV}}$ . . . . 117
  12.9.7 Factors Influencing $\dot{m}_{\text{CV}}$ During Injection . . . . 117
  12.9.8 The Decay of $m_{\text{CV}}$ after Injection . . . . 118
12.10 Qualitative Observations Regarding Buoyancy . . . . 119
12.11 Summary of Experimental Observations . . . . 119

**13 Conclusions 123**

**Nomenclature 127**

**Bibliography 133**

**Curriculum Vitae 138**

# List of Figures

1.1 Two examples of human granulomas. . . . . . . . . . . . . . . . . . . . . . . 2
1.2 The limited distribution of injected dye in a pig spinal cord. . . . . . . . . 3

2.1 Histogram of the position of the catheter tip . . . . . . . . . . . . . . . . . . 8
2.2 Protocol of the clinical trial. . . . . . . . . . . . . . . . . . . . . . . . . . . 9
2.3 The time evolution of the normalized mean VAS score. . . . . . . . . . . . 11
2.4 Histogram of the lowest and the highest dermatome measured at any time during the trials. . . . . . . . . . . . . . . . . . . . . . . . . . . . . . . . . 12
2.5 A histogram of the average position of the highest and lowest dermatome measured at any point during the trial. . . . . . . . . . . . . . . . . . . . 12
2.6 Histogram of the difference between the highest and lowest measured dermatome. . . . . . . . . . . . . . . . . . . . . . . . . . . . . . . . . . . . . 13

3.1 Cross sections of the human spinal canal from the Visible Human Database. 18
3.2 A dissection image of the human spinal canal. . . . . . . . . . . . . . . . . 19
3.3 An illustration of enhanced diffusion in oscillatory flow. . . . . . . . . . . . 21
3.4 The relative increase of diffusion $\overline{D_{\text{enh}}}(t)/D$ vs. $d_{\text{osc}}$ and $f_{\text{osc}}$. . . . . . . . . 24

4.1 Schematic of the experimental setup. . . . . . . . . . . . . . . . . . . . . . 29
4.2 The coordinate system used throughout this work. . . . . . . . . . . . . . . 30
4.3 A schematic of a constricted varying cross section annular gap. . . . . . . . 31
4.4 Typical oscillatory waveforms. . . . . . . . . . . . . . . . . . . . . . . . . . 32
4.5 The injection direction $\varphi$ in two experimental configurations. . . . . . . . . 32
4.6 Schematic of the method to create a laser sheet with rotating mirrors. . . . 33

6.2 Characteristic steady streaming in an annular gap with a slowly varying outer wall shown with a vector plot of $\mathbf{v_s}(r, z)$, and contours of the stream function $\Psi_s$. . . . . . . . . . . . . . . . . . . . . . . . . . . . . . . . . . 43
6.3 The steady streaming velocity $w_s$ vs. $r$ at $\hat{z} = L_c/2$ inside an annular gap with a sinusoidally varying outer wall for different values of $\epsilon$. . . . . . . 44
6.4 $\max(w_s)$ for different values of $\alpha$ and $A_{\text{osc}}$. . . . . . . . . . . . . . . . . 44

7.1 The extracted human-like geometry that was used for the numerical computation shown inside the spinal canal. . . . . . . . . . . . . . . . . . . . . 46
7.2 The computational grid for the human-like geometry. . . . . . . . . . . . . 47
7.3 Comparison of numerically calculated velocity profiles with the Stokes solution for annular gap flow. . . . . . . . . . . . . . . . . . . . . . . . . . . 48
7.4 A vector plot of $\bar{\mathbf{v}}$ in the planes $(r = 2, \theta, z)$, and $(r, \theta = 0, z)$. . . . . . . 49
7.5 A contour plot of $|\bar{\mathbf{v}}|$ in the planes $(r = 2, \theta, z)$, and $(r, \theta = 0, z)$. . . . . . 50
7.6 A contour plot of $|\mathbf{v}_{\text{rms}}|$ in the planes $(r = 2, \theta, z)$, and $(r, \theta = 0, z)$. . . . . 50

7.7 The computational grids of the top surface of the human-like geometry and the standard straight annular gap used in experiments. . . . . . . . . . 51
7.8 $|\mathbf{v}_{\mathrm{rms}}|$ of the non-singly harmonic human waveform on several cross sections extracted from the human-like geometry and inside an annular gap of similar dimensions as our experimental setup. . . . . . . . . . . . . . . . 52
7.9 Characteristic velocities in a plane ($\mathrm{P}_4$) extracted from the human-like geometry. . . . . . . . . . . . . . . . . . . . . . . . . . . . . . . . . . . . 53
7.10 Characteristic velocities in a plane ($\mathrm{P}_3$) extracted from the human-like geometry. . . . . . . . . . . . . . . . . . . . . . . . . . . . . . . . . . . . 54

8.1 The experimentally measured $|\mathbf{v}_{\mathrm{rms}}|$ vs. $r$ for several oscillatory waveforms. 59
8.2 The measured axial steady streaming velocity $w_s = \hat{w}_s/(\omega d_{\mathrm{osc}}\gamma)$ vs. $r$ for 4 different values of $\epsilon$ compared with asymptotic theory. . . . . . . . . . . 60
8.3 The magnitude of the measured steady streaming $|\mathbf{v}_\mathbf{s}|$ in several slowly varying cross section annular gaps, with and without the injection catheter. 61
8.4 The axial steady streaming component $w_s$ around the catheter tip for 3 different values of $\theta$ and 2 different values of $\epsilon$. . . . . . . . . . . . . . . . . 62

11.1 Optical setup used for calibration measurements. . . . . . . . . . . . . . . 72
11.2 Zernike correction of lens aberrations. . . . . . . . . . . . . . . . . . . . . . 73
11.3 The optical effect of the inner cylinder on concentration measurements. . . 74
11.4 The intensity profile across the image planes ($\mathbf{e}_x$). . . . . . . . . . . . . . 75
11.5 The error due to rotating mirror acceleration. . . . . . . . . . . . . . . . . 76
11.6 The effect of static quenching on the mean fluorescent intensity vs. $t$. . . . 78
11.7 Transverse intensity profile of a stationary laser beam in fluorescein. . . . . 80
11.8 The standard deviation ($\sigma$) of the normalized beam signature vs. $z$. . . . . 80
11.9 Beam width of the normalized intensity profile for different $C$ and laser power $P_0$. . . . . . . . . . . . . . . . . . . . . . . . . . . . . . . . . . . . . 81
11.10 The fluorescein signal vs. $C$ and $P_0$ . . . . . . . . . . . . . . . . . . . . . . 82
11.11 The attenuation constant $a$ vs. concentration $C$. . . . . . . . . . . . . . . 83

12.1 Illustration of the method of presenting the parametric models. . . . . . . 91
12.2 $(\theta, z)$-projections of dye dispersion after an injection with the metal injection catheter oriented at 2 different $\varphi$. . . . . . . . . . . . . . . . . . . . . 93
12.3 $(\theta, z)$-projections of dye dispersion after an injection with the Medtronic silicone injection catheter oriented at 2 different $\varphi$. . . . . . . . . . . . . 94
12.4 The axial position of the center of gravity of the dye $z_{\mathrm{g}}$, and the parametric model for the mean axial position of the dye. . . . . . . . . . . . . . . . . . . 95
12.5 The parametric model for the ratio of the mean top and bottom disappearance rates computed with a simple bin model. . . . . . . . . . . . . . . 96
12.6 Three typical curves of $\Phi$ vs. t. . . . . . . . . . . . . . . . . . . . . . . . . 97
12.7 Parametric models for $\min(\Phi)$, and $\Phi(t = 1500\mathrm{s})$. . . . . . . . . . . . . . 97
12.8 $(\theta, z)$-projections of dye dispersion after an injection with the metallic injection catheter placed near a constricted outer wall. . . . . . . . . . . . 99
12.9 Single plane $(r, \theta = 0, z)$ concentration measurements above the injection catheter in a constant cross section geometry. . . . . . . . . . . . . . . . 100

12.10 Single plane $(r, \theta = 0, z)$ concentration measurements above the injection catheter in a constricted geometry. . . . . . . . . . . . . . . . . . . . . . . . 101

12.11 Single plane $(r, \theta = 0, z)$ concentration measurements above the injection catheter in an expanded geometry. . . . . . . . . . . . . . . . . . . . . . . . 102

12.12 $\bar{C}(z,t)$ of a single fast bolus injected with a metal, or silicone catheter inside a constant cross section annular gap. . . . . . . . . . . . . . . . . . 104

12.13 $\bar{C}(z,t)$ of a single fast ($Q_{\text{inj}} = 0.4\ \mu$l/s) bolus injected with a metal catheter placed inside 2 constricted annular gaps with different $\epsilon$. . . . . . . . . . . 106

12.14 $\bar{C}(z,t)$ of a single fast bolus injected with a metal catheter inside 2 expanded annular gaps with different $\epsilon$. . . . . . . . . . . . . . . . . . . . . . . 107

12.15 $\bar{C}(z,t)$ of a single fast bolus injected with a metal catheter inside a stacked, or repetitive, expanded geometry. . . . . . . . . . . . . . . . . . . . . . 107

12.16 The computed theoretical variance $\sigma^2$ vs. t. for 1D axial diffusion in a limited size CV for different detection thresholds. . . . . . . . . . . . . . 108

12.17 Three examples of calculating an enhanced diffusion coefficient and a comparison of $D_{\text{exp}}$ with $D_{\text{enh}}$. . . . . . . . . . . . . . . . . . . . . . . . . . 109

12.18 The computed theoretical envelope of the dye vs. t. for 1D axial diffusion in a limited size CV for different detection thresholds. . . . . . . . . . . . 109

12.19 Two typical dye boundary curves as determined using the detection limit of the setup as a threshold on the axial concentration. . . . . . . . . . . . 110

12.20 The parametric models for the typical height of the envelope above the catheter tip, and the time it takes the envelope to reach a point 14 mm above the catheter tip. . . . . . . . . . . . . . . . . . . . . . . . . . . . . 110

12.21 The parametric model for the growth rate of the envelope away from the catheter tip. . . . . . . . . . . . . . . . . . . . . . . . . . . . . . . . . . 111

12.22 The theoretical variance $m_{\text{CV}}$ vs. t. for 1D axial diffusion in a limited size CV for different detection thresholds. . . . . . . . . . . . . . . . . . . . . . 112

12.23 The primary influence $A_{\text{osc}}$ on $m_{\text{CV}}$ vs. t inside a constant cross section and a slowly varying constricted cross section annular gap. . . . . . . . . 113

12.24 The primary influence $f_{\text{osc}}$ on $m_{\text{CV}}$ vs. t inside a constant cross section and a slowly varying constricted cross section annular gap. . . . . . . . . 114

12.25 The primary influence $Q_{\text{inj}}$ on $m_{\text{CV}}$ vs. t inside a constant cross section annular gap. . . . . . . . . . . . . . . . . . . . . . . . . . . . . . . . . . 115

12.26 The primary influence $\epsilon$ on $m_{\text{CV}}$ vs. t inside a slowly varying constricted cross section annular gap for high and low $Q_{\text{inj}}$. . . . . . . . . . . . . . . 115

12.27 The primary influence $\epsilon$ on $m_{\text{CV}}$ vs. t inside a slowly varying expanded cross section annular gap for high and low $Q_{\text{inj}}$. . . . . . . . . . . . . . . 116

12.28 The average effect of $L$ of the varying cross section annular gap on the dispersion. . . . . . . . . . . . . . . . . . . . . . . . . . . . . . . . . . . 116

12.29 The parametric models for max($m_{\text{CV}}$) and the linear slope of $m_{\text{CV}}$ during injection. . . . . . . . . . . . . . . . . . . . . . . . . . . . . . . . . . 117

12.30 The parametric model for the decay of $m_{\text{CV}}$ after the injection. . . . . . 118

12.31 Qualitative observations regarding the influence of 0.3% (mass) glucose on the dispersion of dye. . . . . . . . . . . . . . . . . . . . . . . . . . . . 120

# List of Tables

2.1 Patient Statistics. . . . . . . . . . . . . . . . . . . . . . . . . . . . . . . . . . 8
2.2 A summary of the drug delivery used during the trials. . . . . . . . . . . . . 10
2.3 The average minimum and maximum blood pressure at any point after the bolus injection . . . . . . . . . . . . . . . . . . . . . . . . . . . . . . . . 13

11.1 Zernike model coefficients, including a 95% confidence interval. . . . . . . . 74
11.2 The measured destruction rate of fluorescein. . . . . . . . . . . . . . . . . . 78

12.1 The range of variables used for the investigation of mixing. . . . . . . . . . 89
12.2 Slowly varying cross section geometries used for LIF experiments. . . . . . . 89
12.3 The range of responses measured in the parametric models. . . . . . . . . . 121

# Chapter 1

# Introduction to Intrathecal Drug Delivery

## 1.1 Intrathecal Drug Delivery

The management of pain often involves the administration of a number of analgesic drugs. The most common route is the systemic administration, that is by mouth or by intramuscular, subcutaneous or intravenous injections. The majority of potent analgesic drugs act through the stimulation of cellular receptors that are mostly located in the central nervous system (CNS). With systemic administration, a drug is distributed throughout the body. Diffusion into the CNS is however impaired by anatomical as well as functional obstacles referred to as the blood-brain barrier (BBB). This results in a concentration gradient between the CNS and the plasma, implying that high blood levels must be achieved in order to reach appropriate concentrations in the cerebral spinal fluid (CSF). These difficulties can be bypassed by delivering the medication directly in the CSF, i.e. by intrathecal administration.

Intrathecal drug delivery (ITDD) has been used since the early 80's [16]. The basic technique has not changed much since, and ITDD has become an accepted method of controlling severe pain due to cancer, or chronic disease [49]. The doses required to obtain a given clinical effect are much lower and the adverse effects are also attenuated. In addition, intrathecal delivery permits the administration of drugs that cannot be given systemically because of metabolic or other biochemical reasons. Successful treatment requires that the drugs, often containing morphine, reach the nerves inside the spinal cord responsible for the pain signals. The action of the drugs stops or attenuates the transmission of the pain signals to the brain.

Technically, access to the CNS requires invasive procedures that are expensive and are associated with higher risks than conventional drug therapy. In concrete terms, a catheter must be placed close to the spinal cord, into the CSF, and connected to a subcutaneous pump. The catheter runs from the point of entry in the spinal canal (typically in the lower lumbar region) up to the specific level of the spinal cord the clinician wants to target. The entire system is implanted under the skin and the pump can be programmed according to the patientŠs needs, for example by changing the flow rate delivered by the device. The continuous injection rate of the pump is usually less than 1 milliliter per day. Some pumps allow patients to self-administer a small bolus injection at the rate of several milliliters per hours during a few minutes.

Although intrathecal drug delivery devices are commonly used in routine pain management, their utilization is considered only when conventional pharmacotherapy fails, either because of lack of efficacy or intractable side effects. Hence, the number of patients for whom these techniques are required is small.

## 1.2 Literature on ITDD

Unfortunately, the spread of the drug and the efficacy of intrathecal treatment have been rather unpredictable. Medical research related to ITDD has been reviewed recently by Hocking and Wildsmith [36]. They conclude that the drug distribution depends on a large number of variables related to the characteristics of the injected solution, the clinical technique, and patient characteristics, but ultimately cannot explain the variance in patient response. In 2004 Buchser et al. [11] have published a clinical observation that suggests that using a higher flow rate can be used to obtain a clinically significant pain reduction. This observation has since then been largely confirmed in a clinical trial performed at the Morges hospital, Switzerland, in parallel to this work, and we discuss the results in chapter 2. Although clinical trials are justifiably considered as the gold standard of ITDD research, results often suffer from a limited number of patients, patient variability, and scattered response to treatment. Furthermore, ethical restrictions limit the scope of any trial.

Much research is therefore done in live animal models such as sheep [34], dogs [79], and rats [20]. These studies tend to focus on the toxicity and absorption of the drugs in the surrounding tissues, and not so much on the actual dispersion of the drug. Recent work by Allen et al. [2] suggests that the formation of granulomas, a mass of chronically inflamed tissue that is usually associated with infected tissue, is directly linked to the concentration of injected morphine. Granulomas are dangerous because they can lead to spinal cord compression and even tissue necrosis. They are also associated with a decrease in clinical effect (see for example Deer et al. [18]). These masses often appear near the catheter tip, as is shown qualitatively with two examples in figure 1.1.

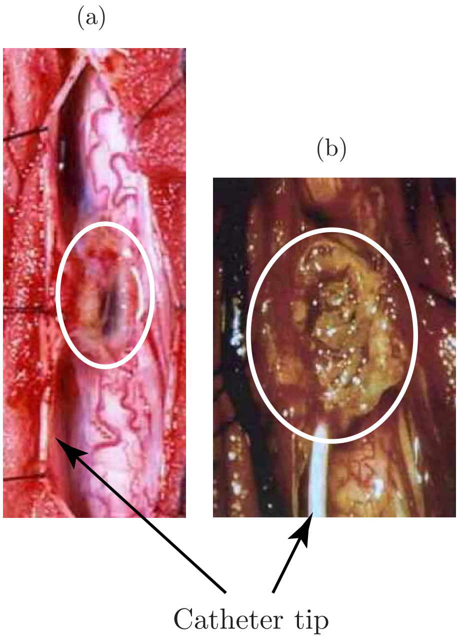
(a)

(b)

**Figure 1.1:** Two examples of human granulomas from (a) Miele et al. [46], and (b) Cabbell et al. [12] The granulomas (inside the white ellipses) are in the direct vicinity of the catheter tip, which suggests that the concentration is highest near the catheter tip.

Bernards [6] recently published an article using a live pig model that focuses specifically on the dispersion of drugs in the subarachnoid space. Based on real-time measurements using dialysis probes and post-sacrifice observations of the spinal cord (see figure 1.2), he concludes that the drug spread is limited $O(\text{cm})$ for all injection speeds, but slightly higher for higher injection speeds. This suggests that Buchser's previously mentioned observation is related to drug spread. The limited drug distribution increases the importance of the position of the catheter to reach specific nerves, however this is difficult to control. Furthermore, a limited spread leads to high local concentrations around the catheter tip which, depending on the drug, may lead to the formation of granulomas. These factors contribute to the increasing realization that limited drug spread is a fundamental problem of ITDD.

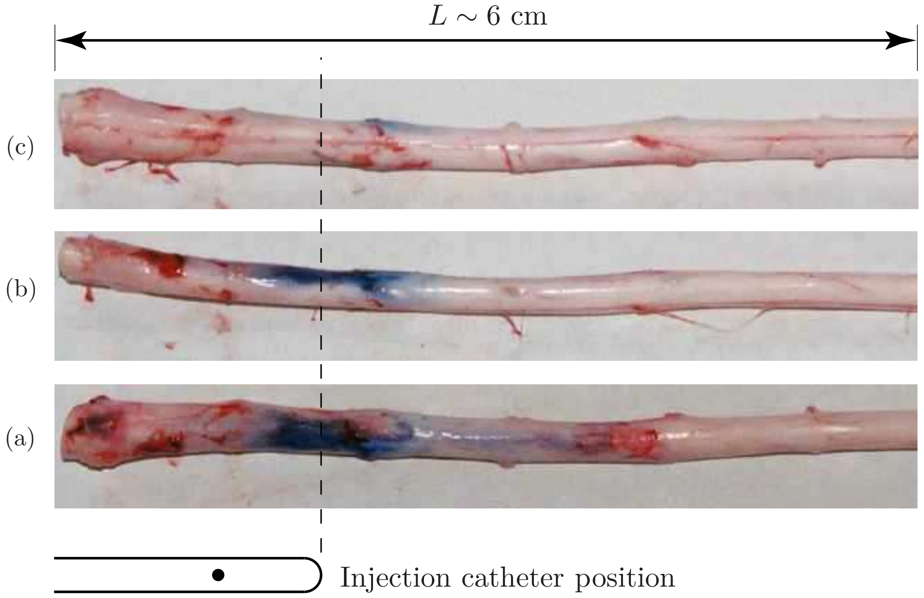

**Figure 1.2:** The (a) posterior, (b) lateral, and (c) anterior view of a spinal cord of a small pig after the injection of a contaminant dye using an (schematically shown) intrathecal catheter. The dye remains relatively concentrated near the tip, and azimuthal spread is limited. Images used with permission from Bernards [6].

Although animal models are very useful to determine the safety of the treatment they offer little explanation for the fundamental processes affecting drug spread. For this reason it is difficult to know exactly whether the drug distribution in the CSF is animal independent, or whether they are representative for the human body. Several authors have created complex in vitro models of the subarachnoid space aiming to understand drug spread and related toxicity issues [53],[55], and [57]. These models, however, systematically neglect important physiological parameters such as the oscillation of the CSF.

## 1.3 Research Questions

Clinical observations and animal models suggest that the limited spread of drugs in the CSF during ITDD can cause potentially harmful side effects such as granulomas, and can limit the clinical efficacy due to inaccurate positioning of the catheter. We therefore hypothesize that a larger spread should have a positive clinical effect. Given the fundamental lack of understanding concerning the mechanisms of drug spread, the goal of this work is therefore twofold:

1. Identify and study the fundamental mechanisms responsible for drug spread in ITDD, i.e. from the moment the drug is injected to the moment where it is absorbed in the spinal cord or surrounding tissue.

2. Investigate how these mechanisms interact and how they can be successfully used to increase the spread of the drug.

In order to experimentally study the dispersion of hydrophilic drugs in ITDD, we built a simplified model of the subarachnoid space and used a fluorescent dye to simulate the drug dispersion. We used laser induced fluorescence (LIF) measurements to quantify the mixing process. We have also performed particle image velocimetry (PIV) measurements to characterize the convective accelerations acting upon the dye. We note that a complete analysis of the efficacy of ITDD for severe pain patients would additionally require intimate knowledge of chronic pain mechanisms, pharmacology and complete pharmacokinetics[1], which goes beyond the scope of this work.

## 1.4 Scope

This thesis is composed of three parts. The remainder of the first part is composed of two chapters. Chapter 2 describes the clinical trials performed at the Morges Hospital to test the effect of a small but relatively fast bolus injection of local anesthetic. We attempt to quantify the clinical effect in terms of experienced pain, cardiovascular, and neurological changes. Intended as a confirmation of clinical observations, they are complementary to the purely fluid mechanical work that is the backbone of this thesis. In chapter 3 we discuss salient features of the subarachnoid space and provide a theoretical background of the dispersion mechanisms involved in ITDD. In addition, we describe the experimental setup that was used to study the mechanisms dispersing a drug, or local anesthetic.

The second part of the thesis specifically addresses the non-linear phenomenon of steady streaming in relation to the geometry of the subarachnoid space. This dispersion is related to convective accelerations in oscillatory flow. Chapter 6 provides a short historical overview and describes an analytical model of the steady streaming in an annular gap with a slowly varying cross section. In chapter 7 we present the results of an exploratory numerical study that addresses 3D steady streaming related to the injection catheter and the inside a realistic model of the subarachnoid space. We discuss the experimental validation of the axi-symmetric model and the catheter generated steady streaming in chapter 8.

The third and final part of this thesis concerns the quantitative study of dispersion mechanisms using LIF. We use a high frequency laser scanning setup to obtain quasi-instantaneous cross sections of dye concentration. Besides a full calibration and error analysis, we address the influence of laser scattering, absorption, and quenching on the LIF technique in chapter 11. Finally, in chapter 12 we discuss the dispersion of the fluorescent dye in our experimental model of the subarachnoid space. We specifically address the influence of the injection catheter and its orientation, the varying cross section of the annular gap, the frequency and amplitude of oscillation of the CSF, the injection speed, and buoyancy on the dispersion of the dye. Where possible we use simple parametric modeling to identify the most important factors influencing drug spread. The conclusions of this thesis are presented in chapter 13.

---

[1] Pharmacokinetic is defined as the action of drugs in the body, including the processes of absorption, metabolism, transformation, distribution to tissues, and elimination.

# Chapter 2

# Clinical trial

## 2.1 Introduction

The administration of drugs directly into the cerebrospinal fluid (CSF) has become increasingly popular in the last two decades. The intrathecal (IT) route has clear advantages that include the delivery of medication directly into the central nervous system (CNS), close to its site of action on the neuronal receptors of the central nervous tissue. This results in an increased effect even when only a fraction of the systemic dose is delivered. In addition, ITDD provides the possibility to use drugs such as local anaesthetics that cannot be administered systemically. The magnitude of the analgesic effect increases when the dose of an analgesic drug is raised. However, the appropriate dose escalation is often limited by the occurrence of side effects. Therefore, one or more drugs, usually of another class (i.e. with different mechanisms of action) must be co-administered in order to improve analgesia and minimise the dose-dependent undesirable effects. While only a very small number of drugs are approved for long-term IT administration, a survey [33] has suggested that in routine clinical practice, more than half of the patients receive a large variety of IT drugs. The most commonly used IT medication is morphine or one of its derivatives, hydromorphone. Yet, because lack of efficacy remains a problem, the adjunct of bupivacaine (a local anaesthetic (LA) drug) has been advocated to improve the analgesic efficacy in specific conditions. Although most authors reported improved pain relief as a result of the addition of bupivacaine, all but one study are uncontrolled and non-randomised case series. A multi-centre, double blind randomised study has showed that even substantial daily doses of bupivacaine administered with a continuous infusion failed to produce significant pain relief [47]. Unpublished clinical experience from a number of centres as well as one documented case study [11] suggests that the clinical effect of intrathecally administered drugs is significantly influenced by how the medication is delivered. This observation cannot be explained only by pharmacokinetic and pharmacodynamic factors alone and considerations related to the distribution of the medication in the CSF must be envisaged. The parameters as well as measurement schedule used in this study were set to detect bupivacaine-related changes, which unlike the other drugs that were co-administered, has a short onset and duration of action. Local anaesthetics (i.e. bupivacaine) produce a non-specific, concentrationŰdependent and reversible blockade of nerve conduction. The clinical effects of intrathecally administered LA's include a decrease in blood pressure, followed by sensory and motor neurological changes. Because the spinal cord has a somatotopic organisation, the site of delivery of LA is an important determinant of the clinical response. LA administered at the thoracic or lumbar levels will predominantly affect thoracic or lumbar nerve distributions, referred to as dermatomes. The area affected by the action of LA is commonly assessed by the number and the lo-

| | Dim | Mean ($\sigma$) | Min. | Max. |
|---|---|---|---|---|
| Age | Years | 61 (14) | 32 | 84 |
| Weight | kg | 62 (14) | 40 | 91 |
| Number of trails | | 1.6 (0.7) | 1 | 5 |

**Table 2.1:** Patient Statistics. Total number of patients $n = 29$, with 11 females and 18 males.

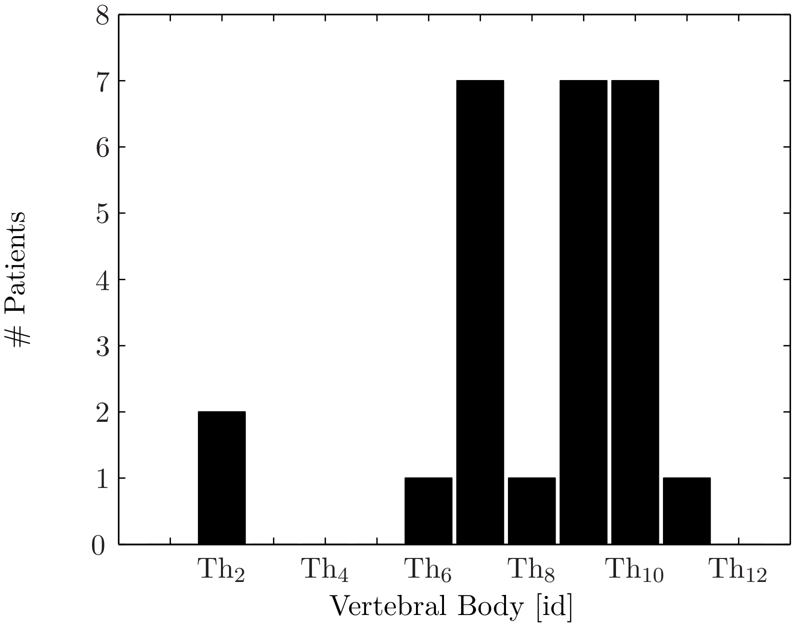

**Figure 2.1:** Histogram of the position of the catheter tip (n = 27). The position of the catheter tip was assessed on AP and lateral X-rays.

calisation of dermatomes where the cold sensation is abolished (i.e. small sensory nerve blockade).

## 2.2 Patients and methods

Following ethical committee approval and patientŠs informed consent, we studied the effect of an intrathecal injection of a small bolus bupivacaine in a mixture of two or more drugs (see table 2.2). Twenty-nine patients receiving continuous intrathecal infusions for the management of intractable pain due to cancer or non-malignant disorders were asked to participate in the study. All patients had implanted intrathecal pumps and were receiving a continuous flow of an intrathecal drug mixture containing bupivacaine. No patient had a pump implanted to be included in the protocol, nor was the medication changed in order to provide study eligibility. In most patients the tip of the catheter was placed between the 7th (Th$_7$) and the 11th (Th$_{11}$) thoracic vertebral body (see figure 2.1).

Since pain is a subjective experience, it cannot be quantified in absolute terms. We have used a non-linear analogue visual scale (VAS), which is a validated tool employed

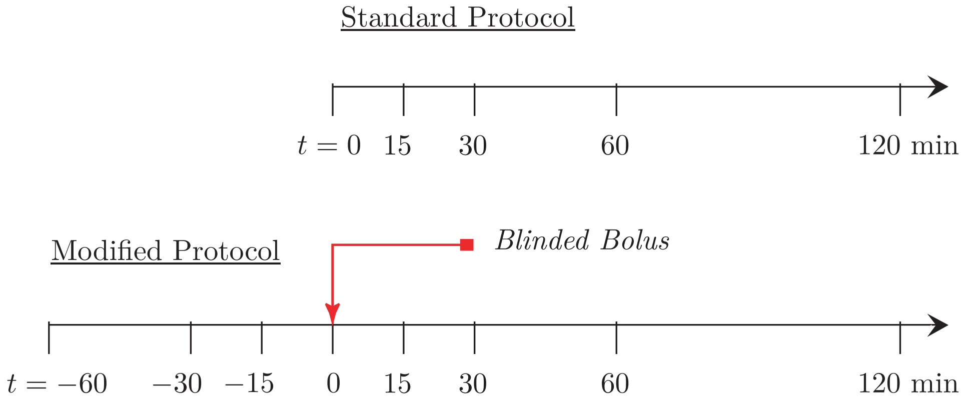

**Figure 2.2:** During the trial the patient was examined for pain (VAS), neurological changes (dermatomes), cardiovascular changes (blood pressure and heart rate), and respiratory rate at specific points in time. A modified protocol was installed during the trial to allow a better estimate of the patient's stability. The total number of trials was 50, while 8 trials were done with the modified protocol.

systematically both in clinical practice and research. The scale is a 100 mm line, 0 indicating no pain and 100 the worst imaginable pain. Neurological changes were assessed by the number and location of cold-insensitive dermatomes. After patients were installed in a comfortable supine position, an external transcutaneous telemetry programmer was used to trigger the pump to inject a predetermined bolus. Changes in pain intensity (VAS), neurological (dermatomes), cardiovascular (blood pressure and heart rate) and respiratory (rate) parameters were measured immediately before the administration of the bolus (base line) and 15, 30, 60, and 120 minutes after the bolus injection. Whenever possible, all measurements were carried out both in lying and standing positions. To provide a better estimate of the base line and minimise placebo response, the same measurements were carried out 60, 30 and 15 minutes before the bolus, which was administered in a patient blinded way. This protocol modification was introduced during the course of the study (see figure 2.2).

Information pertaining to the boli given during the trials is summarized in table 2.2. The average bolus dose of bupivacaine was 0.74 mg but was determined in each patient according to the clinical condition, hence the variability. Similarly, the volume of each bolus was in average $V_B = 44\ \mu$l, but the use of various drug mixtures and concentrations resulted in significant variations. However, for each bolus and patient, both the dose of bupivacaine and the size of the volume were very small compared to the daily dose and flow rate. Therefore, the bolus in itself was not expected to produce a clinically significant effect if only pharmacological factors were to play a role. The information gathered during each trial was used to help optimal programming of the pump parameters in each patient. As the ideal setting for any given patient may change over time and the determination of the best characteristics requires a trial and error type of approach, some patients were studied more than once and the total number of trials is 50.

| | Dim | # trials | Mean ($\sigma$) | Min. | Max. |
|---|---|---|---|---|---|
| Continuous injection rate | ml/day | 50 | 0.44 (0.22) | 0.1 | 1 |
| Bolus Volume | $\mu$l | 50 | 44 (23) | 8 | 102 |
| Bolus Injection rate | $\mu$l/s | 50 | 0.28 (0.09) | 0.03 | 0.38 |
| Dose Bupivacaine | mg | 50 | 0.74 (0.46) | 0.10 | 2.36 |
| Dose Morphine | mg | 27 | 0.38 (0.38) | 0.036 | 1.8 |
| Dose Clonidine | $\mu$g | 39 | 13 (8.7) | 1.8 | 40 |
| Dose Hydromorphone | mg | 10 | 0.32 (0.15) | 0.19 | 0.67 |

**Table 2.2:** A summary of the drug delivery used during the trials. All patients received bupivacaine, but concentration, dose, and additional drugs differed between patients.

## 2.3 Results

After the injection of a single bolus, patients experienced pain relief or neurological changes or both in 86% of the trials. The VAS scores, the appearance of dermatomes, and an overview of the cardiovascular changes are presented in the following sections.

### 2.3.1 VAS Measurements

Patients who had no pain (VAS= 0) at the beginning of a trial were not considered for this analysis, resulting in the exclusion of 7 trials. Compared to baseline, the mean VAS score decreased significantly ($p < 0.05$) both in lying and standing positions at any time after the administration of a bolus dose except for the VAS lying at 15 min. The $p$-value is defined as the probability that the values in a set are a random selection taken from the same distribution as the set with which it is compared. Figure 2.3 shows the trend of the average VAS scores in time. The data in the graph has been normalized to the VAS score at $t = 0$ minutes, so that we only look at changes with respect to the baseline. If the trial was performed with the extended baseline, the average baseline score was used to normalise the data. This explains the small variance in the initial VAS scores. The average improvement experienced was 30% or greater after $t = 30$ minutes and $t = 60$ minutes for VAS at rest and at mobilisation, respectively. Patients experienced an improvement of more than 30% for both the VAS scores compared to before the bolus injection in 77% of all trials. In comparison only a few patients (n=5 or 10% of all the trials) experienced a deterioration of more than 30% for both VAS scores during the trial. There is no evidence to suggest that this deterioration is related to the treatment. On average the VAS score at rest (mobilised) varies between 57% (61%) and 100% (85%).

### 2.3.2 Dermatome Measurements

Sensory changes were assessed by neurological testing for insensitivity to cold (ether swab). The results are expressed by the number and locations of affected dermatomes. The unit of measurement is a dermatome. The position is defined with respect to the position of the catheter tip. Because an asymmetrical dermatome distribution was often encountered, the left and right side dermatomes are considered separately. Loss of cold sensation (der-

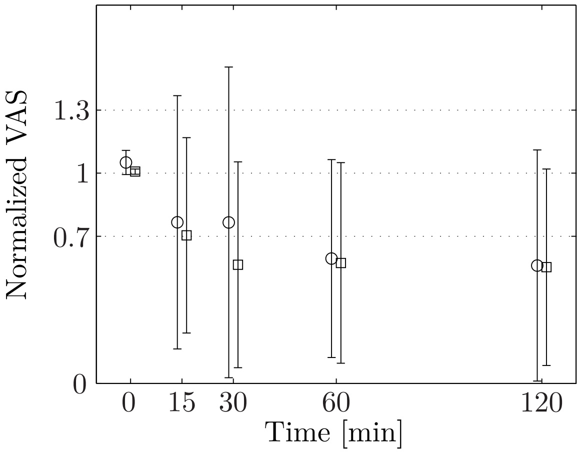

**Figure 2.3:** The time evolution of the normalized mean VAS score. The ○ are the VAS score at rest, while the □ are the VAS at mobilization. The average of the VAS score between $t = -60$ to $t = 0$ was used for normalization if available, otherwise the VAS score at $t = 0$ was used. Trials with an initial VAS score of zero (n = 7) were excluded. The symmetric bars around the mean include 75% of the population.

matome) was observed in 75% of the trials. In 57% of the trials new dermatomes appeared after the bolus injection. These generally appeared 15 to 30 minutes after the injection.

In each trial the highest (most cranial) and lowest (most caudal) dermatome was identified with respect to the catheter tip. Figure 2.4 shows a histogram of all the combined measurements. It is not uncommon to measure the lowest dermatome at a level above the catheter tip, or the highest dermatome below the catheter tip.

We define the centre of the dermatomes as the average between the highest and the lowest cold insensitive dermatome. On average dermatomes are centred somewhat below the catheter tip. This is illustrated in figure 2.5.

The extent of the clinical effect is calculated as the difference between the highest and the lowest dermatome. As shown in figure 2.6, the affected area varies between 1 and 10 dermatomes. Some extreme cases were measured with spreads up to 26, but these cases are based on only a few identified dermatomes and could be measurement errors.

### 2.3.3 Cardiovascular and Respiratory Changes

Whenever possible, the systemic blood pressure (BP) was measured with the patient in supine, and standing positions. The BP tends to decrease at all times after the bolus injection, although the change is quantitatively modest. Maximum and minimum systolic, diastolic and mean blood pressure following the bolus injection are normalised to the initial value. Table 2.3 shows the average values calculated over all the case studies. Changes in heart rate and respiration were also monitored. Although there is a trend towards lower heart rates after the bolus injection, the differences are neither clinically nor statistically significant and are therefore not included. The respiration rate remained unchanged.

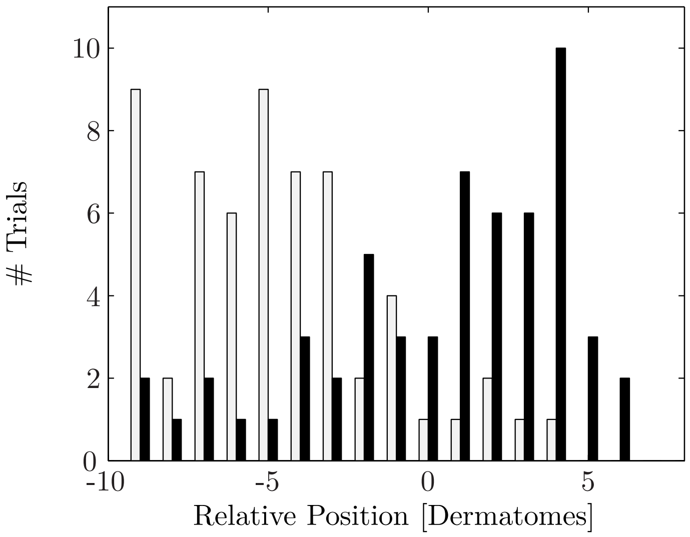

**Figure 2.4:** Histogram of the lowest (grey) and highest (black) dermatome measured at any time during the trial with respect to the catheter tip. Because the measured dermatomes are not necessarily symmetric between the left and right side of the patient each side is treated separately.

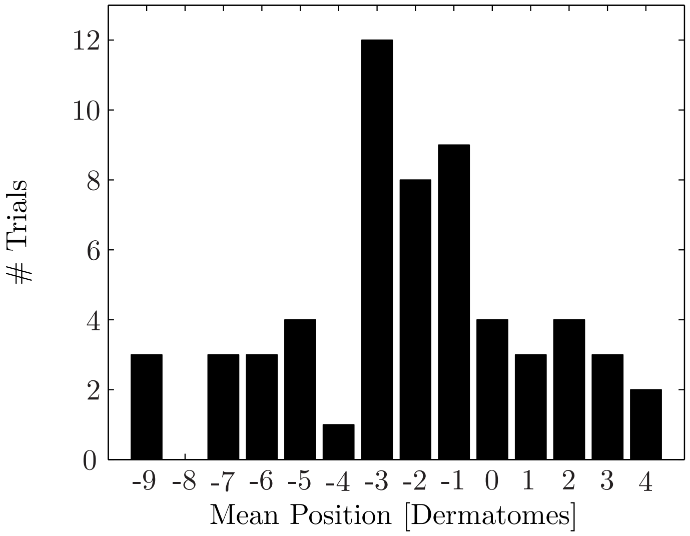

**Figure 2.5:** A histogram of the average position of the highest and lowest dermatome measured at any point during the trial. On average the dermatomes seem to be centred on a point below the catheter tip. Catheters have multiple holes and it is assumed that the drug is flowing through the most proximal orifice which is located about half a dermatome below the catheter tip.

## 2.4 Discussion

All patients in this study are suffering from chronic pain that proved refractory to conventional management and required the implantation of a programmable pump and the

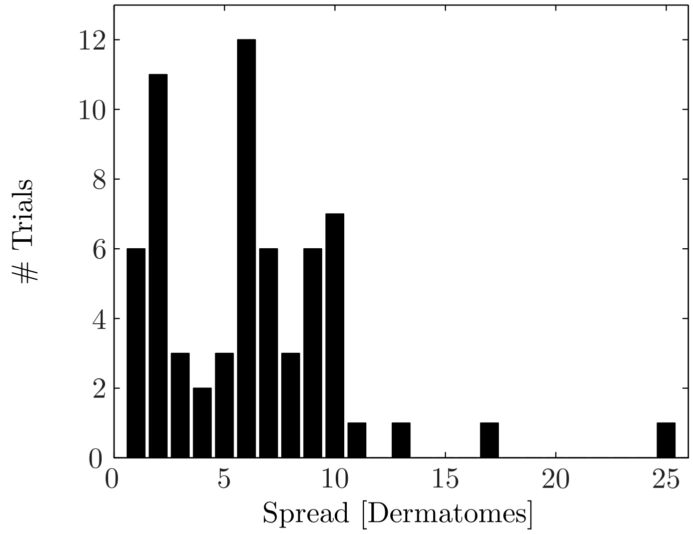

**Figure 2.6:** Histogram of the difference between the highest and lowest measured dermatome.

| | Systolic | | Diastolic | | Mean | |
|---|---|---|---|---|---|---|
| | Min. | Max. | Min. | Max. | Min. | Max. |
| Lying | 86% | 97% | 85% | 97% | 87% | 104% |
| Upright | 82% | 97% | 84% | 103% | 87% | 104% |

**Table 2.3:** The average minimum and maximum blood pressure at any point after the bolus injection ($t \geq 15$ min). The average is calculated over all the case studies.

administration of drug combinations containing a local anaesthetic drug (bupivacaine). Though all the drugs contained in the mixture produce analgesia, bupivacaine is by fare the most fast-acting and the only that causes measurable neurological changes. For practical purposes however, we have assumed that all modifications that were observed were due to the effect of bupivacaine. A further assumption is that all compounds of the mixture will behave in a similar way in terms of dispersion in the CSF.

Although controlled to a large extend, the majority of patients in this study suffer mild to moderate pain at most times. The administration of a small dose produced additional pain relief in the majority of patients. The decrease in VAS score is clinically significant since the pain improvement is in excess of 30% [17] and occurs consistently at rest as well as during mobilisation (standing).

Patients included in this study had pain from a variety of disorders, both cancer and non-cancer related. Therefore, the pain mechanisms were not similar and most patients experienced fluctuations in the intensity of their symptom that was related to a number of factors. This explains why in a small numbers of cases there was no pain at baseline, and the trials (n=7) could not be used for VAS changes. In other instances, peaks of incidental pain caused the VAS to increase slightly after the administration of a bolus dose.

Differences in the mechanism of pain, fluctuations of pain states and the small number of patients contribute to confound the results. Nevertheless, the data confirm the initial observation [2] suggesting that in average, small (clinically non-significant) doses produce clinically significant pain improvement.

At lower doses, the IT administration of a local anaesthetic produces a dose-dependant arterial hypotension that is due to the blockade of the sympathetic nerve fibres. In this series of patients, BP remained unchanged, confirming that bolus doses were of negligible clinical significance. However 6 patients could not assume the standing position because of dizziness presumably due the cardio-vascular auto regulation impairment.

Sensory changes were observed in 75% of the trials, which is consistent with the effect on pain, though both effects are not necessarily occurring in the same subjects. The somatotopic organisation of the spinal cord implies that the number and the location of cold-insensitive dermatomes that appear after a bolus injection indicates the physical spread of the drug in the subarachnoid space. However, since there is overlap in the somatosensory organization of the spinal cord, the clinical delimitation of sensory changes can be blurred. The error associated with the measurements of dermatomes is therefore estimated to be ±1. In addition, a similar error is expected with the assessment of the position of the catheter tip, as catheters are floating in the intrathecal space resulting in unpredictable position changes. We therefore expect the combined error on the assessment of dermatomes with respect to the catheter tip to be of the order of ±2 dermatomes.

Figure 2.5 does show a distinct peak of dermatome activity between -3 and -1 dermatome levels below the catheter tip. Given that the catheter injection ports are placed 12 mm below the tip, which is about half a dermatome, and the assumed measurement error of ±2, the peak in the histogram could correspond to the injection site. This would suggest that bupivacaine tends to travel in a caudal direction before it binds to the receptors in the spinal cord and nerve roots.

Factors that determine the anatomical location and the number of affected dermatomes include the position of the tip of the catheter and the drug dispersion. We therefore assume that dermatomes are at least weakly correlated with the physical dispersion of the drug. Given an approximate average vertebral body height of 3 cm [73], we can estimate the spread to be roughly 0-30 cm from figure 2.6. This estimate is crude and the range is larger than the values measured by Bernards in his pig model [6]. The weak correlation of the dermatomes with the injection site is expected to increase the estimated value of the spread on top of the usual error of ±2 dermatomes.

## 2.5 Conclusion

During the trial the patient was examined for pain (VAS), neurological changes (dermatomes), cardiovascular changes (blood pressure and heart rate), and respiratory rate at specific points in time. A modified protocol was installed mid-trial to allow a better estimate of the patient's base line status. The total number of trials was 50, while 8 trials were done with the modified protocol. The variation of the extended baseline measurements is small compared to the effects we discussed, but the limited number of trials with the modified protocol prevents a quantitative analysis of variance.

The effect of bupivacaine, whether in terms of pain relief, neurological or cardiovascular changes, could not be directly correlated to the injection parameters (i.e. injection speed, bolus volume). Yet, the administration of a fast but small bolus dose on top of a slow but significant background infusion resulted in clinically detectable effects in the majority of trials. Differences in bupivacaine concentrations, patient size, small number of cases and variable catheter tip positions are potential confounding factors, and the importance of flow patterns characteristics remains unclear.

Nevertheless, the data suggests that the infusion of a fast bolus is associated with a quick distribution of the drug to a relatively large area. We will address the fluid mechanics that might be responsible for these phenomena in detail in the remainder of this work.

# Chapter 3

# Dispersion Mechanisms in ITDD

This chapter gives an overview of the dispersion mechanisms relevant to ITDD. To this effect we first describe the oscillatory flow of the CSF inside the spinal canal in section 3.1 and the typical geometry of the subarachnoid space in section 3.2. We suggest that the oscillation is the primary driver for the dispersion of the local anesthetic. We evaluate this hypothesis in the remainder of this chapter by discussing the order of magnitude of all the possible dispersion mechanisms that act upon the drug, specifically molecular and enhanced diffusion, steady streaming induced by the complex geometry of the system[1], the velocity of the injection jet, and buoyancy. We also discuss the influence of ignoring the absorption of the drug into the spinal cord when assessing the drug spread in the CSF.

## 3.1 Cerebrospinal Fluid (CSF) Oscillation

The cerebrospinal fluid (CSF) contained in the subarachnoid space is Newtonian and its viscosity ranges between $0.7 \cdot 10^{-6}$ and $1 \cdot 10^{-6}$ m$^2$/s [8]. It is therefore similar to water at 37°C. CSF is created at a rate of roughly 500 ml/day. Until the 1990's it was commonly accepted that the CSF flowed down the spinal canal towards the lower end of the spine and up again to be reabsorbed. Although many textbooks on physiology still cling to this model, measurements using phase contrast MRI techniques have demonstrated that it is wrong. In fact the CSF is subject to a complex oscillatory motion driven primarily by changes in the intracranial blood volume during the cardiac cycle (see for example Bhadelia et al. [7] and Loth et al. [42]). The oscillatory waveform has no measurable mean flow. In addition to the heart rate, the waveform is also modulated by other physiological factors such as for example the respiratory rate. Because the spinal cord itself is only slightly compressible, and the arachnoid is essentially bounded by the rigid the vertebral bodies, we assume that the characteristic velocity is dependent on the section of the subarachnoid space and is determined by mass flow conservation. Although the arachnoid is a closed sack, the lumbar sack is free to expand to accommodate the cyclic increase and decrease of mass flow. As will be explained in the remainder of this chapter, this oscillating motion combined with the presence of the catheter or other geometric perturbations in the subarachnoid cavity will give rise to enhanced diffusion and convection that will influence the dispersion of the local anesthetic. Before we address these dispersion mechanisms in more detail, we therefore characterize the human subarachnoid space in the next section.

---

[1] Although we discuss diffusion mechanisms in detail in this chapter, an in depth analysis of steady streaming is presented in part I.

## 3.2 Geometry of the Subarachnoid Space

The subarachnoid space (SAS), the volume surrounding the spinal cord into which the intrathecal catheter is placed, is essentially an annular volume bounded by the arachnoid. The arachnoid is a thin transparent sheet that holds the CSF. Although large variations between individuals are possible, the typical anatomy of the spine is well documented (see for example [28]). The vertebral foramina constitute a canal for the protection of the spinal cord. This canal is large and triangular in the cervical and lumbar regions, where it is relatively small and rounded in the thoracic region. The thoracic channel is nearly cylindrical over its entire length. A qualitative overview of the upper lumbar and lower thoracic spinal canal is shown in figure 3.1 using a sagittal[2], and a coronal[3] plane.

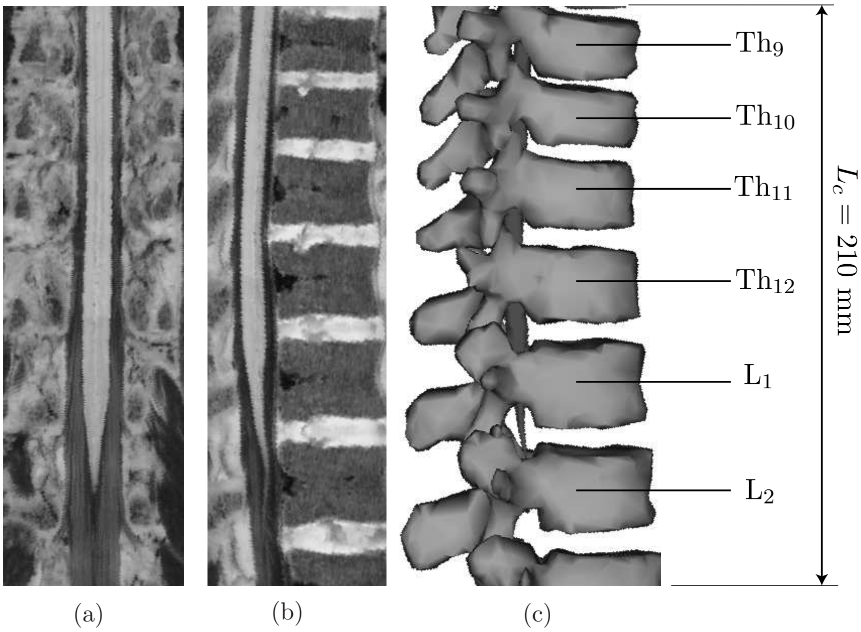

**Figure 3.1:** The (a) coronal and (b) sagittal cross sections of the subarachnoid space of the upper lumbar and lower thoracic spine. (c) Shows the corresponding 3D representation in which the spinal cord is made darker for clarity. The images were extracted from the visible human database [65]. The spinal cord is not always centered in the channel, and the outer wall of the canal has small shape variations. The limited resolution of the images permits only the observation of traces of nerves, specifically in the lumbar region.

The spinal cord forms the elongated part of the central nervous system which occupies the upper two-thirds of the vertebral canal. Both the cervical and lumbar regions of the spinal cord show enlargements corresponding to the attachment of large nerves which supply respectively the upper and lower limbs. The spinal cord itself is slightly flattened in the cervical region, but nearly circular in the thoracic and lumbar regions. The diameter

---

[2] A sagittal plane divides the body in left and right

[3] A coronal plane divides the body in back and front

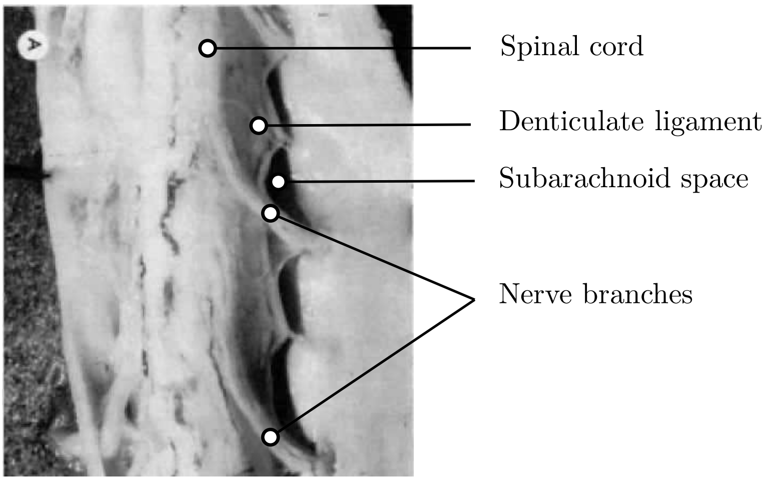

**Figure 3.2:** A dissection of the human thoracic subarachnoid space showing the nerve branches and denticulate ligament. The influence these complex features have on drug dispersion are not considered in this work, but could be included in future models.

of the spinal cord varies considerably between individuals [39].

As a first approximation we model the thoracic subarachnoid space as the empty annular gap between two non-flexible concentric cylinders. Our model can incorporate a slowly varying cross section and is described in more detail in chapter 4. Our model underestimates the true complexity of the subarachnoid space, for example: the spinal nerves and vessels that branch out at regular intervals (see figure 3.2), the varying non-concentric position of the spinal cord within the spinal canal, the flexing of the spinal column and cord with movement [48], patient movement, and finally the natural curvature of the spine. The influence of a small number of these perturbations is addressed with a numerical model in chapter 7.

## 3.3 Molecular Diffusion

Molecular diffusion is the net motion of molecules from regions of high concentration to regions of low concentration. Diffusion is driven by Brownian motion. Combining the law of mass conservation with Fick's first law, stating that the flux of the molecules $q$ is proportional to the concentration gradient $\partial C/\partial \mathbf{x}$, where $C$ is the concentration, we can derive the diffusion equation:

$$\frac{\partial C}{\partial t} = D\nabla^2 C \tag{3.1}$$

We assume that the molecular diffusivity $D$ is not a function of the local concentration. $D$ for bupivacaine in water at 25 °C was measured to be $D = 6.7 \cdot 10^{-10} \pm 10\%\ \mathrm{m}^2/\mathrm{s}$ [10] meaning that even for high drug concentration gradients diffusion will be slow. If we assume an initial homogeneous azimuthal and radial distribution, we can reduce equation 3.1 to one dimension. We define our axis in the $\mathbf{e}_z$direction and use an initial step distribution defined by:

$$C(z,t=0) = 0, \quad \forall |z| > z_c \tag{3.2}$$

$$C(z,t=0) = 1, \quad \forall |z| \leq z_c \tag{3.3}$$

where $C$ has been normalized for convenience. We can calculate an analytical solution using a Laplace transform, the result is:

$$C(z,t) = \frac{1}{2}\left(\operatorname{erf}\left(\frac{z_c - z}{2\sqrt{Dt}}\right) + \operatorname{erf}\left(\frac{z_c + z}{2\sqrt{Dt}}\right)\right) \tag{3.4}$$

where erf is the Gaussian error function that is defined as $2/\sqrt{\pi}$ times the integration of a Gaussian distribution with zero mean and a variance of $1/2$. This result may be interpreted as a probability density function. The error function can be expanded in a Taylor series:

$$\operatorname{erf}(x) = \frac{2}{\sqrt{\pi}} \sum_{n=0}^{\infty} \frac{(-1)^n x^{2n+1}}{n!(2n+1)} \tag{3.5}$$

For sufficiently large time scales, we may therefore write:

$$\lim_{t\to\infty} \operatorname{erf}\left(\frac{z + z_c}{2\sqrt{Dt}}\right) = \frac{2(z+z_c)}{2\sqrt{D\pi}} \frac{1}{\sqrt{t}} + O(t^{-3/2}) \tag{3.6}$$

Under the assumption of 1D diffusion, the concentration will therefore diminish with $t^{-1/2}$ at any given $z$.

A numerical evaluation of equation 3.4 shows that to achieve a 1% concentration of the scalar[4] at $z - z_c = 1$ cm for an initial step at $z_c = 0$ mm one has to wait 1 day. We therefore state that the typical diffusion time $\tau_D = O(\text{days})$. We can also define a typical distance the dye travels through diffusion per oscillation cycle $\delta_D = \sqrt{D/\omega}$. Based on the parameters of our system $\delta_D$ is $O(\mu\text{m})$, which is negligible on a clinical scale.

## 3.4 Enhanced Diffusion

Inside a fluid flowing in a tube, the radial shear will increase the rate of axial diffusion compared to molecular diffusion alone (see for example Taylor [68] and Aris [3]). We attempt to qualitatively explain this phenomenon by tracking two diffusive particles in an oscillatory boundary layer characterized by a peak to peak displacement amplitude $d_{\text{osc}}$ as shown schematically in figure 3.3. During the first half of the oscillation cycle, from $t(0) \rightarrow t(\pi)$, both particles move with the flow field and we additionally hypothesize that they cross the streamlines through molecular diffusion. For illustration purposes we assume that this happens in two sequential steps. During the second half of the oscillation $t(\pi) \rightarrow t(2\pi)$ the particles move along their respective streamlines in the opposite direction. Assuming that they then diffuse back to their original streamline produces the net result that the particles have separated longitudinally, even though the time average velocity of the flow field is equal to zero and there was no longitudinal diffusion. This movement, known as enhanced diffusion, allows the particle to travel further than by molecular diffusion alone.

---

[4] We use the word scalar to signify a non-reacting dye that is only described by its concentration.

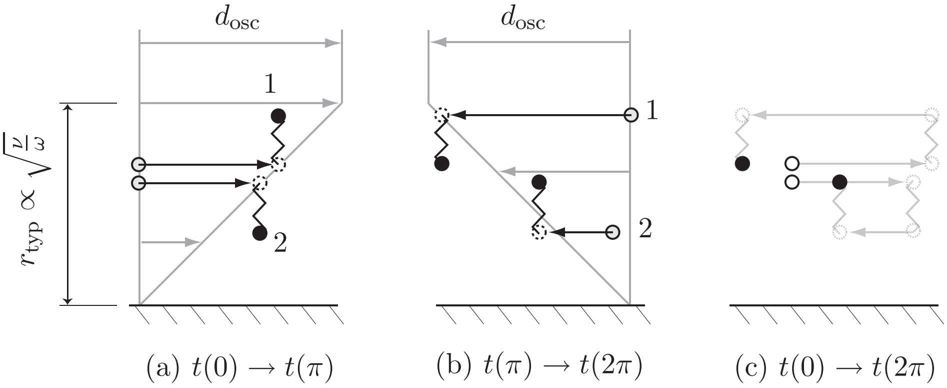
$d_{\text{osc}}$
$d_{\text{osc}}$
$r_{\text{typ}} \propto \sqrt{\frac{\nu}{\omega}}$
1
2
1
2
(a) $t(0) \rightarrow t(\pi)$
(b) $t(\pi) \rightarrow t(2\pi)$
(c) $t(0) \rightarrow t(2\pi)$

**Figure 3.3:** Illustration of enhanced diffusion by tracking two transversely diffusing particles (zigzag line) in an oscillatory shear flow (arrows) at (a) half the oscillation cycle ($t = \pi$), (b) at the end of the oscillation cycle ($t = 2\pi$). (c) shows the displacement after one full cycle. Grey ○ indicate the initial position, white ○ the intermediate positions, and ● the final position. $d_{\text{osc}}$ is a typical longitudinal (e.g. $\mathbf{e}_z$) displacement, and $r_{\text{typ}}$ is a typical transverse distance (e.g. $\mathbf{e}_r$). In this illustration the particle did not diffuse longitudinally.

Furthermore, the extent should increase with the amount of shear in the fluid, described by $d_{\text{osc}}/r_{\text{typ}}$, the ratio of the characteristic longitudinal displacement $d_{\text{osc}}$ and characteristic transverse displacement $r_{\text{typ}}$.

The dispersion of a scalar in a moving fluid is mathematically described by the convection-diffusion equation:

$$\frac{\partial C}{\partial t} + (\mathbf{v} \cdot \nabla)\, C = D \nabla^2 C \tag{3.7}$$

where $\mathbf{v}$ is the fluid velocity. Contrary to equation 3.1 this expression includes scalar transport by advection. We consider the case of axial oscillatory flow $w(t)$ in a cylinder ($\mathbf{e}_z$). We use axi-symmetric cylindrical coordinates $(r, z)$. Although two approximate solutions exist for this case, we first attempt a statistical approach to the phenomena. Following the argumentation of Chatwin [13] we formulate several hypotheses that will allow us to reduce equation 3.7 to 1D whilst retaining a qualitative understanding:

1. The time required for radial diffusion is relatively short compared to axial transport.
2. Because of Brownian motion, both the position $\mathbf{r}_p$ and the velocity $\mathbf{v}_p(t)$ of a particle are random functions of time with finite variance.
3. Dye moves with the spatial mean of the axial flow $\bar{w}(t)$ inside the pipe. This has been shown experimentally by Griffiths in 1911 [29] in steady flow, and was later substantiated mathematically by Taylor in 1953 [68]. It has since then been shown to be valid experimentally for unsteady flow.

The first hypothesis allows us to write that the radial concentration is rather homogenous, or equivalently $\bar{C}(z, t) \approx C(r, z, t)$. Using the central limit theorem[5] and the second hypothesis, we may deduce that the dye distribution will become normally distributed.

---

[5] The central limit theorem states that if the sum of independent, identically distributed random variables has a finite variance, then it will be approximately normally distributed.

$\bar{C}(z,\tau)$, where $\tau$ is a moment in time, can therefore be interpreted as the probability distribution function of the longitudinal displacement of the dye, similar to the 1D diffusion in the previous section. We may therefore write:

$$\bar{C}(z,t) = \frac{1}{\sqrt{2\pi\sigma^2}} \mathrm{e}^{-\frac{(z-z_\mathrm{g})^2}{2\sigma^2}} \tag{3.8}$$

where the standard deviation $\sigma = \sigma(t)$ is defined by:

$$\sigma^2(t) = \int_{-\infty}^{\infty} (z - z_\mathrm{g})^2 \bar{C}(z,t)\mathrm{d}z \tag{3.9}$$

and $z_\mathrm{g}$ is the center of mass of the scalar distribution:

$$z_\mathrm{g}(t) = \int_{-\infty}^{\infty} z\bar{C}(z,t)\mathrm{d}z \tag{3.10}$$

The center of mass is also related to the spatial average of the positions of all the particles $z_\mathrm{g}(t) = \langle \mathbf{r}_p \rangle$, or alternatively:

$$\dot{z}_\mathrm{g} = \langle \mathbf{v}_p(t) \rangle = \bar{w}(t) \tag{3.11}$$

where we have used the third and final hypothesis. By direct differentiation of equation 3.8 we find

$$\frac{\partial \bar{C}}{\partial t} = \frac{1}{2}\frac{\mathrm{d}\sigma^2}{\mathrm{d}t} \cdot \frac{\partial^2 \bar{C}}{\partial z^2} \tag{3.12}$$

Finally, using equations 3.11 and 3.12, and by introducing an enhanced diffusion diffusion coefficient $D_\mathrm{enh} = D_\mathrm{enh}(t)$, we can rewrite the advection-diffusion equation for $\bar{C}(z,t)$:

$$\frac{\partial \bar{C}}{\partial t} + \bar{w}(t)\frac{\partial \bar{C}}{\partial z} = D_\mathrm{enh}\frac{\partial^2 \bar{C}}{\partial z^2} \tag{3.13}$$

As $\bar{w}$ gives no indication of the shear inside the flow field, $D_\mathrm{enh}$ must express the influence of shear on enhanced diffusion, and is therefore a function of the velocity profile. However, if we use equation 3.12 we can see that $D_\mathrm{enh}$ can also be derived from the variance of the spatial distribution of $\bar{C}$:

$$D_\mathrm{enh} = \frac{1}{2}\frac{\mathrm{d}\sigma^2}{\mathrm{d}t} \tag{3.14}$$

Because $\sigma^2$ is a quadratic function of $(z - z_\mathrm{g})$ we expect to find that the $D_\mathrm{enh}$ depends on the amplitude squared of the imposed oscillatory flow. Given the dependence of $z_\mathrm{g}$ on the average axial velocity $w$ we can assume that $D_\mathrm{enh}(t)$ will contain harmonic terms of $\omega$ and $2\omega$.

There are two approaches described in literature to find an approximate analytic expression for $D_\mathrm{enh}$, taking into account the specific unsteady velocity profile and the full convection diffusion equation 3.7. Both are consistent at large time scales, and will be evaluated separately. Harris and Goren [32] and Watson [77] have shown that by assuming a linear and homogeneous concentration gradient along the axis the temporally averaged mean flux $\bar{q}$ across a stationary cross-section is given by:

$$\bar{q} = -D_\mathrm{enh}\frac{\mathrm{d}\bar{C}}{\mathrm{d}z} \tag{3.15}$$

an expression similar to Fick's first law. Using this simplification Watson [77] showed that the functional dependence of the enhanced diffusivity can be expressed by:

$$D_{\text{enh}} = D\left(1 + f_{\text{T}}\left(\alpha, \text{Sc}\right)\left(\frac{2V_T^2}{r_{\text{H}}^6}\right)\right) \tag{3.16}$$

where $V_T = d_{\text{osc}}(\pi r_o^2)$ is the stroke volume, $d_{\text{osc}}$ is the stroke distance, and $r_o = r_{\text{H}}/2$, where $r_o$ is the radius of the tube and $r_{\text{H}}$ its hydraulic radius. $\alpha = r_{\text{H}}\sqrt{\omega/\nu}$ is the relative thickness of the unsteady boundary layer which depends on the angular frequency $\omega$ and the viscosity $\nu$ of the oscillating fluid. The Schmidt number is defined as $\text{Sc} = \nu/D$, and relates the importance of viscous to molecular diffusion. $f_{\text{T}}(\alpha, \text{Sc})$ is a function that depends on the unsteady velocity profile. Tsangaris [71] calculated $f_{\text{T}}$ for oscillatory flow in an annular gap. Given our model parameters, equation 3.16 is only valid for $t \sim O(r_o^2/D) = O(\text{hour})$, the time required to achieve a nearly homogeneous radial scalar distribution, which as is long compared to the experiments ($\sim$ 30 min) that we typically consider in this thesis.

Gill and Sankarasubrama ([25], [26] and expanded upon by Smith [64]), describe the dispersion using a derivative series expansion for $\bar{C}(z,t)$ which consists of concentration gradients and functions describing the unsteady velocity profile. Using this method Elad et al. [21] have calculated the dispersion in a cylindrical tube and compared the outcome in terms of a time averaged effective diffusivity:

$$\frac{\overline{D_{\text{enh}}}(t)}{D} = 1 + \text{Pe}^2 G(\alpha, \text{Sc}) \tag{3.17}$$

where the superscript ($\bar{\ }$) denotes the mean over one oscillation cycle. The Péclet number, indicating the influence of advection to diffusion, is given by $\text{Pe} = \alpha^2 A_{\text{osc}}\text{Sc}$, where $A_{\text{osc}} = d_{\text{osc}}/r_{\text{H}}$ is the non-dimensional stroke distance. Besides being a measure of amplitude, it is also a measure of shear. The function $G(\alpha, \text{Sc})$ expresses the shear in the unsteady velocity profile, and is given by:

$$G = \frac{\alpha^2}{2}\left|\frac{\text{J}_1(\alpha\sqrt{-\text{i}})}{\text{J}_2(\alpha\sqrt{-\text{i}})}\right|^2 \sum_{n=1}^{\infty} \frac{\gamma_n^2}{(\gamma_n^4 + \alpha^4)(\gamma_n^4 + \alpha^4\text{Sc}^2)} \tag{3.18}$$

where $\text{J}_\varsigma$ is a Bessel function of the first kind of order $\varsigma$, and $\gamma_n$ is the $\text{n}^{\text{th}}$ zero of the $\text{J}_1(\alpha\sqrt{-\text{i}})$. It can be shown explicitely that equation 3.17 is valid for time scales $t \sim 0.2r_o^2/D = O(\text{min})$.

The relative increase $D_{\text{enh}}$ compared to $D$ according to equations 3.17 and 3.18 is shown in figure 3.4 for relevant parameters. For values estimated to be relevant for ITDD, specifically $4 < \alpha < 10$, $A_{\text{osc}} < 8$, and $\text{Sc} \approx 2000$, the enhanced diffusion is estimated to be up to 150 times as important as molecular diffusion. The typical distance the dye travels per oscillation cycle due to enhanced diffusion $\delta_{ED}$ can therefore become of $O(\text{mm})$, which, contrary to molecular diffusion, is relevant on a clinical scale. To understand the functional dependence of 3.17 and 3.18 we use:

$$\lim_{\alpha\to\infty} G(\alpha, \text{Sc}) = \frac{1 - \text{Sc}^{-1/2}}{\alpha^3(\text{Sc}^2 - 1)} \tag{3.19}$$

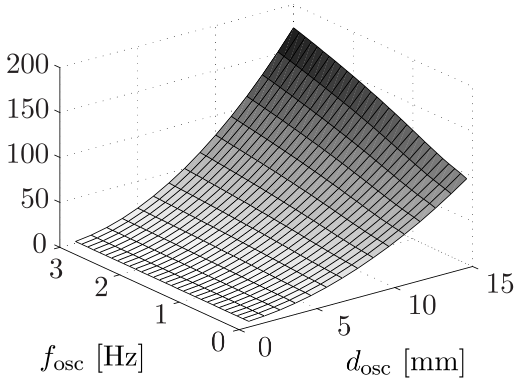

**Figure 3.4:** $\overline{D_{\mathrm{enh}}}(t)/D$ as a function of characteristic parameters $d_{\mathrm{osc}}$ and $f_{\mathrm{osc}}$. Additional parameters were $\nu = 0.7 \cdot 10^{-6}$ m$^2$/s, and $r_{\mathrm{H}} = 3 \cdot 10^{-3}$ m

For large Sc representative of liquid-liquid diffusion, we therefore find:

$$D_{\mathrm{enh}}/D \propto \alpha A_{\mathrm{osc}}^2 \tag{3.20}$$

Several authors have successfully used equation 3.17 with 3.18 to experimentally measure the enhanced diffusivity (see for example Gaver et al. [24]).

## 3.5 Steady Streaming

Steady streaming is a non-zero mean flow induced by non-linear effects in incompressible oscillatory flow. It occurs, but not exclusively, whenever a viscous oscillatory flow is set up over any axial inhomogeneity. In this work we only consider changes in cross section representative of the spinal canal or the injection catheter. The steady streaming typically manifests itself as recirculation cells with a characteristic velocity that is an order of magnitude smaller than those associated with the oscillatory flow itself. Womersley [78] was one of the first authors to successfully describe non-linear steady streaming phenomena in pulsating flows, specifically for flexible arteries. His name is therefore commonly given to the parameter $\alpha = r_{\mathrm{H}}\sqrt{\omega/\nu}$ that expresses the relative thickness of the viscous boundary layer in oscillatory flow. The specific characteristics of steady streaming in ITDD are discussed in detail in part I using analytical, numerical and experimental techniques. Anticipating the results we state that the typical steady streaming velocity for ITDD is proportional to the steady streaming Reynolds number $\mathrm{Re}_{\mathrm{s}} = \alpha^2 A_{\mathrm{osc}}^2$. The typical steady streaming velocity for ITDD is estimated to be $O(1$ mm/s).

The ratio of viscous to molecular diffusion can be expressed using the Schmidt number $\mathrm{Sc} = \nu/D$. For high Sc, such as found in fluid-fluid diffusion, steady streaming will increase the dispersion of a scalar, both though advection and diffusion forces. As shown by Grotberg [30] the Lagrangian motion of the scalar at low and moderate Womersley numbers qualitatively follows the streamlines of the mean velocity field (see section 12.6 for an experimental confirmation). Once the dye is entrained into the recirculation cells its surface area will increase promoting a more rapid diffusion, similar to enhanced diffusion. The influence of steady streaming is naturally restricted to the size of the recirculation cell which depends on the exact characteristics of the perturbation. Depending on the geometry, steady streaming is the phenomena that can transport the drug over the largest distance, say a vertebral body height, in the shortest time.

Several authors have defined a diffusivity that includes the dispersion due to steady streaming (see for example the analysis of the dispersion coefficient in a curved tube by Sharp et al. [63], or Hydon and Pedley [37] for dispersion in a channel with oscillating walls). Some caution is required however, because the continuity equation requires that the net mass flow across a cross section must be zero. Ultimately the steady streaming influence on the mixing of the scalar is therefore due to the increase of the surface area, and not to the mass flow of the steady streaming itself. As remarked by Grotberg [30] it is therefore counterintuitive to combine the notion of an enhanced diffusivity to enhanced diffusion due to steady streaming. It may however be appropriate if the observed axial dispersion is Gaussian. This can happen for example when the recirculation cells are widespread and small compared to the total dispersion.

## 3.6 Injection Jet

The injection rate ($Q_{\mathrm{inj}}$) typically used in ITDD ranges from roughly 1 $\mu$l/min (~1 ml/day) to 30 $\mu$l/min. When using the Medtronic catheter Indura® model 8711, the local anesthetic is injected through two most proximal injection ports of diameter $\phi_{\mathrm{c}} = 0.7$ mm (see the preliminary report by Truong [70]). We therefore simplistically approximate the injection speed with $V_{\mathrm{inj}} \sim Q_{\mathrm{inj}}/(\phi_{\mathrm{c}}^2) < 1$ mm/s. The typical distance the local anesthetic travels due to $Q_{\mathrm{inj}}$ per oscillation period is $\delta_{\mathrm{inj}} \sim Q_{\mathrm{inj}}/\phi_{\mathrm{c}}^2\omega$. We note that the Reynolds number for the injection jet of a fast bolus ($Q_{\mathrm{inj}} = 30$ $\mu$l/min) is low, $\mathrm{Re}_{\mathrm{inj}} = Q_{\mathrm{inj}}/(\phi_{\mathrm{c}}\nu) \approx 1$. The injection jet will therefore quickly be attenuated by viscous dissipation, an effect that will be even more important for low injection rates. Consequently, the dye is not expected to spread very far due to the influence of $Q_{\mathrm{inj}}$ alone.

The bigger the difference between $\delta_{\mathrm{inj}}$ and $\delta_{\mathrm{ED}}$, the more dye will be folded into surrounding medium before it diffuses. We express the advection with respect to the diffusion with a Péclet number for the injection rate $\mathrm{Pe}_{\mathrm{inj}} = Q_{\mathrm{inj}}/(\phi_{\mathrm{c}}D)$. However, we know from the previous section that the axial diffusion is augmented by shear. For a more realistic expression for $\mathrm{Pe}_{\mathrm{inj}}$, assuming a high Sc, we can replace $D$ with $D_{\mathrm{enh}}$ using equation 3.20. We find $\mathrm{Pe}_{\mathrm{inj}} = Q_{\mathrm{inj}}/(\phi_{\mathrm{c}}\alpha A_{\mathrm{osc}}^2 D)$. For sufficiently high injection rates, or simply a high $\mathrm{Pe}_{\mathrm{inj}}$, the dispersion becomes dominated by advection. A natural consequence is that concentration gradients will remain relatively high whilst spreading the local anesthetic over a relatively large distance from the injection site.

## 3.7 Drug Buoyancy

Normal solutions of bupivacaine at body temperature such as used in ITDD are known to be less dense[6] than the CSF [45]. Buoyancy is not easily quantifiable analytically and requires numerical simulations or experiments for a detailed understanding. Two non-dimensional numbers are often used to estimate the extent of the buoyancy effect. The

---

[6] The term hypobaric is often clinically used to denote a solution that is lighter than the CSF, while hyperbaric is used for a fluid that is heavier than CSF. To avoid any possible confusion with relative pressure, this terminology is not used in this thesis.

Rayleigh number, $\mathrm{Ra} = g\beta^*\Delta C r_{\mathrm{H}}^3/\nu D$, where $g$ is the gravitational acceleration, and $\beta^* = 1/\rho \cdot \partial\rho/\partial C$ is the relative variation of density ($\rho$) with concentration ($C$), describes the ratio of buoyancy to diffusive forces. The Péclet number $\mathrm{Pe} \equiv \mathrm{ReSc} = \alpha^2 A_{\mathrm{osc}}\mathrm{Sc}$ indicates the rate of advection compared to the rate of viscous and molecular diffusion.

Some theoretical work has been done by, amongst others, Erdogan and Chatwin [22] and Barton [5]. They suggest that the additional dispersion due to buoyancy in a steady flow in a tube is proportional to Ra squared. The dispersion is predicted to be relatively higher for lower Pe. Importantly, these authors conclude that the dispersion induced by buoyancy at large time scales is small compared to dispersion by buoyancy at short, transient time scales. This is because the density difference between the two fluids will diminish as they diffuse, expressed in $\beta^*$. In this respect, it is logical to assume that a higher $\mathrm{Pe}_{\mathrm{inj}}$, due to for example a higher $Q_{\mathrm{inj}}$, will permit the dye to travel further before it diffuses.

We define the Grashof number $\mathrm{Gr} \equiv \mathrm{Ra}/\mathrm{Sc}$ to express the ratio of buoyancy to (only) viscous forces:

$$\mathrm{Gr} \equiv g\beta^*\Delta C r_{\mathrm{H}}^3/\nu^2 \tag{3.21}$$

Based on the measured densities of plain bupivacaine at 37°C, and a bolus volume of 50 $\mu$l the Grashof number would be in the order of 1000. Combined with the knowledge that the effect is related to Ra squared, this suggests a substantial effect of buoyancy, but this is diminished by shear augmented diffusion and viscous dissipation of the injection jet. LIF experiments that shall be discussed at length in part II of this thesis, showed that a dye similar to bupivacaine was relatively quickly dispersed. This indicates a short transient time scale indicating that the density difference $\Delta\rho$ would be considerably diminished during the injection time. Furthermore, during the slow infusion of plain local anesthetics in a pig model by Bernards [6] there was no evidence of buoyancy. No attempt was therefore made to measure, or study the buoyancy effect of plain bupivacaine.

Although the effect of buoyancy is probably minor or nonexistent for normal local anesthetics, the addition of glucose can be successfully used to influence the spread in for example epidural anesthesia (see for example Vercauteren et al. [74], and Bannister et al. [4]). Qualitative experiments have therefore been performed with low concentration glucose solutions, see section 12.10, showing that buoyancy does indeed become the determining factor of the dispersion.

## 3.8 Absorption into the Spinal Cord

The spinal cord is a porous, structured medium, characterized by 20 nm diameter pores [76]. In ITDD the drugs are not directly injected into the spinal cord tissue itself[7], thus we assume that there are no pressure gradients inside the extracellular space driving the drug over significant distances. In fact, several authors have observed that drug transport inside the spinal cord is dominated by molecular diffusion [50]. We therefore hypothesize that the uptake of the drug is proportional to the surface area of the spinal cord that is in contact with the drug, as well as the concentration gradient across this area. Additionally, one must consider the interaction of the drug with the spinal cord tissue, i.e. the pharmacokinetics.

---

[7] Direct interstitial injection of drugs is commonly known as convection-enhanced delivery (CED). See for example Sarntinoranont et al. [59] for a relatively recent numerical model of CED drug spread.

Especially the degree of lipophilicity of the drug is an important determinant for local drug concentration in the spinal cord and the surrounding tissue [72].

As previously argued, molecular diffusion is a very slow process in comparison with the other dispersion mechanisms. In the spinal cord this is illustrated by the time scale on which the clinical effect takes place, typically 15 to 60 minutes after the injection of a small bolus containing bupivacaine, a quick acting local anesthetic. Furthermore, dynamic concentration measurements in a live pig model [6] with intrathecal bupivacaine have shown that a steady state concentration near the catheter tip is reached only two hours after a continuous slow injection is started. This is an equilibrium state between the continuous injection, the absorption into the spinal cord, and the dispersion in the CSF. This relatively long time scale also suggests a relatively slow uptake into the spinal cord.

Absorption of the drug into the spinal cord or surrounding tissue decreases the time the drug stays in the CSF and therefore limits the axial spread that could be obtained through enhanced diffusion and steady streaming. Although agarose gels can be used to model the diffusion into the spinal cord [14], this was not deemed necessary taken into account the relative speed ($O$(min), see previous sections) of the other drug dispersion mechanisms. Because we do not attempt to model the absorption of the drug in the surrounding tissue, our models will overestimate the axial dispersion at long time scales.

## 3.9 Summary

Based on the analysis above the dispersion is to depend on the following parameters:

- $\mathrm{Pe_{inj}} = \frac{Q_{\mathrm{inj}}}{\phi_{\mathrm{c}} D_{\mathrm{enh}}}$ describing how concentrated the dye remains before diffusion substantially lowers the concentration gradients. Low $Q_{\mathrm{inj}}$ favors diffusion, while high $Q_{\mathrm{inj}}$ favors advection.

- $\mathrm{Pe} = \alpha^2 A_{\mathrm{osc}} \mathrm{Sc}$ describing how important advection is with respect to molecular diffusion.

- $\mathrm{Pe}^* = (\alpha / A_{\mathrm{osc}})\mathrm{Sc}$, equivalent to Pe where $D$ has been substituted with relation 3.20, describing the influence of advection with respect to enhanced diffusion. A large $A_{\mathrm{osc}}$ will increase the apparent diffusion, while $\alpha$ increases the relative importance of advection.

- $\mathrm{Re_s} = \alpha^2 A_{\mathrm{osc}}^2$ describing the influence of the steady streaming. Furthermore, steady streaming will increase the surface area of the drug after injection and thus enhance the mixing.

- Ra, Pe, and $\mathrm{Pe_{inj}}$ are required to study the influence of buoyancy. The quicker a scalar is diluted, the quicker the influence of the buoyancy is reduced.

# Chapter 4

# Setup

With knowledge of the oscillation, geometry, and the likely order of magnitude of the dispersion mechanisms presented in the previous chapeter, we have designed the experimental and optical setup.

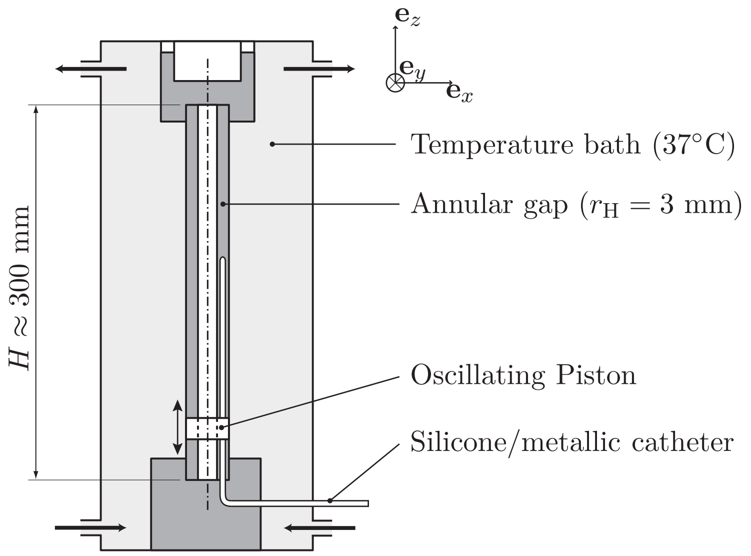

**Figure 4.1:** Schematic of the temperature controlled experimental setup. A cog-less linear motor directly drives the piston. The catheter is guided into the test section using a hypodermic needle. The upper part of the catheter (∼ 50 mm) is free to move. There is optical access from above and from all 4 sides. To minimize temperature gradients the experiments is wrapped in polystyrene.

## 4.1 Model and Material

A schematic of the experiment is show in figure 4.1. The annulus is made of two concentric, straight, 300 mm tall glass tubes (Schott A.G., Duran glass) containing distilled water. Our parameterization is derived from measurements taken from the Visible Human project [60]. The annular gap has an external radius $r_o = 7.5$ mm, an internal radius $r_i = 4.5$ mm and the hydraulic radius is therefore $r_\mathrm{H} = r_o - r_i = 3$ mm. The basic geometry is shown in figures 4.2. We place the origin of the coordinate system on the axis of the cylindrical tubes at the height of the catheter tip. The straight annular gap can be replaced by a section made out of Plexiglas that has a slightly varying cross section as shown in figure

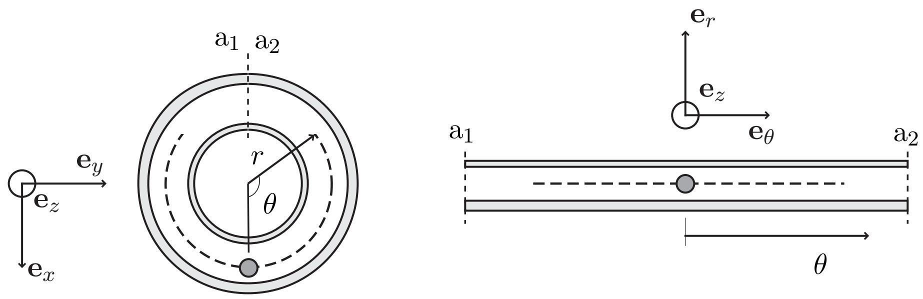

(a) Top view experiment (b) 'Unfolded' top view

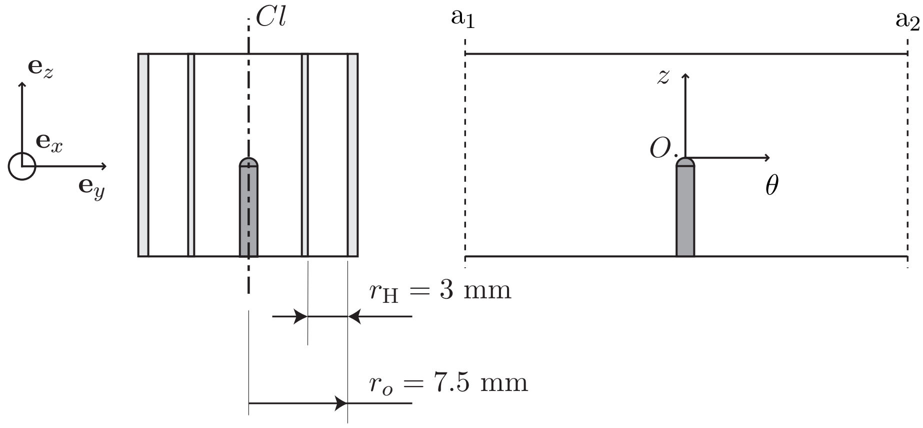

(c) Front view (d) $(\theta, z)$–projection

**Figure 4.2:** The coordinate system used throughout this work. Figures (a) and (b) show the top projection of the annular gap in Cartesian and cylindrical coordinates, respectively. Figure (c) shows the camera field of view, while (d) shows a commonly used $(\theta, z)$–projection of the annular gap, where the origin is placed at the catheter tip. shows the cross section of the symmetry plane $y = 0$. The dotted line in the middle of the annular gap shows the plane used in chapter 7 for post processing of numerical results, corresponding to $(r = 6 \text{ mm}, \theta, z)$.

4.3. Its radius is defined by

$$r = r_o \pm \frac{\Delta r_o}{2} \left(1 - \cos\left(2\pi \hat{z}/L\right)\right), \qquad \hat{z} \in [0, L] \tag{4.1}$$

where $L \in \{25, 50, 75\}$ mm is the height, and $\Delta r_o \in \{0.7, 1.4, 2.1\}$ mm is the peak to peak amplitude of the perturbation. $r_o = 7.5$ mm is the radius of the unperturbed outer wall. We define the typical slope of the perturbation as $\epsilon = 2\Delta r_o/L$. A schematic of an example of a constricted cross section annular gap is shown in figure 4.3.

This geometry models variations in the subarachnoid canal as found in for example the lumbar or cervical regions of the spine, or locally as induced by nerve branches. As will be explored in part I, this relatively slow variation of the outer wall will induce steady streaming that can be analytically modeled with an asymptotic analysis (see specifically chapter 6). In the remainder of this thesis we will refer to geometries with $\min(r) < r_o$ as constricted, and geometries with $\max(r) > r_o$ as expanded.

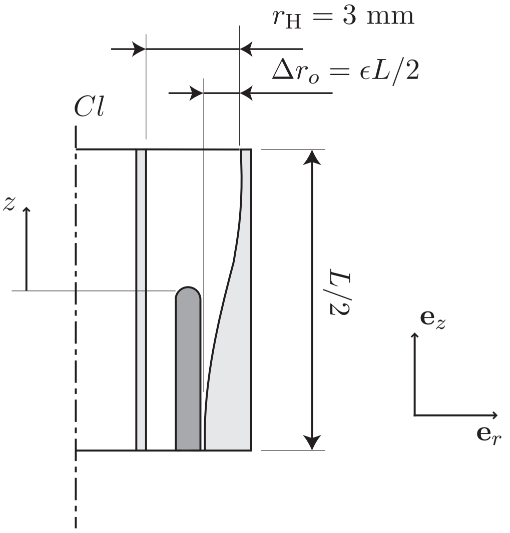

**Figure 4.3:** A schematic of a constricted cross section annular gap.

Because the CSF has roughly the same characteristics as water at the same temperature, we maintain the entire test section at 37°C using a re-circulating temperature controlled bath (Lauda Gmbh). This also ensures that the experiment is not subject to variations in room temperature. The oscillatory flow field is established using a small piston placed inside the annular gap that is driven by a cog less linear motor (Tecnotion B.V.). The oscillatory waveform can be freely programmed to correspond to a singly harmonic, or complex waveforms such as measured by Loth [42]. The peak-to-peak displacement amplitude typically used is 5 – 13 mm, and the frequency ranges from 0.8 – 2.5 Hz. Several waveforms used throughout this thesis are shown in figure 4.4.

An intrathecal silicon catheter (Medtronic, model 8711) is introduced parallel to the axis into the test section from below though the piston using a hypodermic needle. The top 5 cm of the catheter is unsupported and the piston movement induces a small uncontrolled oscillatory motion of the catheter tip $< 0.25r_{\mathrm{H}}$. The catheter is placed as straight as possible in the middle of the annular gap, but in absence of supporting structures the position is not entirely reproducible. A metallic straight catheter with the same 1.4 mm outer diameter and rounded tip as the Medtronic catheter was made and used to reduce the effect of curvature on the steady streaming. The catheter orientation $\varphi$ is defined as the angle between the axes of the two most proximal ports through which the dye is injected [70] in relation to the $\theta$-direction of the annular gap. This is shown in figure 4.5. $\varphi = 0$ corresponds to injecting in the tangential direction, while $\varphi = \pi/2$ corresponds to injecting into the boundary layers of the oscillatory flow.

## 4.2 Optical Scanning System

Our aim is to measure quasi-instantaneous 3D concentration profiles using laser induced fluorescence. Rockwell [56] reviewed several scanning techniques that were considered. We opted for a system of rotating mirrors (GSI Lumonics) and long focal length cylindrical

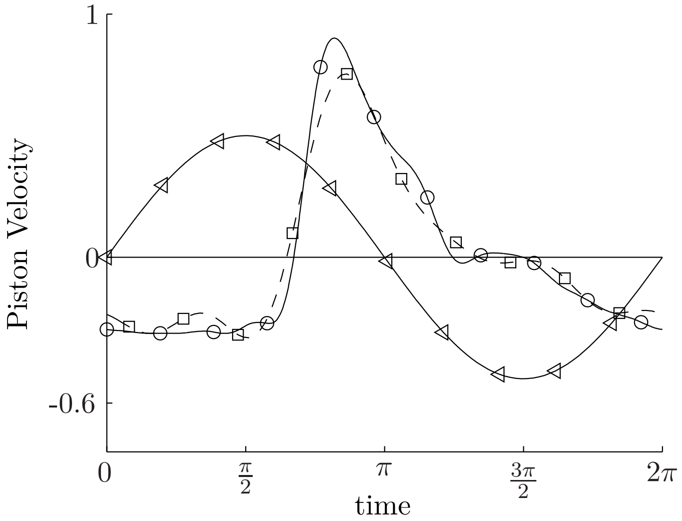

**Figure 4.4:** Several waveforms were used to specify the piston speed. (◁) is a sinusoidal, while the red (○) is the mass flow curve measured in vivo by [42]. This non-singly harmonic signal is characterized by a fundamental frequency of 0.77 Hz and a stroke distance of $d_{\text{osc}} = 12.89$ mm, (□) is a Fourier series fit on the latter with a decreased spectral content. This curve has specifically been used for the PIV experiments.

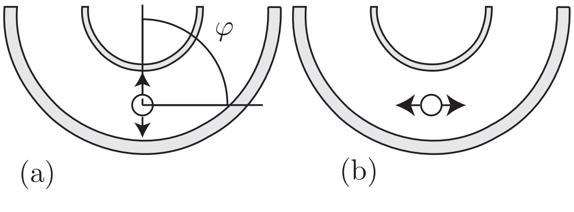

**Figure 4.5:** The injection direction $\varphi$ in two experimental configurations, namely (a) $\varphi = \pi/2$, and (b) $\varphi = 0$.

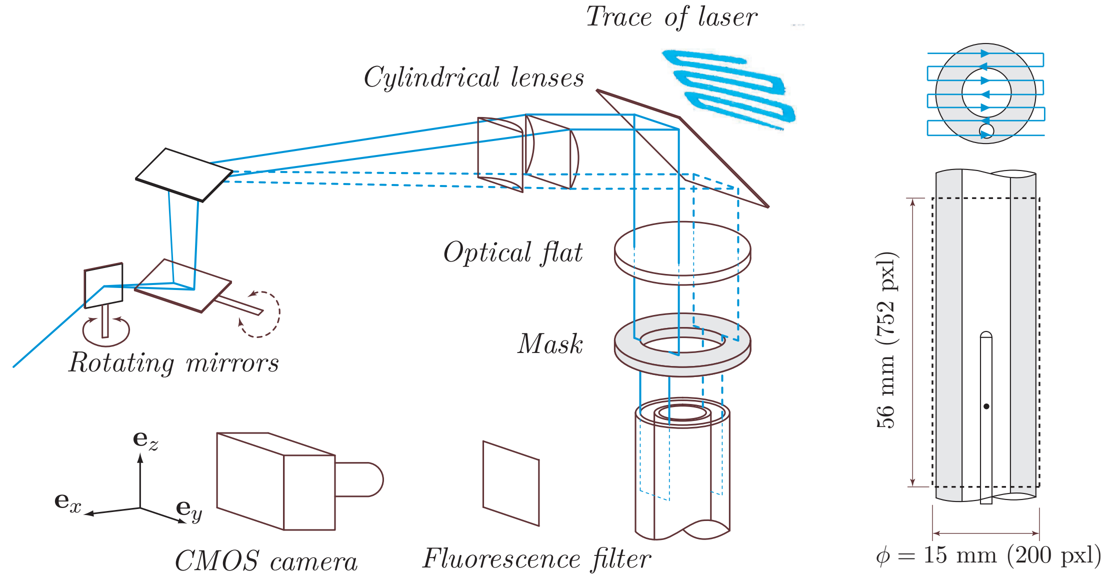

(a) (b)

**Figure 4.6:** (a) A light sheet of width $\Delta y \approx 20$ mm is made and incrementally scanned across the annular gap ($\Delta x \geq 0.4$ mm) from above using high speed rotating mirrors. A high speed CMOS camera is triggered by the mirrors. The optical flat is used to avoid a free surface of the water, and the mask cuts away all the light that would not fall inside the annular gap. The cutoff filter only lets through the fluorescent signal. (b) The typical field of view of the camera.

lenses ($f$=1500 mm) because of its inherent scanning flexibility, light sheet homogeneity and scanning speed. The optical bench is shown schematically in figure 4.6. A laser sheet is created by quickly rotating an 8 mm mirror. We project this sheet in small increments over the entire cross section of the annular gap using a 15 mm mirror. The maximum scan frequency, approximately 800 Hz, is determined by the speed of rotation of the mirrors and the distance of the mirrors to the test section. Deusch and Dracos [19] and Tian and Roberts [69] have used a similar configuration in their LIF experiments. A 350 Hz (full frame), $752 \times 582$ pixels, 8-bit CMOS camera (Photonfocus, model MV-D752) is triggered by the rotating mirrors. Because of its flexibility we were able to perform both PIV (see section 8) and LIF experiments (see part II) with it. Our typical window size is $752 \times 200$ and the lowest resolution we worked with was approximately 75 $\mu$m/pixel, which could be increased using a 12× optical zoom lens (f/# 2.4, Computar). The typical field of view of the camera is shown in figure 4.6(b). Our scanning speed is limited by the time required to upload a captured image to the working memory of the dedicated acquisition computer. We sweep the focused laser beam across the annular gap in 0.94 ms during which time the image is taken. While we wait 1.54 ms for the transfer of the image, we place the laser at the starting point of the next plane. Defined as the time of the sweep with respect to the total scan time, our duty cycle is 38%. We can maintain a total scan frequency of 390 Hz for long periods, limited only by computer memory. Single plane PIV measurements were done at 250 Hz.

A continuous 5 W Ar-ion laser (Spectra Physics) was used. We expand the laser beam diameter 5× and focus it on the test section, roughly 2.5 m further away. Based on these parameters, the theoretical beam width is 180 $\mu$m. For the LIF experiments only the 488 nm 1.5 W blue line was used and we placed a cutoff filter in front of the camera to eliminate laser reflections from the fluorescent signal. A full analysis of how this scanning technique can be optimized for quantitative LIF taking into consideration quenching, scattering, optical aberrations of the system, and laser beam attenuation is presented in chapter 11.

To model the local anesthetic, i.e. bupivacaine, we used fluorescein. This fluorescent tracer has a high quantum yield making it ideal for the high speed acquisition. Because of its slightly lower molecular weight fluorescein is expected to have a slightly lower diffusivity $D_{\text{fluo}}(T = 37°\text{C}) = 7.9{\cdot}10^{-10}$ m$^2$/s compared to bupivacaine at the same temperature. The diffusivity of bupivacaine was measured at 25°C, namely $D(T = 25°\text{C}) = 6.7 \cdot 10^{-10} \pm 10\%$ m$^2$/s [10][1]. We can use the Stokes-Einstein relation $D \sim T/\mu$, where $\mu$ is the dynamic viscosity of the solvent, to estimate $D(T = 37°\text{C}) = 10 \cdot 10^{-10} \pm 10\%$ m$^2$/s. Taking into account the error on the measured diffusion constant, $D$ is 13 to 37% larger than the diffusivity of fluorescein. This implies that the LIF experiments will be more diffusive than is realistic for ITDD.

---

[1] In comparison with other drugs cited in the same article, we note that this value is probably too large.

# Part I

# Steady Streaming in ITDD

# Chapter 5

# Introduction

Oscillatory flow inside complicated geometries is known to generate steady recirculation zones known as steady streaming. This non-zero mean velocity will be important in spreading the anesthetic inside the subarachnoid space. In order to investigate and characterize the nature of the steady streaming inside the subarachnoid space, we present an axi-symmetric analytical model in chapter 6. In chapter 7 we present the results of a numerical study to specifically characterize the steady streaming induced by the presence of the injection catheter and in a realistic model of the subarachnoid space. Finally, in chapter 8 we describe an experimental PIV study performed to validate the analytical and numerical results, characterize the steady streaming present inside the experiment, and qualitatively explore the effect of a slowly varying cross section annular gap on the steady streaming near the catheter tip.

# Chapter 6

# Steady Streaming Theory

## 6.1 Introduction

Steady streaming is defined as the non-zero mean of the fluctuation flow of an incompressible fluid. The term acoustic streaming is normally reserved for the same phenomenon in compressible fluids. In 1802 Chladni [15] was the first known observer of acoustic streaming. Later, in 1831 Faraday [23] experimentally studied this phenomenon and Lord Rayleigh [52] provided the first analytical framework for this phenomenon in 1884. Riley [54] reviewed more recent work in 2001, and summarized that steady streaming can result directly from the action of a non-conservative body force, or indirectly through the influence of Reynolds stresses inside a viscous fluid, or alternatively in free surface flows.

Ground breaking theoretical and practical work on internal oscillatory flow in human arteries was published by Womersley in the 1950's (amongst others [78]). The non-dimensionless number that expresses the relative thickness of the unsteady boundary layer in oscillatory flow is now commonly named after him. We define:

$$\alpha = r_{\mathrm{H}}\sqrt{\frac{\omega}{\nu}} \tag{6.1}$$

where $\omega = 2\pi f_{\mathrm{osc}}$ is the natural frequency of the oscillation and $r_{\mathrm{H}}$ a characteristic length such as the hydraulic radius. A paper published by Stuart in 1966 [66] provides the mathematical framework by which oscillatory flows with high $\alpha$ are often analyzed. Based on the Reynolds stresses associated with general unsteady boundary layers, he concludes that the typical steady streaming velocity far away from the Stokes boundary layer scales as $V_s \sim O(U_\infty^2/\omega r_{\mathrm{H}})$, where $U_\infty$ is the free stream velocity.

For oscillatory flow in a tube we may write $U_\infty \sim \omega d_{\mathrm{osc}}$, where $d_{\mathrm{osc}}$ is defined as the stroke distance, for example the peak to peak displacement of the piston. We define the tidal volume $V_T = S d_{\mathrm{osc}}$, where $S$ is the characteristic surface area of the tube. Based on the characteristic steady streaming speed we can identify a steady streaming Reynolds number $\mathrm{Re_s}$ for free, or internal flows:

$$\mathrm{Re_s} = \frac{V_s r_{\mathrm{H}}}{\nu} = \frac{U_\infty^2}{\omega\nu} = \alpha^2 A_{\mathrm{osc}}^2 \tag{6.2}$$

where $A_{\mathrm{osc}} = d_{\mathrm{osc}}/r_{\mathrm{H}}$ is the non-dimensional oscillation amplitude. We have used $V_s \sim O(\omega d_{\mathrm{osc}}^2/r_{\mathrm{H}})$. We note that using this notation the normal Reynolds number is defined as $\mathrm{Re} = \alpha^2 A_{\mathrm{osc}}$.

In the 1970's several authors, including Ramachandra and Deshikachar [51], Manton [44], and Hall [31] used different asymptotic approaches to describe streaming in tubes with slowly varying cross-sections, i.e. tubes for which the change in radius $\Delta r_o$ is small

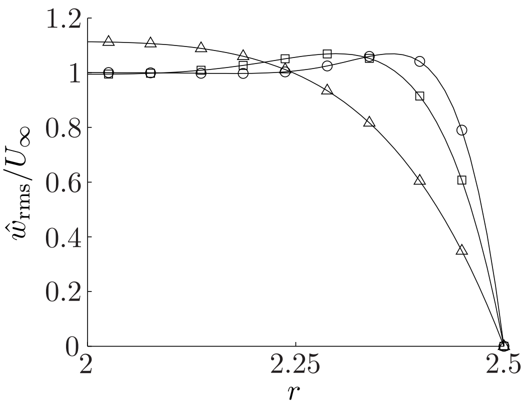

**Figure 6.1:** The root mean square profile of the unsteady boundary layer in a constant cross section annular gap for $\alpha = 4$ (△), 8 (□), or 12 (○). The Stokes layer has a phase shift of $\pi/2$ and the higher RMS velocity adjacent the inviscid core for high $\alpha$ is known as the annular effect.

compared to the characteristic length of the change $L_c$, $\epsilon = \Delta r_o/L_c \ll 1$, and a low Reynolds number, $\mathrm{Re} = \alpha^2 A_{\mathrm{osc}} \ll 1$. Grotberg [30] described the steady streaming in a tapered channel with the possibility of changing the parameters of the flow, such as the Womersley number, without conserving the pressure gradient. When for example the frequency is increased the unsteady speeds do not decrease monotonically as a result, as is the case for the aforementioned work of Hall. Grotberg finds that for low Womersley numbers the steady streaming is characterized by a steady bi-directional drift. The flow near the centerline is in the direction of the wider end of the channel, and towards the narrow end near the boundaries. For moderate $\alpha \approx 10$ the flow near the centerline reverses. For high $\alpha$ a secondary steady drift layer is formed next to the inner boundary layer. This phenomenon is related to the phase difference between the Stokes boundary layer and the inviscid core (which oscillates with the imposed pressure gradient). The root mean square velocity is actually higher adjacent to the inviscid core than inside it. This phenomenon is known as the annular effect [62] and is shown in figure 6.1. It will become evident in the next section why this can reverse the flow near the midline. Grotberg also investigated the results for high $\alpha$, corresponding to $\mathrm{Re} \gg 1$, by using a matched asymptotic analysis similar to Stuart's. For this he defines a drift-layer thickness that is thicker than the Stokes-layer thickness. As expected, given the importance of the Reynolds stresses in steady streaming, the mean velocity in the inviscid core tends to zero for increasing $\alpha$.

## 6.2 Annular Gap with Slowly Varying Cross Section

Following Grotberg, we non-dimensionalize the cylindrical Navier–Stokes equations with the aim of finding a series solution in terms of the non-dimensional slope of the perturbation $\epsilon = \Delta r_o/L_c = 2\Delta r_o/L$, where $L$ is a characteristic length of our specific perturbation described in section 4. We use the hydraulic radius $r_{\mathrm{H}} = \hat{r_o} - \hat{r_i}$ as the typical dimension of the annular gap, where a superscript $(\hat{\ })$ is used to denote dimensional quantities. For an axi-symmetric flow field $(\hat{u}, 0, \hat{w})$ and coordinates $(r, \theta, z)$, we write:

$$
\begin{aligned}
r = \frac{\hat{r}}{r_{\mathrm{H}}}, \qquad z &= \frac{\hat{z}\epsilon}{r_{\mathrm{H}}}, \qquad t = \hat{t}\omega, \qquad Q = \frac{2\pi\hat{Q}}{V_T\omega} \\
u = \frac{\hat{u}}{\omega d_{\mathrm{osc}}\epsilon}, \qquad w &= \frac{\hat{w}}{\omega d_{\mathrm{osc}}}, \qquad p = \frac{\epsilon\hat{p}}{\rho(\omega d_{\mathrm{osc}})^2} \qquad (6.3)
\end{aligned}
$$

The non-dimensionalization of the pressure with $\epsilon$ anticipates that even the leading order pressure gradient varies linearly with the slope of the perturbation. The Navier–Stokes equations reduce to:

$$
\begin{aligned}
\frac{1}{r}\frac{\partial}{\partial r}(ru) + \frac{\partial w}{\partial z} &= 0 && (6.4)\\
\epsilon^2\alpha^2\frac{\partial u}{\partial t} + \epsilon^3\mathrm{Re}\left(u\frac{\partial u}{\partial r} + w\frac{\partial u}{\partial z}\right) &= -\mathrm{Re}\frac{\partial p}{\partial r} + \cdots \\
&\quad + \epsilon^2\left(\frac{1}{r}\frac{\partial}{\partial r}\left(r\frac{\partial u}{\partial r}\right) - \frac{u}{r^2} + \epsilon^4\frac{\partial u}{\partial z^2}\right) && (6.5)\\
\alpha^2\frac{\partial w}{\partial t} + \epsilon\mathrm{Re}\left(u\frac{\partial w}{\partial r} + w\frac{\partial w}{\partial z}\right) &= -\mathrm{Re}\frac{\partial p}{\partial z} + \frac{1}{r}\frac{\partial}{\partial r}\left(r\frac{\partial w}{\partial r}\right) + \epsilon^2\frac{\partial^2 w}{\partial z^2} && (6.6)
\end{aligned}
$$

where we define $\mathrm{Re} = \alpha^2 A_{\mathrm{osc}}$ as the standard Reynolds number of the flow. No-slip boundary conditions apply: $u(r_i, z) = u(r_o(z), z) = 0$ and $w(r_i, z) = w(r_o(z), z) = 0$. We then seek a series solution by expanding $u, w, p$, and $Q$ in powers of $\epsilon$ and therefore require $\epsilon \ll 1$, and $\epsilon\mathrm{Re} \ll 1$. Each power series is written in the form:

$$
u = u_0 + u_1\epsilon + O(\epsilon^2) \qquad (6.7)
$$

This approach is identical to the work of Sarkar and Jayaraman [58], except for a slightly different non-dimensionalization. In this work the important steps in the analysis by Sarkar and Jayaraman are repeated for clarity, but the reader is referred to their work for more detail.

After substitution of 6.7 in 6.5 and 6.6 we find at leading order:

$$
\begin{aligned}
\frac{1}{r}\frac{\partial}{\partial r}(ru_0) + \frac{\partial w_0}{\partial z} &= 0 && (6.8)\\
0 &= \frac{\partial p_0}{\partial r} && (6.9)\\
\alpha^2\frac{\partial w_0}{\partial t} &= -\mathrm{Re}\frac{\partial p_0}{\partial z} + \frac{1}{r}\frac{\partial}{\partial r}\left(r\frac{\partial w_0}{\partial r}\right) && (6.10)
\end{aligned}
$$

with boundary conditions $u_0(r_i, z) = u_0(r_o(z), z) = 0$, and $w_0(r_i, z) = w_0(r_o(z), z) = 0$. Equation 6.10 is easily solved by separating the variables in the form $w_0(r, z, t) = \frac{1}{2}\left(W_0(r, z)\mathrm{e}^{\mathrm{i}t} + \tilde{W}_0(r, z)\mathrm{e}^{-\mathrm{i}t}\right)$ where the superscript ( $\tilde{}$ ) denotes the complex conjugate. We present the final solution of the axial velocity:

$$
w_0 = C_1(z)J_0(\mathrm{i}^{3/2}\alpha r) + C_2(z)Y_0(-\mathrm{i}^{3/2}\alpha r) + \frac{\mathrm{iRe}}{\alpha^2}\frac{\partial p_0}{\partial z} \qquad (6.11)
$$

where $J_0$ and $Y_0$ are Bessel functions of the first and second kind, respectively of order 0. The terms $C_1(z)$ and $C_2(z)$ can be easily determined using the boundary conditions. $u_0$ is calculated with the continuity equation 6.8. An analytic expression for $\frac{\partial p_0}{\partial z}$ can be determined by integrating the leading order mass flow $Q_0$:

$$2\pi \int_{r_i}^{r_o} r w_0 \mathrm{d}r = 1 \tag{6.12}$$

The first order continuity and Navier–Stokes equation are written as:

$$\begin{aligned} \frac{1}{r}\frac{\partial}{\partial r}(r u_1) + \frac{\partial w_1}{\partial z} &= 0 &(6.13)\\ 0 &= \frac{\partial p_1}{\partial r} &(6.14)\\ \alpha^2 \frac{\partial w_1}{\partial t} + \mathrm{Re}\left(u_0 \frac{\partial w_0}{\partial r} + w_0 \frac{\partial w_0}{\partial z}\right) &= -\mathrm{Re}\frac{\partial p_1}{\partial z} + \frac{1}{r}\frac{\partial}{\partial r}\left(r \frac{\partial w_1}{\partial r}\right) &(6.15)\end{aligned}$$

with the boundary conditions $u_1(r_i, z) = u_1(r_o(z), z) = 0$, and $w_1(r_i, z) = w_1(r_o(z), z) = 0$, and $Q_1 = 0$. The solution for $w_1$ will have a steady and an unsteady component:

$$w_1(r, z, t) = w_s(r, z) + w_{us}(r, z, t) \tag{6.16}$$

$w_{us}$ is proportional to $\mathrm{e}^{2it}$ and $\mathrm{e}^{-2it}$. Focusing on only the steady streaming component $w_s$ we can reduce equations 6.13–6.15 using the leading order solution:

$$\begin{aligned} \frac{1}{r}\frac{\partial}{\partial r}(r u_s) + \frac{\partial w_s}{\partial z} &= 0 &(6.17)\\ 0 &= \frac{\partial p_s}{\partial r} &(6.18)\\ \frac{1}{r}\frac{\partial}{\partial r}\left(r \frac{\partial w_s}{\partial r}\right) &= \mathrm{Re}\frac{\partial p_s}{\partial z} + \\ &\quad \frac{\mathrm{Re}}{4}\left\{U_0 \frac{\partial \tilde{W}_0}{\partial r} + \tilde{U}_0 \frac{\partial W_0}{\partial r} + W_0 \frac{\partial \tilde{W}_0}{\partial z} + \tilde{W}_0 \frac{\partial W_0}{\partial z}\right\} &(6.19)\end{aligned}$$

where the subscript $s$ always denotes the temporal mean component of the variable. Because the steady pressure gradient is a function of $z$ only, equation 6.19 can be solved by numerical integration. $p_s(z)$ can be determined using the no-flux condition $Q_s = 0$. We note that the steady streaming depends on the $\frac{\partial \tilde{W}_0}{\partial r}$, which changes sign for high $\alpha$ due to the aforementioned annular effect. This qualitatively explains why the steady streaming can change sign in the drift layer. For qualitative analysis, see for example figure 6.2(b) we define a steady streaming stream function $\Psi_s$:

$$w_s = \frac{1}{r}\frac{\partial \Psi_s}{\partial r} \quad \text{and} \quad u_s = -\frac{1}{r}\frac{\partial \Psi_s}{\partial z} \tag{6.20}$$

## 6.3 Key Features of Axi-symmetric Steady Streaming

For illustration purposes we used the theory in the previous section to characterize the flow in an annular gap of slightly more extreme dimensions as the subarachnoid space. We

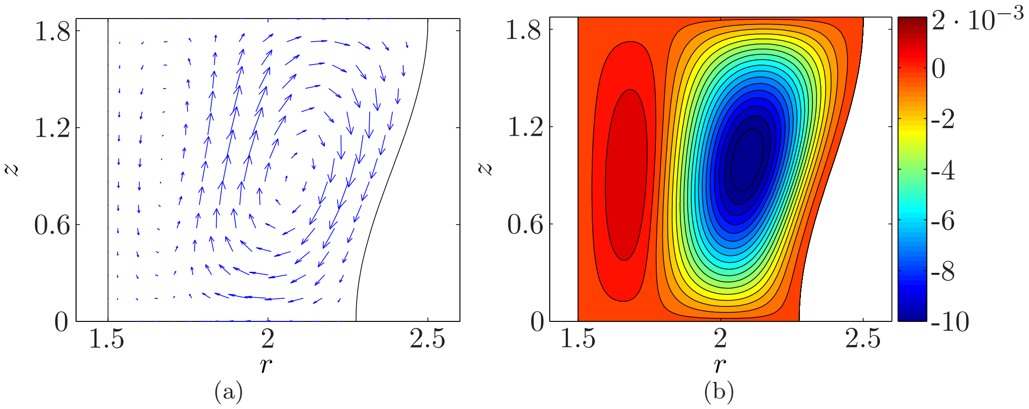

(a) (b)

**Figure 6.2:** Characteristic steady streaming in an annular gap with a slowly varying outer wall ($\epsilon = 0.009$) illustrated with (a) a vector plot of $\mathbf{v_s}(r,z)$, and (b) contours of the stream function $\Psi_s$.

look at a typical case corresponding to $\epsilon = 9 \cdot 10^{-3}$, with an annular gap of the dimension of our experimental setup, namely $r_i = 4.5$ mm and $r_o = 7.5 \cdot 10^{-3}$. We choose $A_{\text{osc}} = 1$, and $\alpha = 7$ to correspond with normal parameters for ITDD conditions. This gives a $\epsilon\text{Re} = 0.44$. We explore a vector plot of the axi-symmetric velocities and the stream function in figure 6.2. Similar to a tapered channel, the velocities in the middle of the annular gap are in the direction of the wider end of the channel. There is an upward velocity near the walls. The velocities near the inner wall are small compared with the velocities near the outer wall.

We explore the influence of the slope of the perturbation $\epsilon$ in figure 6.3 for ITDD relevant parameters. As expected we find that the typical steady streaming velocity is linearly dependent on $\epsilon$. The influence of the non-dimensional stroke distance $A_{\text{osc}}$ is further explored in figure 6.4(a). The axial streaming velocity scales linearly with $A_{\text{osc}}$ instead of $A_{\text{osc}}^2$ as should be expected based on the quadratic nature of the convective terms. This is explained because $w_s$ is a non-dimensional quantity, so that $\hat{w} = \omega d_{\text{osc}} w$ depends quadratically on $d_{\text{osc}}$.

The non-linear relation between the maximum positive velocity and $f_{\text{osc}} \propto \alpha^2$ is shown in figure 6.4(b), again deviating from the order of magnitude analysis. Similarly to the amplitude one should multiply the non-dimensional quantity to obtain the correct order of magnitude of $V_s$. However the $\alpha$ also determines the specific flow pattern of the steady streaming. Based on conclusions from the tapered channel steady streaming, we expect that for high $\alpha$ the flow field reverses in the midline for a fixed tidal volume. This explains why, at higher frequencies, the maximum positive velocity diminishes. A higher $\alpha$ was not pursued because the asymptotic relation is not valid for high Re and because it will be shown in the following chapters that for typical ITDD parameters this model suffices. More practically the Bessel functions are delicate to calculate for high $\alpha$ requiring more precise calculations. Already the final expressions for $w_s$ can only be numerically evaluated because we could not find an analytic expression for the steady streaming pressure gradient. A numerical approach would therefore be preferred to study the effect of a higher $\alpha$.

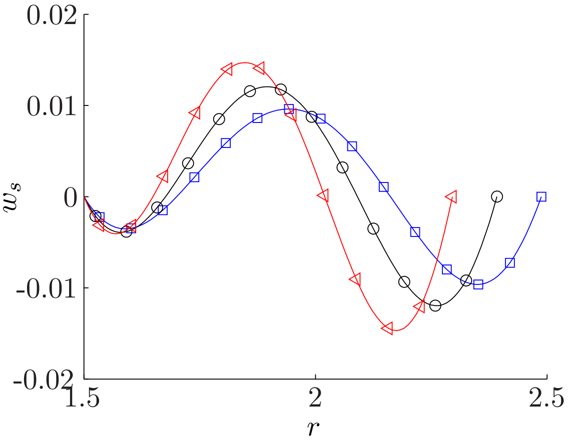

**Figure 6.3:** The steady streaming velocity $w_s$ vs. $r$ in the middle of a geometry (r,$\hat{z} = L_c/2$) with a sinusoidally varying outer wall defined by equation 4.1 with $\epsilon = 0.001$ (□), 0.009 (○), and 0.017 (◁) for $L = 75$ mm, $r_o = 7.5$ mm, and $r_{\mathrm{H}} = 3$ mm. The stroke distance is $d_{\mathrm{osc}} = 5$ mm, and $\alpha = 8.9$. The positive velocity is towards the wider end of the annular gap.

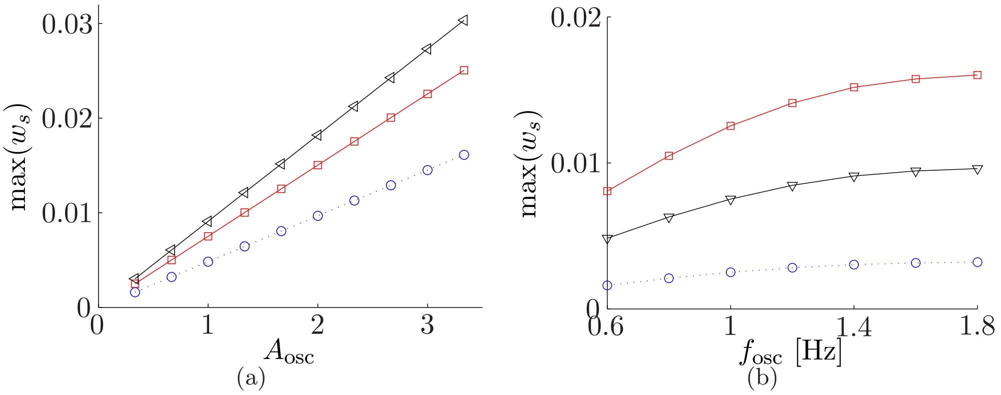

**Figure 6.4:** The maximum value of $w_s > 0$ inside the entire geometry, $\max(w_s)$ vs. (a) the non-dimensional stroke distance $A_{\mathrm{osc}}$ for $\epsilon$ =0.009, and $\alpha = 6.7$ (○) and $\alpha = 9.0$ (□), and $\alpha = 10.6$ (◁), and (b) $f_{\mathrm{osc}} \propto \alpha^2$ for a non-dimensional stroke distance $A = 0.33$ (○), $A = 1.00$ (▽), and $A = 1.67$ (□). We may observe a linear dependence in (a), which is due to the nondimensionalization of $w_s = \hat{w}_s/(\omega d_{\mathrm{osc}})$. Hence the dimensional $\hat{w}_s$ is proportional to $d^2_{\mathrm{osc}}$. For higher $\alpha$ the maximum tends towards negative values.

# Chapter 7

# Numerical Investigation of Steady Streaming

## 7.1 Introduction

The axi-symmetric theory cannot explain 3D steady streaming phenomena expected from the presence of the catheter and the intricate true human spinal canal geometry. Therefore, numerical study was performed using a finite volume commercial software package (Fluent®) to investigate these phenomena. Although we focused our numerical study on the steady streaming related to the presence of the catheter, we also made an attempt to calculate the velocity profile in a geometry that was extracted from the Visible Human database [60]. This case study included the influence of the non-singly harmonic waveform (see figure 4.4) in a straight geometry. We usually characterize the flow field of the numerical results with the non-dimensional root mean square velocity $\mathbf{v}_{\text{rms}}$,

$$\mathbf{v}_{\text{rms}}(r,\theta,z) = \frac{\hat{\mathbf{v}}_{\text{rms}}(r,\theta,z)}{\omega d_{\text{osc}}} = \sqrt{\frac{1}{n}\sum_{i=1}^{n} \mathbf{v}(r,\theta,z,t_i)^2} \tag{7.1}$$

and the non dimensional temporal mean of the velocity field $\bar{\mathbf{v}}$, equivalent to steady streaming vector:

$$\bar{\mathbf{v}}(r,\theta,z) = \frac{\hat{\mathbf{v}}_s}{\omega d_{\text{osc}}} = \frac{1}{n}\sum_{i=1}^{n} \mathbf{v}(r,\theta,z,t_i) \tag{7.2}$$

where $[t_1, t_n]$ corresponds to a single cycle. Although the numerical approach is certainly more appropriate to describe complex flow phenomena it is too expensive to compute the diffusion of a scalar in such geometries over long time periods of the order of an hour. This study was only performed to support experimental observations and was not intended as a full parameter study of the steady streaming in ITDD.

## 7.2 Case I: Straight Annular Gap with Injection Catheter

The basic geometry is a constant cross section annular gap with $r_i = 4.5$ mm, $r_o = 7.5$ mm and is 70 mm tall. The 1.4 mm diameter, rounded tip, injection catheter was placed parallel to the cylinders in the middle of the annular gap. This corresponds exactly to the experimental straight tube geometry. The working fluid was water with a kinematic viscosity of $\nu = 6.58 \cdot 10^{-7}$ m$^2$/s. The imposed frequency was $f_{\text{osc}} = 1$ Hz, and the stroke distance was $d_{\text{osc}} = 2.1$ mm.

The plane parallel to the axis and dividing the catheter in two $(x, y = 0, z)$, or $(\theta = 0 \vee \theta = \pi)$ was used as a symmetry plane. A non-structured 2.5 million cell mesh consisting

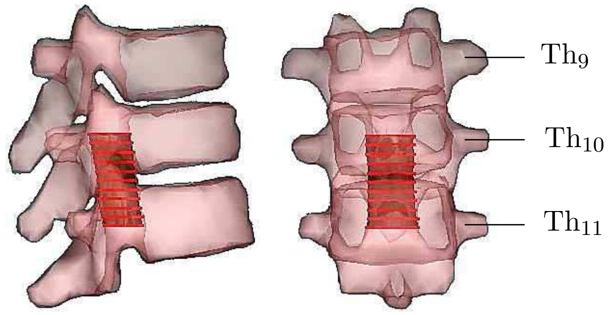

**Figure 7.1:** The extracted human-like geometry that was used for the numerical computation as shown inside the spinal canal. This extraction is based on the Visible Human database. The red contours show the manually defined position of the arachnoid, which was subsequently used to construct the computational grid.

primarily of tetrahedral cells was created. The unsteady boundary layer increases the demands on the computational grid. The maximum mesh density was $\sim 10$ per annular gap cross section but refined near the catheter tip. Far away from the catheter, we created a structured grid to limit the number of cells. A picture of the grid is shown in figure 7.7. Approximately 90% of the elements have an equiangle skew of 0.5, and the worst element has an equiangle skew of 0.82. The calculation time on 6 Pentium 4 computers was roughly 5 days.

For qualitative post treatment of the steady streaming, we extracted slices that we interpolated onto a structured grid. In this chapter we analyze the flow in the symmetry plane on the side of the catheter ($\theta = 0,\ 4.5 \leqslant r \leqslant 7.5$ mm), and the mid-plane of the annular gap ($-\pi \leqslant \theta \leqslant \pi,\ r = 6$ mm). The latter plane is shown explicitly in a top projection of the geometry in figure 4.2.

## 7.3 Case II: Geometry From Visible Human Database

To date, this case corresponds to the most accurate simulation of steady streaming inside an actual human subarachnoid space. The variations in the arachnoid cross section due to nerves branching out of the subarachnoid space at regular intervals are expected to be the primary source of the variation. The human-like geometry was therefore taken to be at least the height of a single vertebral body. We constructed a computational grid that was based on manually identified cross sections of the spine and arachnoid between vertebral levels $Th_{10}$ and $Th_{11}$ in the Visible Human database. Additional steady streaming can be expected from the non-centric position of the spine. Although this model is more advanced geometrically than case I, section 7.2, it is still highly simplified. It does not include the nerve branches themselves, the denticulate ligament, or for example the movement of the spine.

To reduce steady streaming due to entrance effects, such as described by Goldberg [27], the top and bottom surfaces were extended in the local average direction of the arachnoid and spine. The entire computational grid is shown in figure 7.2. It is non-conformal between the structured grid in the extended parts and the non-structured grid inside the

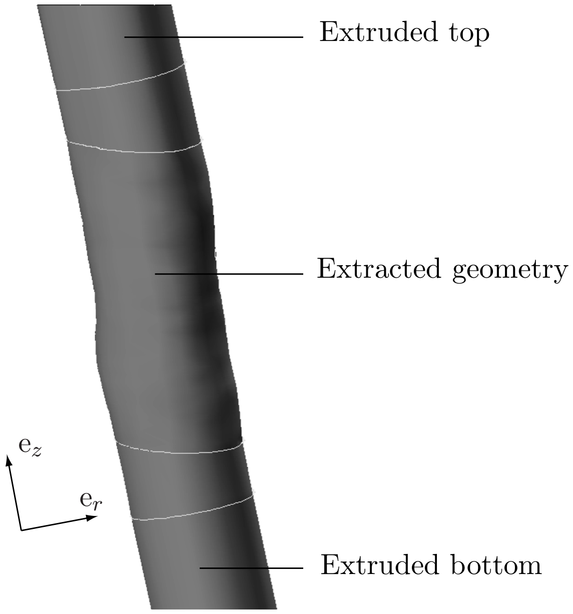

**Figure 7.2:** The computational grid for the human-like geometry. The top and bottom sections were extruded from the top and bottom surface of the extracted geometry. These sections are made with a structured grid, while the grid in the extracted geometry is unstructured.

human-like geometry. The total grid is composed of 2.8 million cells. Only one simulation was done with the non-singly harmonic waveform shown in figure 4.4, characterized by a fundamental frequency of $f_{\mathrm{osc}} = 0.77$ Hz and a stroke distance of $d_{\mathrm{osc}} = 12.89$ mm. The calculation time on 6 Pentium 4 computers was roughly one week.

Although the shape of this extracted geometry is largely cylindrical, the azimuthal variations in cross section and the varying position of the spine inside the subarachnoid space imply that the flow becomes 3D. For post treatment we extracted several planes (see figure 7.7) onto which we projected the velocity profiles. We independently study the velocity parallel ($\mathbf{v}_{||}$) and perpendicular ($\mathbf{v}_{\perp}$) to these extracted planes. $\mathbf{v}_{\perp}$ is roughly equivalent to $e_\theta$, while the components of $\mathbf{v}_{||}$ qualitatively correspond to the axial $\mathbf{e}_z$ and the radial $\mathbf{e}_r$ directions.

## 7.4 Numerical Method and Validation

The solver for the continuity and Navier–Stokes equations was implicit and fully 3D. The unsteady formulation was of first order implicit and a relatively small constant time step of 0.01 s was used. Because the time derivative at $t = 0$ is not known, 3 full cycles were calculated. The first cycle was discarded, and no significant differences between the velocity profiles in the second and third cycle at the same phase could be identified. The pressure is internally calculated using the continuity equation with the Pressure-implicit Splitting of Operators (PISO) [38]. The momentum equation is discretized with a first order upwind scheme which assumes that all quantities at the surface of the cell are equal to the quantity at the cell center. The pressure was discretized using the momentum

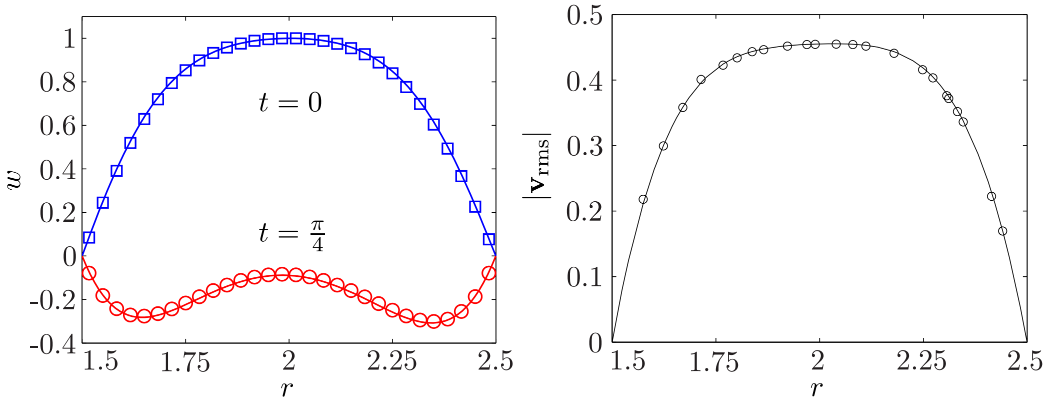

(a) (b)

**Figure 7.3:** (a) The numerical velocity profile at two different phases in the oscillation cycle, and (b) $|\mathbf{v}_{\text{rms}}|$. The profiles were extracted from the case I geometry far away from the catheter so that they can be compared with the analytical Stokes solutions (solid lines). The oscillation parameters were: $f_{\text{osc}} = 1$ Hz, and $d_{\text{osc}} = 2.1$ mm.

coefficients at the cell's surface. The calculations were done in double precision, and the solution was judged converged if the scaled residuals were lower than $10^{-6}$. This criterion was met for nearly all time steps, except at for a few points around the turning points of the oscillation, i.e. where the velocities were lowest.

To help the solver converge more rapidly, the analytical axi-symmetric velocity profile was given as a boundary condition on the top surface. The other side, which has a protruding catheter is specified with a constant pressure. No-slip conditions are enforced on the walls of the domain.

The accuracy of the method was investigated by comparing the time dependent velocity profile and $|\mathbf{v}_{\text{rms}}|$ to the analytical Stokes solution for oscillatory flow in an annular gap. This is shown in figure 7.3. The profiles were extracted from the numerical solution on a single cross section of the grid far away from the catheter tip. The error is time dependent and of the order of $10^{-3}$, which, given the first order numerical schemes and the quality of the grid, is acceptable. No effort was made to improve on this accuracy. The mean velocity $\bar{\mathbf{v}}$ at the given cross section is $O(10^{-6})$. The error on the mean velocity field was not specifically investigated, but should be of the same order as error on the $|\mathbf{v}_{\text{rms}}|$ profile.

## 7.5 Results: Case I

$\bar{\mathbf{v}}$, or the steady streaming $\mathbf{v}_{\mathbf{s}}$, is numerically zero $O(10^{-6})$ except for the region immediately surrounding the catheter tip. The steady streaming in the planes $(r = 2, \theta, z)$, and $(r, \theta = 0, z)$ is shown as a vector plot of the cylindrical velocities in figure 7.4. A recirculation cell exists on both sides of the catheter. The downwards draft of the recirculation cell is in the region directly above the catheter tip. This negative axial velocity is carried through on both sides of the catheter in the symmetry plane.

The magnitude $|\bar{\mathbf{v}}|$ of the streaming velocities in the recirculation cells is explored in

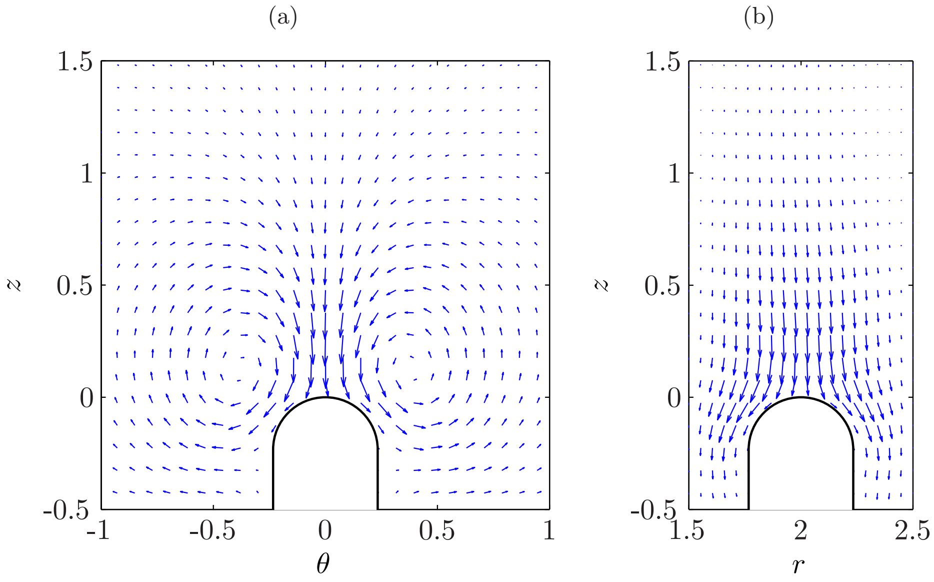

**Figure 7.4:** A vector plot of the steady streaming ($\bar{\mathbf{v}}$) in cylindrical coordinates in the plane (a) $(r = 2, \theta, z)$, and (b) $(r, \theta = 0, z)$. The magnitude of the plotted vectors is exaggerated for easier interpretation.

figure 7.5. The maximum of the magnitude of the steady streaming is nearly 10% of the characteristic velocity defined by $\omega d_{\text{osc}}$ corresponding to approximately 1 mm/s. This maximum has a large negative axial component and is located directly above the catheter. Smaller steady streaming velocities ($< 0.005\ \omega d_{\text{osc}} \approx 0.05$ mm/s), which correspond to the limit of the numerical precision, can be detected some 5 mm above the catheter tip. Similar low amplitude velocities can also be seen to extend a similar distance in the $\theta$-direction. This gives rise to a characteristic mushroom shape where the catheter serves as the stalk. The upward velocities on either side of the catheter are lower in magnitude than the central downward velocity.

Although steady streaming will dominate the dispersion of the dye in ITDD, $|\mathbf{v}_{\text{rms}}|$ is important to estimate the effect of the enhanced mixing near the catheter. It is especially important because at the height of the injections ports at ($z = -4$, $\hat{z} = -12$ mm) the steady streaming is numerically zero. The primary effect of the catheter is to obstruct the flow. The RMS velocity $|\mathbf{v}_{\text{rms}}|$ in the symmetry plane is therefore considerably lower than in the free stream. In order to respect the continuity equation, the fluid must accelerate away from the symmetry plane at $z \leqslant 0$. The higher RMS velocity is especially evident in the zone directly adjacent to the catheter. This increase in local velocity increases the local $A_{\text{osc}}$. This might be significant in relation to enhanced mixing because, according to equation 3.20, $D_{\text{enh}} \propto \alpha A_{\text{osc}}^2$ for high $\alpha$ and Sc. The effect of enhanced mixing near the catheter could therefore be locally increased.

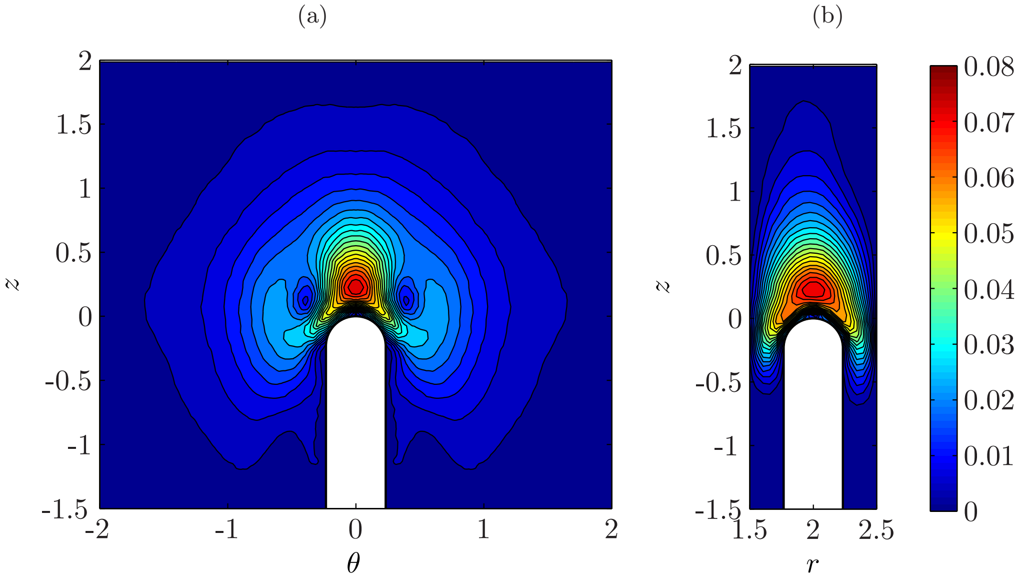

**Figure 7.5:** The magnitude of the steady streaming $|\bar{\mathbf{v}}|$ in the plane (a) $(r = 2, \theta, z)$, and (b) the symmetry plane $(r, \theta = 0, z)$. $|\bar{\mathbf{v}}|$ was normalized to $\omega d_{\text{osc}}$. The maximum streaming magnitude is 0.08 $\omega d_{\text{osc}}$ .

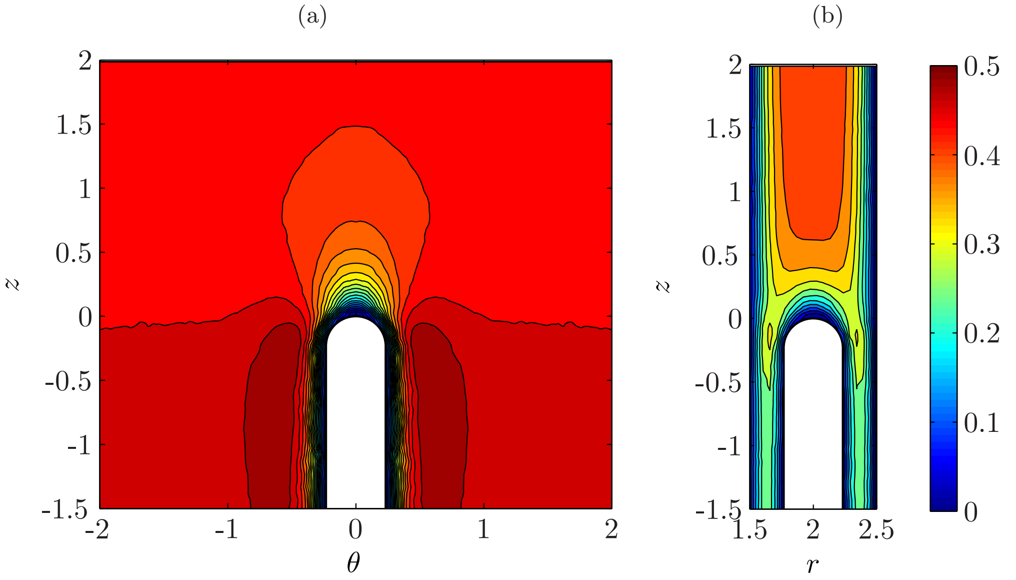

**Figure 7.6:** A contour plot of $|\mathbf{v}_{\text{rms}}|$ in the plane (a) $(r = 2, \theta, z)$, and (b) $(r, \theta = 0, z)$. $|\mathbf{v}_{\text{rms}}|$ was normalized to $\omega d_{\text{osc}}$.

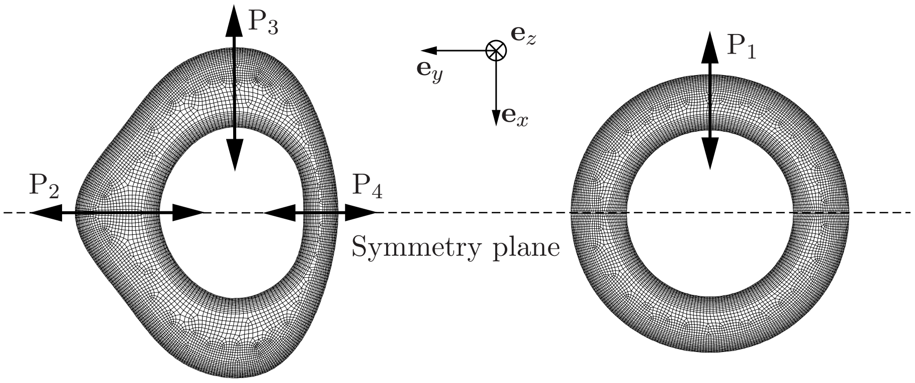

**Figure 7.7:** The computational grids of the top surface of the human-like geometry and of the experimental $r_{\mathrm{H}} = 3$ mm straight annular gap. Lines P$_1$ to P$_4$ refer to cross sections that are used for comparison of the RMS velocity with theory. All computations were performed using the indicated symmetry plane.

## 7.6 Results: Case II

The size of the annular gap is dependent on $\theta$, even in the extruded top and bottom parts of the geometry. We therefore first investigated the influence this has on $|\mathbf{v}_{\mathrm{rms}}|$. To this effect we extracted velocity profiles from $(r, z)$-projections taken from the extruded top part of the mesh. The velocity profiles are taken perpendicular to the axis of the geometry, as is shown in figure 7.7.

We also investigate $|\mathbf{v}_{\mathrm{rms}}|$ of the human-like waveform inside a constant cross section annular gap. Similar to figure 7.3, we compare the velocity profiles to a fitted solution of the unsteady Stokes flow inside an annular gap. The $\alpha$ that was used for the fit was based on the local channel width and the fundamental frequency of the non-singly harmonic waveform. The shift of each curve in $r$ corresponds to the slight differences of the inner radius, or thickness of the spinal cord with $\theta$. The fits are not perfect, but this can be expected because the fitted function is based on an axi-symmetric annular gap. Qualitatively, however, the fit is quite acceptable. The pronounced flattening of $|\mathbf{v}_{\mathrm{rms}}|$ observed in wider sections of especially cross sections P$_2$ and P$_3$ can therefore be explained to leading order by the local hydraulic radius of the annular gap, but would require higher order analytical models to correct the $\theta$-dependence of the geometry to increase the precision. Furthermore, comparison with figure 7.3 shows that the only effect of using the non-singly harmonic is to slightly flatten the RMS profile. It is noted that the non-singly harmonic profile should also induce small magnitude steady streaming due to the different size of the boundary layer in time, notably because of the asymmetry of the waveform between positive and negative mass flow. Unfortunately, the accuracy of our numerical method is not high enough to resolve this steady streaming.

Instead we focus our attention on the steady streaming generated by the geometry itself. We examine the velocity profiles on two different planes that are labeled P$_1$ and P$_3$ in figure 7.7. We examine the velocity profiles inside the central human-like part of the grid, at lower $z$ than in the extended top section. We examine the steady streaming in these planes in figures 7.9 and 7.10 by looking at a vector plot and the magnitude of the velocities parallel to these planes $(\mathbf{v}_{||})$, the RMS velocity $|\mathbf{v}_{\mathrm{rms}}|$, and finally the magnitude

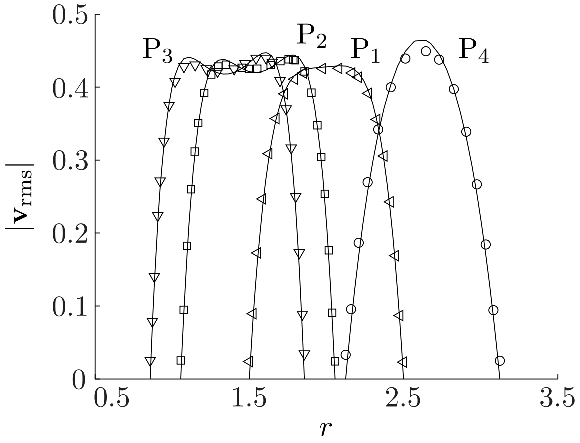

**Figure 7.8:** The RMS velocity profile $|\mathbf{v}_{\mathrm{rms}}|$ of the non-singly harmonic human waveform on a line extracted from $P_1$ inside a perfect annular gap with the same dimensions as the experimental setup, and $P_2$–$P_4$ from different locations of the extracted top part of the human geometry grid. The letters assigned to each curve correspond to the specific cross sections shown in figure 7.7. The fitted profiles are calculated using the unsteady Stokes solution of an oscillatory waveform in an axi-symmetric annular gap with $\alpha$ based on the fundamental frequency of the waveform $f_{\mathrm{osc}}$ and the local radii of the numerical grid.

of the velocity perpendicular to the plane ($\mathbf{v}_\perp$). Both figures use the same color scales for easier direct comparison. First we observe that the steady streaming in the planes corresponds qualitatively to the axi-symmetric theory presented in section 6. The velocity on the midline is in the direction of the wider side ($\mathbf{e}_z$), and in the opposite direction near the walls ($-\mathbf{e}_z$). Locally $\left|\bar{\mathbf{v}}_{||}\right|$ can be as much as 0.04, which represents 50% of the steady streaming that is generated by the injection catheter placed inside the constant cross section annular gap. Higher steady streaming velocities, such as seen at for example $r = 1.5$ and $z = 0.5$ in figure 7.9(b), and $r = 2.7$ and $z = 2$ in figure 7.10(b), seem to be associated with a higher local slope of the wall, and higher velocities perpendicular to the plane $|\bar{\mathbf{v}}_\perp|$.

$\left|\bar{\mathbf{v}}_{||}\right|$ is on average the same order of magnitude as predicted by theory, $O(0.01 - 0.02)$. The steady streaming is lower in the wider cross section shown in figure 7.10, which can be qualitatively understood by defining a Womersley number $\alpha$ based on the local hydraulic radius of the annular gap. Typical steady streaming velocities extend over the entire cross section for both planes. We observe that $|\bar{\mathbf{v}}_\perp| \approx 0.25\left|\bar{\mathbf{v}}_{||}\right|$. This partly explains why the axi-symmetric model can still be used to interpret the main effect. As can be expected, the RMS velocity is higher in narrower sections of the domain. The flattening of $|\mathbf{v}_{\mathrm{rms}}|$ in wider sections of the channel can be explained by defining a local Womersley number. This was already shown to be relatively accurate in figure 7.8 for the RMS velocities in the extended top section of the geometry.

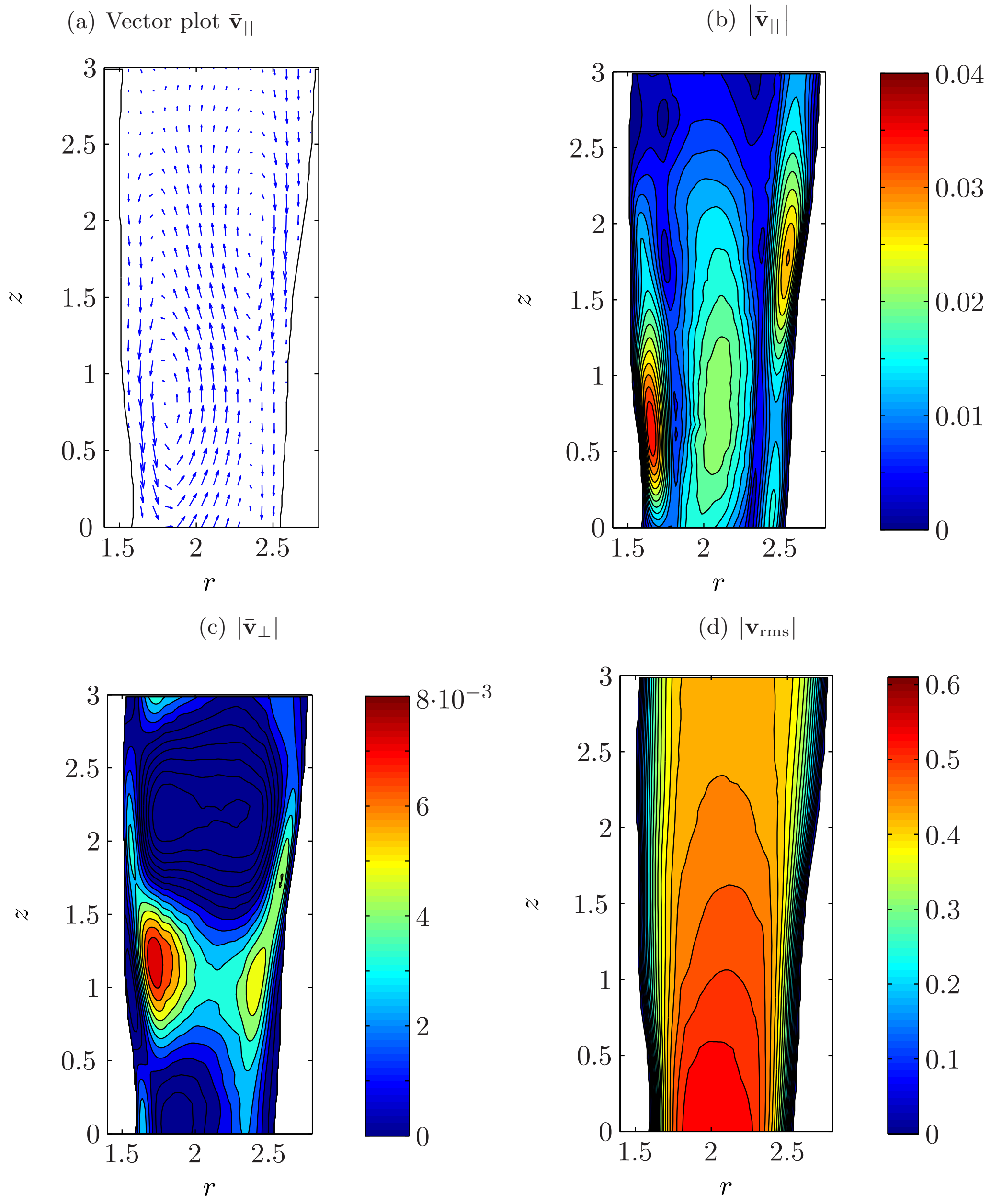

(a) Vector plot $\bar{\mathbf{v}}_{||}$

(b) $\left|\bar{\mathbf{v}}_{||}\right|$

(c) $|\bar{\mathbf{v}}_{\perp}|$

(d) $|\mathbf{v}_{\mathrm{rms}}|$

**Figure 7.9:** An investigation of the velocities calculated in plane $P_4$ from figure 7.7. (a), (b), and (d) show a vector plot, the magnitude and the RMS of the unsteady velocities that are parallel to the extracted plane ($\mathbf{v}_{||}$), respectively. (c) shows the component of the mean velocity field perpendicular to the extracted plane ($\mathbf{v}_{\perp}$).

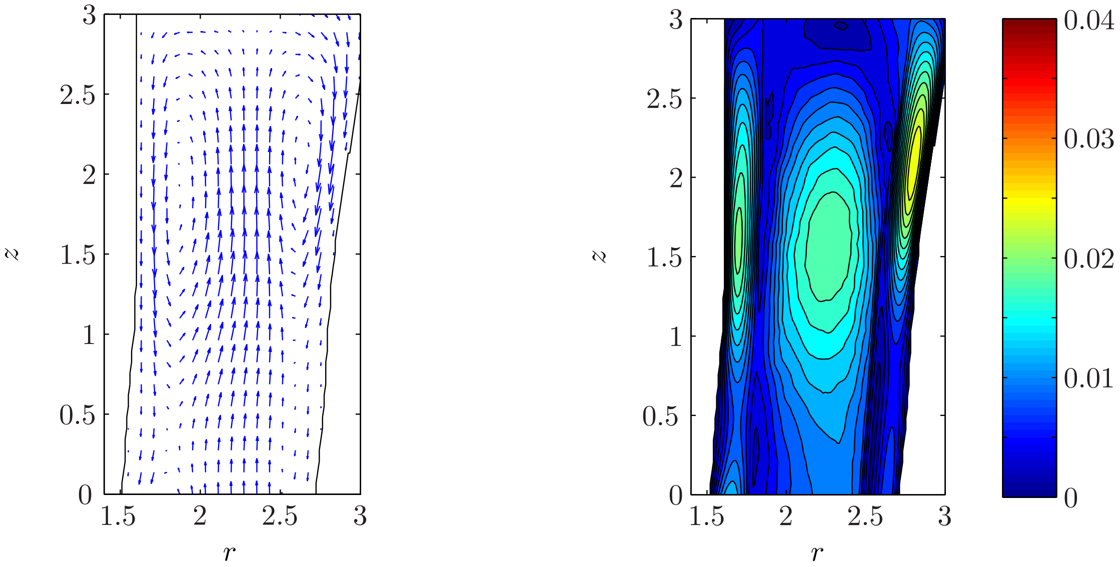

(a) Vector plot $\bar{\mathbf{v}}_{||}$ (b) $\left|\bar{\mathbf{v}}_{||}\right|$

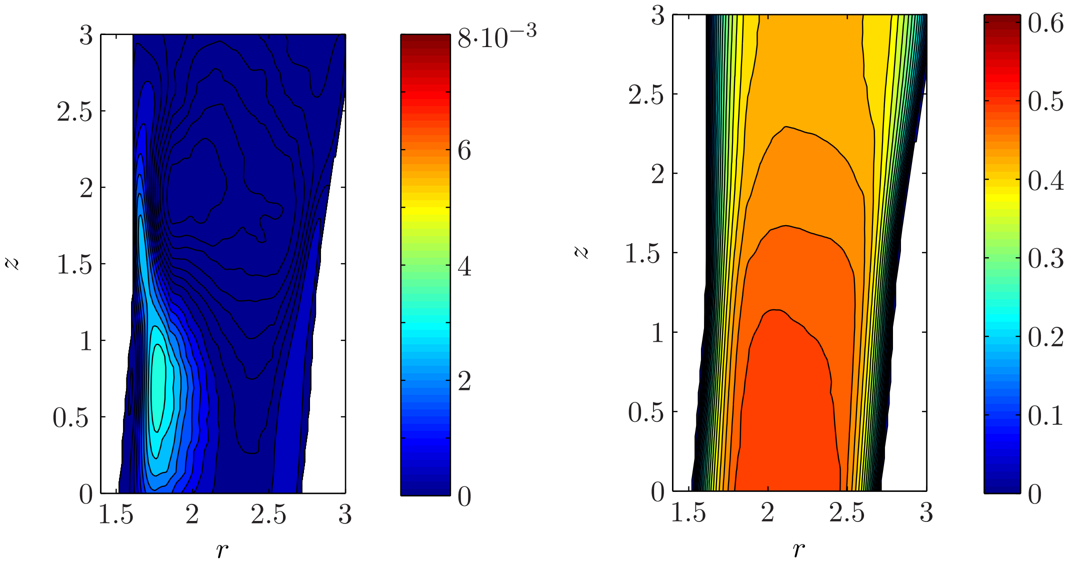

(c) $|\bar{\mathbf{v}}_{\perp}|$ (d) $|\mathbf{v}_{\mathrm{rms}}|$

**Figure 7.10:** An investigation of the velocities calculated in the plane $\mathrm{P}_3$ from figure 7.7. (a), (b), and (d) show a vector plot, the magnitude and the RMS of the unsteady velocities that are parallel to the extracted plane ($\mathbf{v}_{||}$), respectively. (c) shows the component of the mean velocity field perpendicular to the extracted plane ($\mathbf{v}_{\perp}$).

## 7.7 Summary of the Numerical Study

Numerical simulations are well suited to study the steady streaming in complex geometries such as the human subarachnoid space. However, with our relatively large grids generating results requires considerable calculation power. If possible, it would be beneficial to work on slightly simpler, structured grids. Furthermore, with our first order formulation the accuracy is limited $O(10^{-3})$. Nonetheless the results have been useful in modeling the steady streaming. We find that the introduction of an ideal catheter generates steady streaming at the tip over at least 5 mm. The maximum mean velocity is 0.08 $\omega d_{\mathrm{osc}}$. Furthermore we have hypothesized that the increased RMS velocities near the catheter are likely to have an influence on the initial dispersion of the drug through enhanced diffusion.

Case II computations with a geometry extracted from the Visible Human database showed that although the mean velocity field becomes slightly 3D, the axi-symmetric analytical model can still be used to qualitatively understand it. The observed recirculation cells are characterized by a midline velocity in the direction of the wider end of the channel, and in the opposite direction near the walls. The magnitude of the steady streaming generated by the non-singly harmonic waveform in this geometry is smaller than the streaming induced by the catheter tip but extends over a larger distance. The steady streaming becomes more 3D with an increased magnitude near higher slopes of the walls. The latter observation is consistent with the axi-symmetric analytical model's prediction that the steady streaming scales with the slope ($\epsilon$). Because the 3D component of the steady streaming is generally weak, we conclude that it is reasonable to model small variations of the subarachnoid space using an axi-symmetric slowly varying cross section. It will be shown in part II that both the catheter tip and slowly varying cross section have an important influence on the dispersion of the local anesthetic. We note however that the investigated geometry is still a relatively simple model of the actual subarachnoid space, and is only representative of a single vertebral body.

# Chapter 8

# Experimental Investigation of Steady Streaming

In this chapter we report on a series of particle image velocimetry (PIV) measurements aimed at:

- confirming the axi-symmetric theory presented in chapter 6,
- measuring the steady streaming near the catheter tip to compare with the numerical results shown in section 7.5, and
- investigating the combined effect of steady streaming generated by the catheter tip placed inside a slowly varying cross section annular gap.

In section 8.2 we discuss how we optically used the setup described in 4 to perform the PIV measurements. In section 8.2 we briefly describe the procedure of the experiments, and in section 8.3 we discuss the results.

## 8.1 Notes on the Setup

We used the experimental setup described in detail in section 4 to performed 2D DPIV measurements. The experiment was configured with or without the metallic catheter inside a constant or slowly varying cross section annular gap. Only one of the two scanning mirrors described in figure 4.6 was used to create the laser sheet. We only considered $(r, \theta = \mathrm{Cst}, z)$-planes because the position of the walls are relatively well defined. Furthermore, compared to for example the $(x = \mathrm{Cst} \neq 0, y, z)$-plane, the results are easier to compare with the axi-symmetric theory. We changed the orientation $(\theta)$ of the light sheet by rotating the experiment about its $z$-axis. This resulted in a better quality light sheet than using both scanning mirrors simultaneously to scan the light sheet at an angle, which also requires changing the camera position.

In any cylindrical tube there are hidden regions near the outer wall that the camera cannot image. Using ray tracing, Lowe and Kutt [43] showed that prevalence of these regions depends, logically, on the thickness of the tube wall, the refractive indices of the media, and the camera. Based on images taken of a regular grid, we estimate the hidden region near the outer wall to be of order of our vector resolution. Furthermore, we could not identify any grid deformations due to the cylindrical tubes. This was not different in a slowly varying cross section annular gap.

We scan the laser sheet from above $(\mathbf{e}_z)$, which implies that the laser has to travel through roughly 15 cm of water that is densely seeded. This scatters, and consequently widens the laser beam $(d_{\mathrm{plane}})$ considerably and decreases its intensity with distance.

Although we had sufficient laser power to compensate for the decrease in intensity we worked at the limit of our optical system. We attempted to scan the laser beam from the side rather than from the top, but it was not possible to avoid reflections off the inner glass tube in our optically unmatched system, causing secondary laser planes in our image.

Because the laser sheet comes from above the test section, we must avoid shaded areas in the varying cross section geometries. To this effect we limit ourselves to constricted annular gaps shown qualitatively in figure 4.2 and described by:

$$r = r_o \pm \frac{\Delta r_o}{2}\left(1 - \cos\left(2\pi \hat{z}/L\right)\right), \qquad \hat{z} \in [0, L] \tag{8.1}$$

where $r_o = 7.5$ mm is the external radius of the standard constant cross section annular gap. We place the catheter above the midpoint of the geometry, roughly at $\hat{z} = 3L/4$. We used geometries with $\Delta r_o = 0.7$ mm, and $L \in \{25, 50, 75\}$. Although we decided to use our optically unmatched system and scan from above for practical and time reasons, we acknowledge that an optically matched system can possibly yield superior results.

## 8.2 Procedure

By zooming in on the test section we obtained a resolution of 16 $\mu$m per pixel and we used 30 $\mu$m mean diameter polyamide seeding particles (PSP). To make the particles neutrally buoyant the working fluid was a mixture of 14% Glycerol in distilled water. This increases the viscosity, even though we kept this increase to a minimum by working at 37°C. To keep the Womersley number $\alpha = r_{\mathrm{H}}\sqrt{\omega/\nu}$ in the clinically relevant range we compensated for the increased viscosity $\nu$ by increasing the driving frequency $f_{\mathrm{osc}}$, specifically to 1.3 and 2.6 Hz. We note that we could not increase the temperature further to reduce the viscosity without generating temperature induced buoyancy of the particles.

The instantaneous velocity profile was calculated with cross-correlations using an open source Matlab code MatPIV [67]. This code uses a multiple pass algorithm whereby the interrogation window (IW) size can be decreased at each iteration. For each pass the algorithm calculates the cross-correlation between the IW from the first image with an offset IW in the second image. The offset is equal to the displacement vector calculated from the previous pass. In comparison to a commercial code that uses image deformation, it obtained only a slightly lower accuracy at much quicker calculation time. Our typical acquisition frequency was 10 Hz, and we used phase-averaging to calculate the temporal velocity field. To obtain a convergence to within 5% for all phases outside the Stokes boundary layer, 1024 image pairs were taken per phase. The weak steady streaming component was measured by computing the temporal mean of the velocity profile.

We zoomed in on a small region ($3 \times 8$ mm) of the annular gap. Using a final IW size of 16x16 pixels with an overlap of 50% a sampling of $\sim 20$ points per cross section was obtained. We roughly had 4-8 particles per final IW. The time between two successive images $\Delta t = 3.6$ ms was not changed during the oscillation cycle. Therefore the maximum particle displacement and shear per IW varies with the phase of the oscillation cycle. The maximum particle displacement observed is 12 pixels, or 75 % of the final IW size. To avoid loosing particles from our final pass IW, we typically calculated 5 passes, starting with an IW size of $64 \times 64$ pixels. We estimate the maximum shear from the RMS velocity profile shown in figure 7.3(b) as $\omega d_{\mathrm{osc}}/2$ per a third of the channel. With our highest intensity

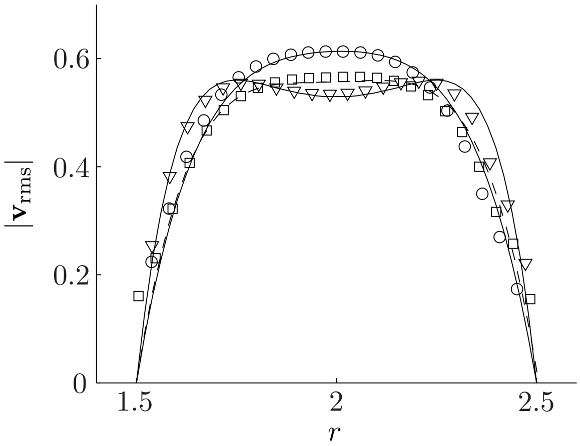

**Figure 8.1:** The measured $|\mathbf{v}_{\mathrm{rms}}|$ vs. $r$ for the 1.3 Hz (□), 2.5 Hz (▽) singly harmonic, and 1 Hz human-like waveform (○) in a straight tube as compared with the analytical Stokes solution. The scattering of the laser sheet and high shear in the boundary layers limit the accuracy near the wall, while a 5% accuracy is obtained in the rest of the domain. Error bars (Typically ±5%) are omitted for clarity.

oscillation $d_{\mathrm{osc}} = 5$ mm, $f_{\mathrm{osc}} = 2.5$ Hz, and $r_{\mathrm{H}} = 3$ mm we obtain $\frac{\partial w}{\partial r} \approx 40\ \mathrm{s}^{-1}$. This is relatively large ($\frac{\partial w}{\partial r}\Delta t = 0.14$), but is representative only for a third of the oscillation cycle. Furthermore, because of the aforementioned scattering of the laser sheet the image quality in the boundary layers is poor, especially near the inner tube $r_i = 4.5$ mm. The relatively high shear was therefore not the primary limiting factor in resolving the boundary layers. Spurious velocity vectors are identified using a variety of filters; a signal to noise filter, a global histogram operator, and a local median and moving average filter. Outliers, typically less than 5% of the total amount of vectors, are replaced by linear interpolation.

## 8.3 PIV Results

To investigate the accuracy of our PIV measurements, we compared the measured root mean square velocity $|\mathbf{v}_{\mathrm{rms}}|$ profile in a straight tube to the analytical Stokes solution. This is shown in figure 8.1. Although the overall error is acceptable, the error in the Stokes boundary layer can be as much as 20%. This can be explained by the limited resolution of our optical system and the small error in determining the boundaries of our system.

Figure 8.2 shows the axial component of the steady streaming $w_s$ in a cross section of the annular gap with a slightly varying outer diameter. From the analytical work in chapter 6 we expect the non-dimensional steady streaming velocity to scale with $\epsilon\omega d_{\mathrm{osc}}$, and therefore non-dimensionalize accordingly. As expected for moderate Womersley numbers $\alpha$ the midline velocity is in the direction of the wider end of the channel and towards the narrow end in the boundary layers. As was shown in section 6.2, the steady streaming depends linearly on $\epsilon$, so we only need one analytical model plot in figure 8.2. By examining the residual velocity in the constant cross section geometry, we estimate the error on the computed mean velocity to be ±0.003. Although it is clear that the steady streaming in the varying cross section geometries corresponds qualitatively to the asymptotic theory,

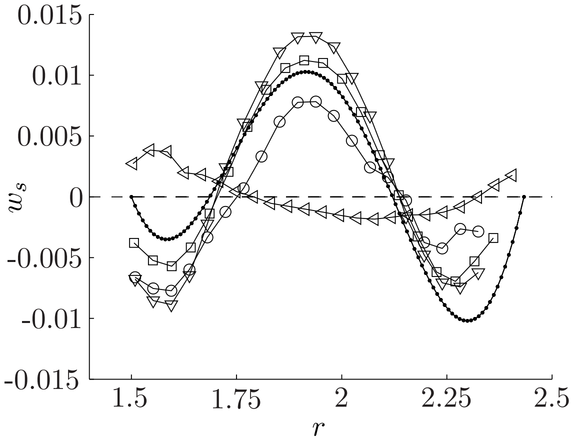

**Figure 8.2:** The measured axial steady streaming velocity $w_s = \hat{w}_s/(\omega d_{\text{osc}}\gamma)$, where $\gamma = 0.019/\epsilon$ is ratio of $\epsilon$ to the smallest slope ($\epsilon = 0.019$) included. $\alpha = 8.9$ for $\epsilon$ is 0 (◁), 0.019 (○), 0.028 (▽), and 0.056 (□). The dotted solid line indicates the theoretical prediction of chapter 6. Although the experimental error (±0.003) is large, we note that the curves are in qualitative agreement.

the error inside the boundaries is too large to make a more quantitative comparison with theory.

Figure 8.3 shows the magnitude of the steady streaming $|\mathbf{v_s}(r, z)|$ generated by the catheter compared to the steady streaming generated by the slowly varying wall. We note that $\mathbf{v_s}$ is based on only 2 components parallel to the acquired PIV images. The same figure also shows the effect of placing a catheter in a slowly varying cross section annular gap. First, we note the excellent qualitative agreement of $|\mathbf{v_s}|$ near the catheter tip shown in figure 8.3(d) with the numerically calculated steady streaming magnitude shown in figure 7.5(b). This is in spite of using different $\alpha$ and $A_{\text{osc}}$. The maximum steady streaming magnitude $\max(|\mathbf{v_s}|)$ is 0.10 (experimental) compared to 0.08 (numerical), and the extent of the influence is also similar. An exact comparison is difficult because of the limited accuracy of our method (±0.003) and catheter movement. This movement is imparted on the catheter by the piston. Furthermore our error is large in areas near the catheter because of shear.

As predicted by the numerical work in the previous chapter, the typical magnitude of the steady streaming generated by the changing section of the outer wall is small $O(0.01)$ compared to that generated by the catheter tip $O(0.1)$. We note that the slowly varying section of the outer wall amplifies the magnitude of the steady streaming near the catheter tip. We found that $|\mathbf{v_s}|$ increases with $\epsilon$ for all values of $\epsilon$ we tested. Some of this effect is probably related to higher leading order velocities near the catheter tip because the fluid is accelerated in a constricted annular gap. Based on a higher local velocity, the steady streaming at the catheter tip should scale with $r_{\text{H}}/(r_o(z = 0) - r_i)$. Such an explanation might however be too simple, as steady streaming is a non-linear boundary layer phenomenon. It does not explain for example why $\max(|\mathbf{v_s}|)$ is considerably larger for the larger $\epsilon$ (comparing figure 8.3(e) with 8.3(f)) even though the section of the annular gap at the catheter tip is similar. To better understand this phenomenon it would be

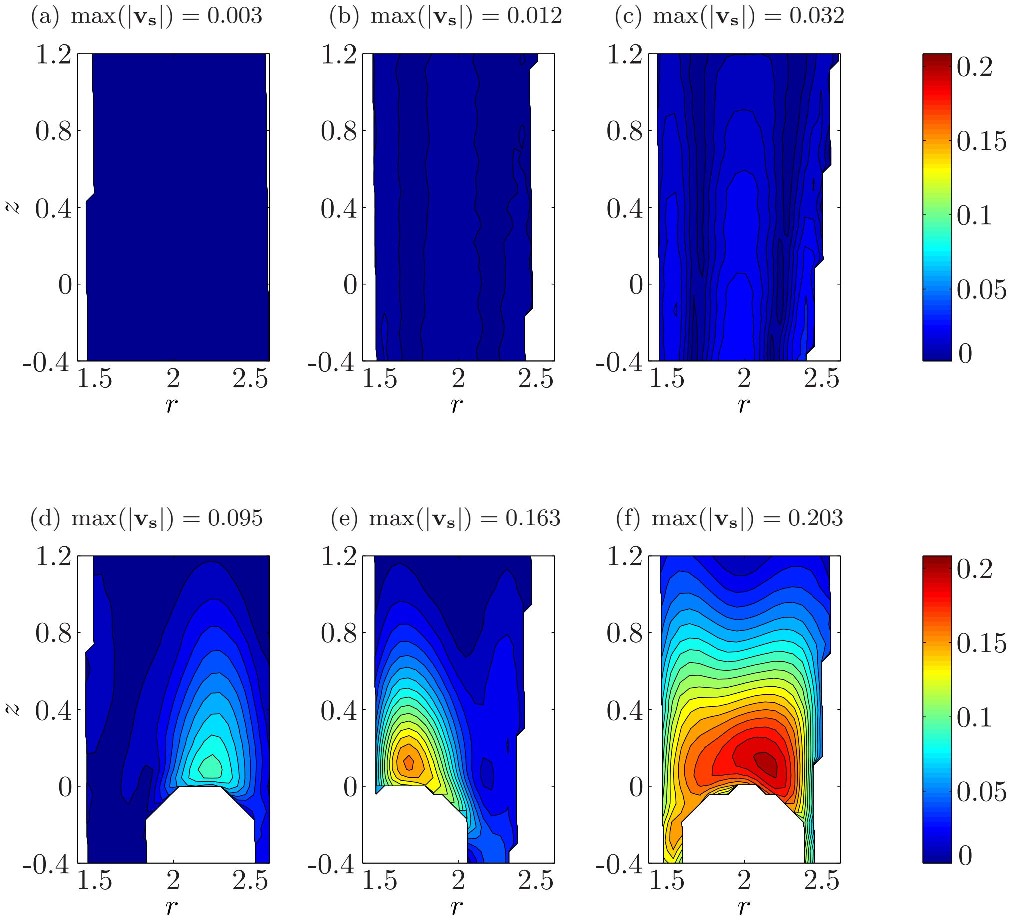

**Figure 8.3:** The magnitude $|\mathbf{v_s}|$ of the measured steady streaming without (a)-(c), and with (d)-(f) a catheter placed in a constant cross section annular gap (a), (d) or in an annular gap with a varying outer wall with $\epsilon = 0.019$ (b), (e), or 0.056 (c), (f). $|\mathbf{v_s}|$ is normalized with $\omega d_{\mathrm{osc}}$.

insightful to place the catheter near an expanding section, something that is difficult to do in our present setup. Unfortunately, our velocity profiles lack spatial resolution and accuracy in the boundary layer for a quantitative analysis of this phenomenon.

Figure 8.4 shows the axial velocity profile at the regions surrounding the catheter tip ($\theta \in \{-0.2, 0, 0.2\}$ to within experimental error). The steady streaming in the plane of the catheter is restricted to a small region above the catheter tip. The axial velocity is in the negative $z$-direction, towards the catheter tip. To the side of the catheter the steady streaming velocity is in the positive $z$-direction. This corresponds qualitatively to the upward steady streaming adjacent the catheter shown in figure 7.4(a). The shape of the recirculation pattern cannot be explained by the axi-symmetric steady streaming theory, but is adequately described with the numerical model. Intuitively, one can interpret the rounded catheter tip as a converging channel, but with the recirculation cells displaced. We can observe that the slope of the perturbation increases both the positive and negative axial steady streaming velocities.

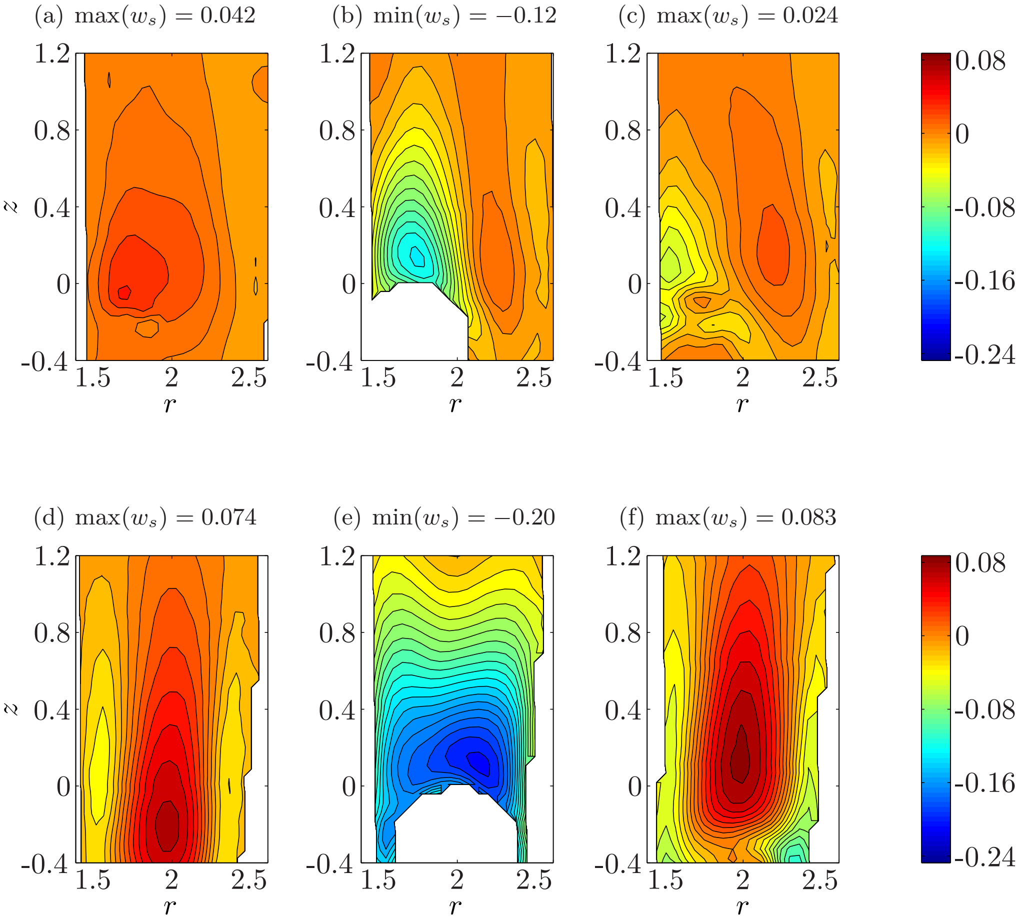

**Figure 8.4:** The normalized axial steady streaming around the catheter in a straight annular gap (a)-(c) and an annular gap where $\epsilon = 0.056$. The angle with respect to the mid-plane of the catheter is -0.26 rad (a), 0 rad (b), 0.19 rad (c), -0.23 rad (d), 0 rad (e), 0.17 rad (f). Slight variations in catheter position between the planes may exist.

## 8.4 Summary of the PIV study

In this chapter we have compared $|\mathbf{v}_{\mathrm{rms}}|$ and the mean axial component of the velocity field, i.e. $w_s$, with theory for several configurations of the experiment. The RMS measurements indicate that we have an error on time integrated quantities that is of the order of 5% outside of the boundary layers. Although our laser scanning setup was not originally designed for accurate PIV measurements, we were able to check the order of magnitude and trend of the steady streaming predicted by the axi-symmetric analytical model for several values of $\epsilon$. Furthermore, we showed that the numerically calculated steady streaming around the catheter tip is realistic, obtaining a similar maximum steady streaming velocity, direction, and a similar extent of the non-zero mean velocity. Finally, we have shown that the magnitude of the steady streaming is sensitive to variations in the cross section of the annular gap. Although this might be explained to some extent by an increase in leading order velocities, it is probably also due to a boundary layer phenomenon that is poorly understood at present.

# Chapter 9

# Conclusions

We have analyzed several sources of steady streaming using analytical, numerical and experimental techniques. The analytic model is valid for an annular gap with a slowly varying cross section defined by its slope $\epsilon \ll 1$, and an oscillatory flow field limited by $\epsilon \mathrm{Re} \ll 1$. The model predicts that at moderate $\alpha$, the midline velocity is in the direction of the wider end of the geometry. The non-dimensional steady streaming is dependent on the slope of the outer wall and $\alpha^2 A_{\mathrm{osc}}$. The steady streaming inside our annular gap corresponds qualitatively to the case of steady streaming inside a slowly varying channel, described by Grotberg. The functional dependence of steady streaming on $\epsilon$ was confirmed to within experimental error using PIV measurements in three 3 different geometries. We note that the order of magnitude of such steady streaming is $\sim O(1$ mm/s, roughly the same as the injection speed of the dye through an intrathecal catheter.

Steady streaming induced by the catheter tip was numerically investigated using a commercial code. We found significant steady streaming velocities centered on a point above the catheter tip, extending at least 5 mm in all directions. The steady streaming is characterized by a downwards velocity straight above the catheter tip with recirculation occurring on either side. The maximum magnitude of the effect is in the order of $0.1\ \omega d_{\mathrm{osc}}$ which is considerably higher than the typical velocities related to the steady streaming of the axi-symmetric perturbations.

We numerically explored the steady streaming inside a more realistic model of the subarachnoid space. We found that although the steady streaming becomes 3D, the azimuthal component is relatively weak, at most 25% of the in plane steady streaming. We observe that the analytical axi-symmetric model correctly predicts the order of magnitude and the direction of the steady streaming. Although slowly varying axi-symmetric cross sections might underestimate the local steady streaming velocities that can be found in the subarachnoid space, they should therefore provide an adequate experimental model.

Using PIV measurements we were able to successfully compare the steady streaming velocities around the catheter tip in the $(r, \theta = 0, z)$-plane with the aforementioned numerical results. Furthermore, using a slightly offset plane, we were able to confirm that the downward velocity in the catheter plane was compensated by an upward flow at either side of the catheter. We discovered that the magnitude of the steady streaming could be increased dramatically by putting the catheter near a slowly varying outer wall. Although we speculate that this phenomenon might be in part explained by the local increase of the velocity at the catheter inside a constricted geometry, we did not investigate this 3D boundary layer phenomenon in detail.

# Part II

# Mixing phenomena in ITDD

# Chapter 10

# Introduction

We have characterized the steady streaming in the previous part. Although the enhanced mixing theory is well established, it might not suffice to explain the 3D drug dispersion in ITDD. Furthermore, we do not know how the injection rate, enhanced mixing and steady streaming interact to determine the drug distribution in ITDD. Rather than attempting to explain each mechanism of dispersion independently, we have performed a large series of experiments to study the interaction of dispersing mechanisms as a function of the primary variables, the injection rate $Q_{\text{inj}}$, the non-dimensional amplitude of oscillation $A_{\text{osc}}$, the oscillation frequency $f_{\text{osc}}$, and the slope of the slowly varying cross section geometry $\epsilon$.

To achieve this we rely on our optical system to give us quantitative concentration data. This requires a detailed description of the errors related to our LIF, and our scanning setup in particular. Furthermore, for a study of the axial dispersion we must reduce the acquired cross sections of fluorescent dye concentration from quasi-3D to 1D. These issues are addressed in chapter 11. It also includes a review of quenching phenomena, beam scattering, optical aberrations as well as a complete calibration and evaluation of the error due to absorption of the laser beam. This evaluation is also aimed at identifying an optimum laser power ($P_0$) for a given concentration ($C$) of dye. Although the calibration measurements are based on homogeneous dye concentrations, our aim is to extrapolate them to the injection of a small bolus volume ($V_B$) of dye that disperses over time. We specifically hypothesize how the error due to attenuation of the laser beam influences the accuracy given an initial $V_B$ and initial $C$.

Following this analysis we present a LIF study aimed at understanding how steady streaming, enhanced diffusion, and the injection rate influence the advection of the dye in our experimental model (presented in chapter 3). It includes a wide variety of qualitative and quantitative observations, each characterizing a different aspect of the dye dispersion. For each observation, such as the decay of concentration in time, or the propagation of the dye envelope, we link experimental observations to parametric models of the given variables. Where possible we specifically address how the limited accuracy of measurement method is expected to quantitatively influence our observations.

Finally, the conclusions that can be drawn from this thesis are presented in chapter 13. We specifically address possible implications for clinical work and present an outlook on possible future work in this field.

# Chapter 11

# Quantitative LIF

## 11.1 Introduction

LIF is a diagnostic tool that is used to measure dye concentrations [40]. It is usually assumed that the fluorescent intensity $I_\mathrm{f}$ is linearly dependent on the concentration of the dye $C$ and the temperature $T$. Using a laser light sheet to illuminate the dye it is therefore relatively easy to obtain images that give a qualitative impression of the local concentration. In this chapter we evaluate the accuracy of LIF under the influence of optical distortions, quenching, scattering, and attenuation of the laser beam.

In section 11.2 we shortly discuss the experimental setup. Lens aberrations decrease the measured intensity in certain parts of the image, while the signal is also deformed through the cylindrical tubes and inhomogeneous scanning of the laser beam. These issues are discussed in section 11.3. Dye molecules are subject to (ir)reversible quenching, meaning that they do not always fluoresce at their optimum efficiency. Furthermore, the laser beam is scattered by the dye molecules, widening the beam and inducing secondary scattering. We address quenching and scattering in section 11.4. Finally, we find that the accuracy of our method is largely dependent on the attenuation of the laser beam which exponentially decreases the fluorescent signal with distance. The absorption and its effect on the measurement is analyzed in 11.5, together with the results of a calibration. Finally, we present two ways of artificially increasing the dynamic range of our camera in section 11.6.

## 11.2 Setup

To characterize the fluorescent signal we used the laser scanning system described in 4.2, composed of rotating mirrors, an 8-bit CMOS camera with a 12x zoom lens (f/# 2.4), and a high frequency pass color filter. The distilled water inside the cylindrical tubes is replaced by a solution with a known concentration of fluorescein. Unfortunately, it is not possible to perform the calibration at the level of the catheter tip ($z = 0$) because of the considerable attenuation of the laser beam inside the cylindrical tubes. We therefore measured in the slightly modified top part of the experimental setup, approximately 150 mm above the test section. The camera was mounted on a traverse parallel to the annular gap, ensuring that the distance of the camera to the cylindrical tubes did not change when performing experiments. The modified setup is shown in figure 11.1. The free surface coincides with the field of view of the camera, which is lower than is usual. This is required to place the mask into the path of the laser, and ensure that we can measure the entire beam once it enters the fluorescein concentration. These modifications have no significant influence on the quality of the laser beam. Because it is difficult to center the inner tube in the

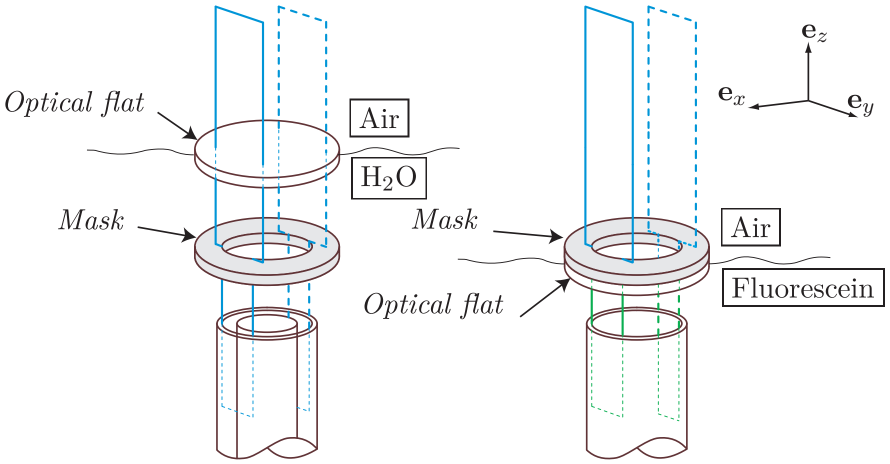

(a) (b)

**Figure 11.1:** (a) the standard optical layout used for experiments, and (b) the modified setup used for the calibration experiments.

modified setup, we performed the calibration measurements without the inner cylinder. We discuss the implications of this in section 11.3.2.

The measurements presented in this chapter were performed with concentrations of fluorescein that were diluted from an initial stock of 1g of fluorescein per 1 liter of distilled water. Several stocks were made to make sure no dilution errors were made. Stocks were not kept for longer than a few days and stored in a closed cupboard to minimize the risk of bleaching through daylight. In anticipation of the results of section 11.4.2 that addresses the effect of bleaching of the dye under high laser power $P_0$, we normally limit $P_0$ to 500 mW.

## 11.3 Corrections for Image Distortions

In this section we discuss how we compensate measured concentrations for the effects of lens aberrations, optical distortions and the scan speed $\dot{\xi}$ ($\mathbf{e}_y$).

### 11.3.1 Lens Aberrations

Depending on the degree of zoom, lens aberrations have to be accounted for. Although a small image distortion is evident at high zoom, the effect of reduced intensity away from the center of the image is far more important. These aberrations can be modeled using a commonly used Zernike model which consists of a series of polynomials:

$$\begin{aligned} Z_n^l &= R_n^l(r)\cos(l\theta_{\text{im}}) \\ Z_n^l &= R_n^{-l}(r_{\text{im}})\sin(n\theta_{\text{im}}) \end{aligned} \tag{11.1}$$

where $r_{\text{im}}$ and $\theta_{\text{im}}$ are the normalized polar coordinates with respect to the center of the image ($\mathbf{e}_x$) and $l$ and $n$ are natural numbers. Each polynomial $R_n^l$ corrects for a different aberration such as tilt, defocus, astigmatism, coma, etc.. Zoom decreases the measured

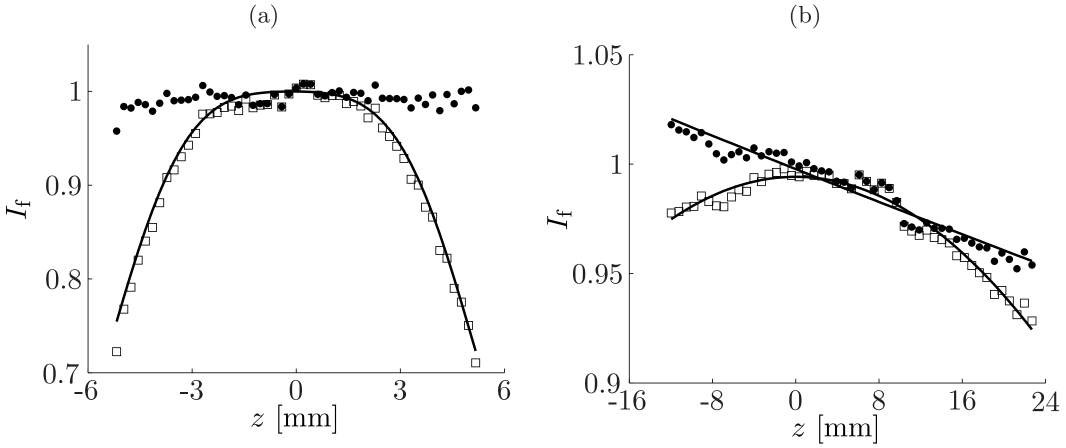

**Figure 11.2:** The normalized intensity on the centerline ($\mathbf{e}_z$) of an image before $I_f$ (□), and after $I_{corr}$ (●) correction with the Zernike model. (a) corresponds to a zoomed in image, and (b) is representative of a zoomed out image, used during most experiments. The latter includes a fit $I_f(z) = A e^{-az}$ on the corrected centerline that captures the attenuation of the laser beam due to absorption even at the low concentration of 0.0625 mg/l.

intensity at the edges of the image. Therefore we included terms for parabolic defocusing, as well as for primary and secondary spherical aberrations, to correct for this behavior. The optimal number of correctional terms was determined by trial and error. The Zernike model was reduced to:

$$Z(r_{im}) = a_0 + a_1(2r_{im}^2 - 1) + a_2(6r_{im}^4 - 6r_{im}^2 + 1) + a_3(20r_{im}^6 - 30r_{im}^4 + 12r_{im}^2 - 1) \quad (11.2)$$

To calculate the constants, calibration images were taken at different zoom positions of a homogeneous concentration of fluorescein illuminated with the laser scanning setup without the glass cylinders. The concentration used was highly diluted (0.0625 mg/l) to reduce the effect of laser beam attenuation. To obtain sufficient signal in the calibration images, the laser power was 1 W and the scan speed was lowered as compared to normal experimental conditions. The calibration images are fitted with the Zernike polynomial and the model constants are determined. A corrected image ($I_{corr}$) is then calculated by dividing the original image ($I_f$) by the Zernike model:

$$I_{corr}(r_{im}, \theta_{im}) = \frac{I_f(r_{im}, \theta_{im})}{Z(r_{im})} \quad (11.3)$$

The effect of this correction on the calibration images is shown in figure 11.2. A zoomed out image as characterized by 11.2(b) can typically be described to within ± 3% accuracy using only $a_0$ and $a_1$. The incorporation of the other model constants does not improve the fit. A zoomed in image such as characterized by the centerline shown in figure 11.2(a) requires all the Zernike model constants in equation 11.2 to obtain a similar accuracy. In table 11.1 we give the normalized model constants and their 95% confidence interval for the correction shown in figure 11.2(a).

| $a_i$ | Value | 95% conf. [%] |
|---|---|---|
| $a_0$ | 1 | 0.01 |
| $a_1$ | -0.29 | 0.07 |
| $a_2$ | 0.02 | 1.3 |
| $a_3$ | 0.05 | 0.4 |

**Table 11.1:** Zernike model coefficients, including a 95% confidence interval.

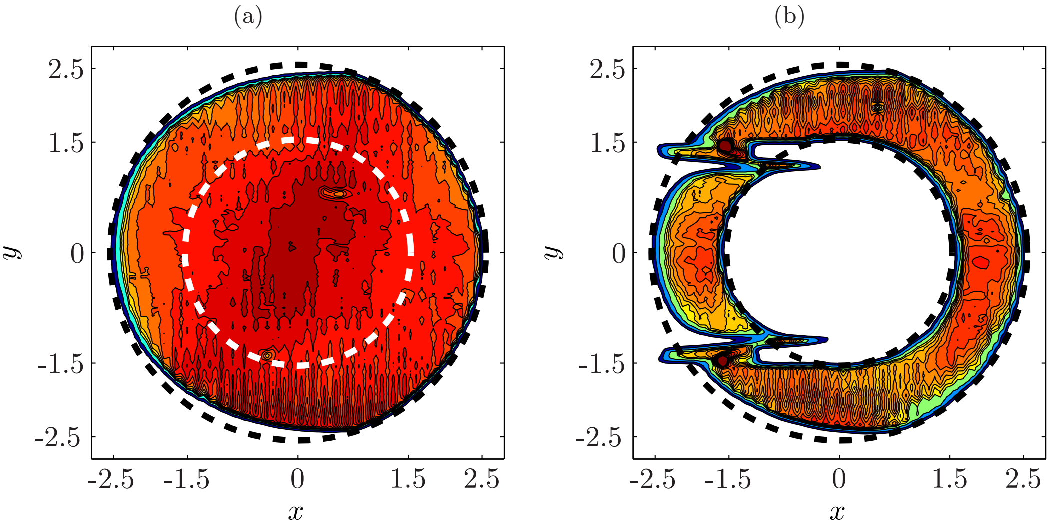

**Figure 11.3:** A contour plot of a transverse cut through a full 3D scan consisting of 71 image planes. (a) Shows a scan of a typical calibration measurement, while (b) an identical scan with the inner tube in place. The white line roughly indicates the position of the glass tubes.

### 11.3.2 Image Distortions

As previously mentioned, it is not practical to perform the calibration measurements inside the experiment with the inner tube. We determine the influence of the inner tube by comparing a 71 plane 3D scan of the entire annular gap with the same scan inside only the outer tube. The result is shown in figure 11.3. It is immediately evident that the spatial intensity profile behind the inner tube is altered. There are however no vertical ($\perp$ to the plane shown in figure 11.3) optical distortions. The problem is twofold, first the voxel volume (a small imaginary volume within the beam width that is projected onto the image plane) changes as a function of $x$ and $y$, and second, a reconstruction of the image is not straightforward. Although this has consequences for the measurements, this does not influence the calibration measurements. It can be observed in figure 11.4(a) that there is no noticeable difference between the intensity measured at similar locations in front of, or behind the inner glass tube. From the two intensity profiles across the image planes shown in figure 11.4 it is evident that $I_\mathrm{f} = I_\mathrm{f}(x)$. The maximum at $x = 0$ and $y = 0$ is characteristic of a focusing error in the images. This would normally require the identification of a specific Zernike polynomial for each plane, but this is not deemed necessary because the variations in the annular gap are within the error margin. The

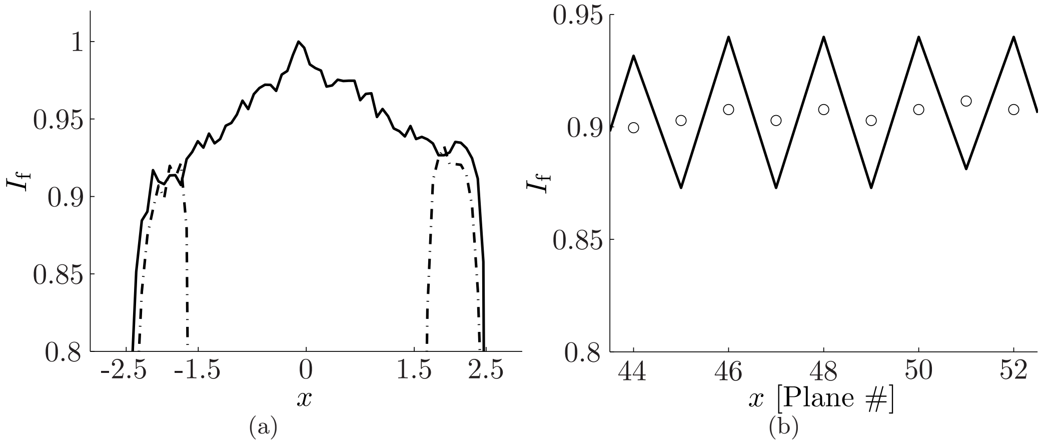

**Figure 11.4:** The intensity profile normalized to $I_\mathrm{f}(x=0, y=0, z=\mathrm{Cst})$ across the image planes ($\mathbf{e}_x$), specifically (a) $I_\mathrm{f}(x, y=0, z=\mathrm{Cst})$ vs. $x$, and (b) $I_\mathrm{f}(x, y=2, z=\mathrm{Cst})$ vs. plane number. $I_\mathrm{f}$ was measured inside a homogeneous concentration inside a geometry without (solid line) and with the inner glass tube (dashed line). The peak in (a) is characteristic of a focusing error, while the zigzag in (b) is due to scanner acceleration. The ($\circ$) shows the result of using equation 11.4 to correct this phenomenon.

ragged profile at $x = 0$ and $y = 2$ is due to differences in scan speed, and is addressed in the next section.

### 11.3.3 Scanner Speed $\dot{\xi}$

The rotating mirror making the light sheet accelerates during the scan, and the fluorescent intensity $I_\mathrm{f}$ will be higher where the scan speed $\dot{\xi}$ is lower. This depends on the scan direction. Because we generally scan back and forth this means that the measured intensities are different for consecutive planes, even though the concentration is constant. The difference between the measured intensity for a homogenous concentration of dye at the same position can vary by as much as 8%. This is illustrated in figure 11.4(b) which is based on the homogenous transverse cut of the laser intensity shown in figure 11.3(a). Although the acceleration characteristics are reproducible, they cannot be eliminated when working with small scanning angles at high scanning speed $\dot{\xi}$.

One could perform a double scan for each plane, but this poses other risks related to the stability of the fluorescent dye as will become evident in section 11.4. It is therefore more appropriate to compensate for this effect post acquisition by a correctional multiplication of the measured intensity. We scan a homogenous concentration of dye (without the inner tube) and calculate the intensity between two planes using a linear interpolation, or $I_{\mathrm{f},n+1/2} = 1/2(I_{\mathrm{f},n} + I_{\mathrm{f},n+1})\ \forall n \in [1, N_\mathrm{nop} - 1]$, where $N_\mathrm{nop}$ is the number of planes scanned for the cross section. We use $I_{\mathrm{f},n+1/2}$ to normalize each scanned plane $I_{\mathrm{f},n}$ and define the error due to scan speed $\varepsilon_\xi = I_{\mathrm{f},n} - I_{\mathrm{f},n+1/2}$. We combine the $\varepsilon_\xi$ for all the even planes (or odd) and find that the resulting set is a function of $y$ only. The measured intensity is subject to random electronic noise from the camera that is of the order ± 1%, and we therefore fit a polynomial of order 3 ($f_\xi$) to describe the required correction. Including

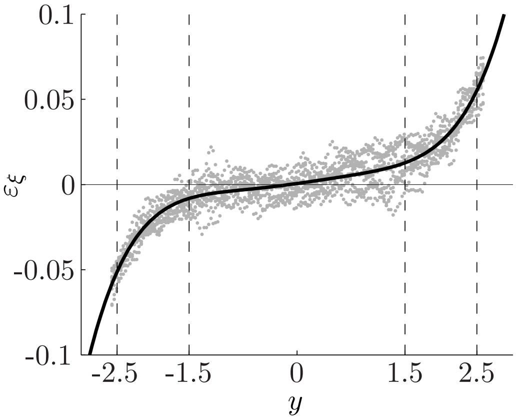

**Figure 11.5:** The error due to rotating mirror acceleration $\varepsilon_\xi$ vs. y for a plane that was scanned from right to left. The fit $f_\xi$ is a polynomial of order 3. The dashed lines indicate where the annular gap would usually be.

the Zernike polynomial from the previous section, we find:

$$I_{\text{corr}} = \frac{I_{\text{f}}(r_{\text{im}}, \theta_{\text{im}})}{f_\xi(y) Z(r_{\text{im}})} \tag{11.4}$$

$f_\xi(y)$ is shown in figure 11.5. As can be expected, we find that the error due to the mirror acceleration is largest near the outer wall, the region of the annular gap. This error could be reduced if we were to scan the laser over a distance $\gg 15$ mm, but this would unacceptably lower the acquisition rate. The result of a correction is shown in figure 11.4(b). Equation 11.4 is used to correct all LIF images unless stated otherwise.

## 11.4 Complex LIF Behavior

Quenching is a generic term used to describe the reduction of fluorescence intensity due to a loss of excitation energy. Quenching is often categorized by the mechanism through which this occurs. We discuss two types of quenching, reversible collisional quenching, and irreversible static quenching, more commonly known as photo-bleaching. Following this discussion we address issues pertaining to the scattering of the laser beam.

### 11.4.1 Collisional Quenching

Collisional or dynamic quenching is either caused by intermolecular collisions creating heat energy instead of light energy, or a reaction with a non-fluorescing quencher. This is a reversible process that is dependent on temperature and, if present, a quencher concentration $C_q$. It can be described using the Stern–Volmer equation:

$$\frac{I_{\text{f}}^0}{I_{\text{f}}} \propto (1 + k_q T) \tag{11.5}$$

where $I_{\text{f}}^0$ is the unquenched fluorescent intensity, $k_q$ is a quencher rate coefficient dependent on the time a fluorophore is in the excited state and the concentration of a quencher, and

$T$ is the temperature. The requirement to work at $T = 37$ °C will therefore slightly reduce the fluorescent intensity with respect to room temperature.

An experiment was performed where the temperature of the water bath was varied between 22 and 42°C for two different concentrations of dye (0.5 and 8.0 mg/l). The dye was excited using the experimental set of laser scanning parameters during roughly 8 seconds at a typical duty cycle of 38%. The laser powers $P_0$ used are close to, or higher than used during the calibration experiments. It was observed that the measured intensity for the whole image was decreased, independent of laser attenuation. The average pixel value of each image $\langle I_\mathrm{f} \rangle$ was calculated and used to determine the efficiency (the slope of equation 11.5, $k_q$) of the fluorescein. It was estimated from these experiments that the loss of signal due to collisional quenching was roughly 0.2%/°C, independent of $P_0$ and $C$.

### 11.4.2 Static Quenching

Static quenching is an irreversible and inevitable process where a fluorophore is destroyed due to photon induced chemical damage. This phenomenon is also known as photo-bleaching. The laser power determines the rate at which the fluorophore is destroyed, see for example [61]. The effect of photo bleaching on PLIF has been investigated by Larsen and Crimaldi [41] who have constructed a model that depends non-linearly on a photo-bleaching parameter $B$:

$$B = K \frac{P_0}{\dot{\xi} d_\mathrm{plane}} \tag{11.6}$$

where $d_\mathrm{plane}$ is the beam diameter, and $K$ a constant that depends on the scattering cross section of the dye, the number dye molecules bleached per photon, Planck's constant and the frequency of the incident light. For fluorescein excited at a wavelength of $\lambda = 488$ nm, $K = 1.37 \cdot 10^{-6}\ \mathrm{m}^2\mathrm{J}^{-1}$. To have a fluorescent signal $I_\mathrm{f}$ within 1% of the unquenched value $I_\mathrm{f}^0$, $B \leqslant 1.4 \cdot 10^{-2}$. At $B = 1$, roughly 50% of the signal is lost. Given typical scanning parameters ($P_0 = 520$ mW, $\dot{\xi} = 20$ m/s, and $d_\mathrm{plane} = 0.4$ mm (see next section for details)), we obtain $B = 8.6 \cdot 10^{-5}$, implying that we would be able to scan a molecule $\approx 160$ times.

To confirm this, we isolate the effect of static quenching in the images discussed in the previous section, by studying the average image intensity $\langle I_\mathrm{f}(t) \rangle$ normalized to its initial value $\langle I_\mathrm{f}(t = 0) \rangle$. The results for the first 2 seconds of the experiment are shown in figure 11.6. The average intensity is seen to decrease quickly before it tends to stabilize. We hypothesize that the bleached dye is replaced by convection brought about temperature gradients induced by collisional quenching. It can be observed that the stabilization is quicker for high $C$.

To describe only the rate at which dye is destroyed due to photo-bleaching, we look at the initial slope of the curves shown in figure 11.6. The slopes of the curves are summarized in table 11.2. We require that the total loss of fluorescent signal should not exceed 1% during an experiment. Using $P_0 = 520$ mW, a value often cited as the maximum permissible $P_0$, and a typical scan time of approximately 1 ms, the total number of scans should not exceed 200, a slightly larger value than theory. These estimates do not take into account the distance between image planes in a 3D scan. A low density 3D scan will not illuminate each dye molecule at each pass, while the same molecule could be illuminated several times in a high density scan.

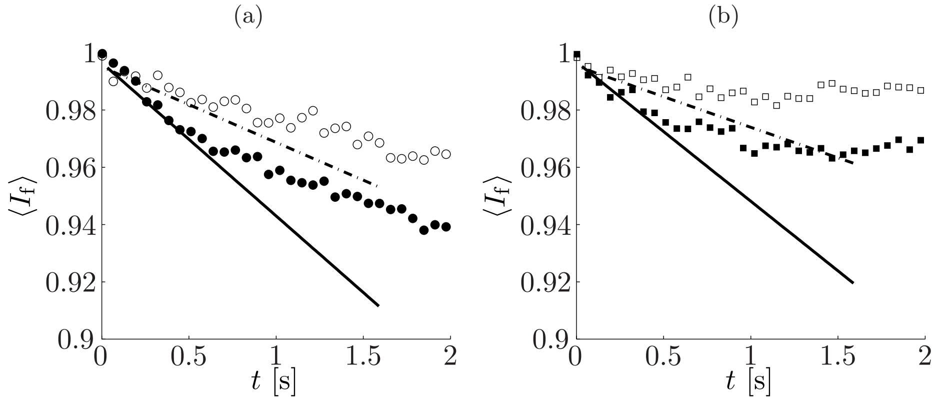

**Figure 11.6:** The effect of static quenching or photo-bleaching on the mean fluorescent intensity in the image $\langle I_\mathrm{f} \rangle$ normalized to $\langle I_\mathrm{f} \rangle(t = 0)$ vs. $t$ for different concentrations $C$ and laser power $P_0$ at $T = 37°$C. Typical laser scan speeds were used. Figure (a) shows the effect at $C = 0.5$ mg/l for $P_0 = 520$ mW (○), and $P_0 = 870$ mW (●), while the time evolution in (b) was measured at 8.0 mg/l for $P_0 = 59$ (□), and $P_0 = 100$ mW (■). The (dashed) straight lines are a linear least square fits to the data points and indicate the rate at which the fluorescein is destroyed.

| | $C = 0.5$ mg/l | $C = 8.0$ mg/l |
|---|---|---|
| $P_\mathrm{typ}$ | -0.03 | -0.02 |
| $P_\mathrm{high}$ | -0.05 | -0.05 |

**Table 11.2:** The rate at which dye is destroyed [s$^{-1}$] at a duty cycle of 38%. $P_\mathrm{typ}$ and $P_\mathrm{high}$ refer to a typical ($P_0 = 59$, or $P_0 = 520$ mW), or high ($P_0 = 100$, or $P_0 = 870$ mW) laser power for the given $C$.

### 11.4.3 Laser Beam Scattering

Light propagation in an absorbing and scattering medium can be described using the radiative transport equation (RTE):

$$(\Omega \cdot \nabla) I(r, \Omega) = -(a+s) I(r, \Omega) + \frac{s}{4\pi} \int_{4\pi} I(r, \Omega') \mathrm{d}\Omega' \tag{11.7}$$

where $I(r, \Omega)$ is the radiation intensity at position $(r, \Omega)$, where $\Omega$ is a solid angle, $a$ is the absorption coefficient, and $s$ is the scattering coefficient. In this expression of the RTE, we have neglected unsteady effects and do not consider any source terms. The spatial dependence of $I(r, \Omega)$ is dependent of the scattering of the light. Dye molecules are small compared to the wavelength ($\lambda = 488$ nm), so the scattering from a laser beam can be described using the Rayleigh approximation:

$$I(\theta) \propto N_s (1 + \cos^2(\theta)) \tag{11.8}$$

where $N_s$ is the number of scatterers, and $\theta$ is the angle of the scattering with respect to the incident light. This symmetrical relation implies that the backward scattering is equal to the forward scattering but implies that the laser beam will also diffuse radially. Because backscattering is important, the fluorescent signal at $z = h$ also depends on the laser power at $z = h + \Delta h$. Since Rayleigh scattering depends on the number of scatterers in the solution $N_s$, the laser beam signature across a steep concentration gradient will change. In the absence of scattering, i.e. $s = 0$, the solution of the RTE (equation 11.7), known as the Lambert–Beer law of exponential decay, is easily found:

$$I_{\mathrm{f}}(z) = I_{\mathrm{f}}(0) \mathrm{e}^{-az} \tag{11.9}$$

For this result, we have assumed that all the absorbed energy has been emitted as light, and that the measured $I_{\mathrm{f}}$ is a constant fraction of the emitted light. The influence of scattering on our calibration has been qualitatively studied by zooming in on the region where the laser beam enters the dye, just below the optical flat. $P_0$ was low, and scanned during several milliseconds. Several measured beam profiles $I_{\mathrm{f}}(y, z = \mathrm{Cst})$ are shown in figure 11.7. We observe that the cross section of the beam grows with $z$ even though the concentration is homogenous. This diffusion of the laser beam cannot be explained by absorption, unlike the reduction of the signal after the beam has reached its final width.

To isolate the effect of scattering from absorption, each profile was normalized by its maximum value and the standard deviation $\sigma(z)$ was calculated. This is taken as an absolute measure of beam width, and indicates the effect of scattering in the cross sectional direction. The result as a function of distance is shown in figure 11.8. This indicates that the standard deviation reaches a steady state. This seems to imply that the scattering is still important, but no longer changes the beam signature. Although scattering partly determines the changing amplitude of fluorescent signal, the Lambert–Beer law can still be used to approximately calculate the absorption coefficient. However the measured absorption coefficient ($a_m$) will include the effect of scattering.

Figure 11.9 shows that the beam width, and thereby the effect of the scattering of the profile, depends slightly on both the concentration $C$ and the laser power $P_0$. To avoid over-sampling the dye during a 3D scan and thereby increasing the effect of static quenching, a minimum distance of $d_{\text{plane}} = 0.4$ mm is used to separate the light sheets.

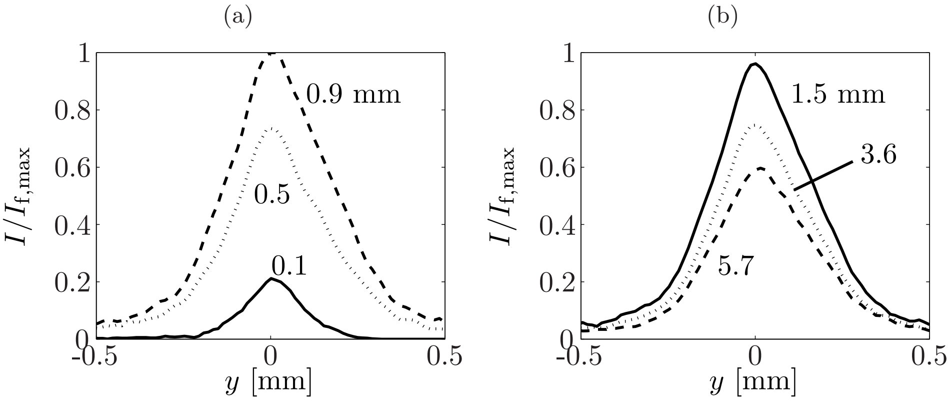

**Figure 11.7:** The signature, or transverse intensity profile ($\mathbf{e}_y$) of a stationary laser beam ($P_0 = 66$ mW) as it enters a homogeneous solution of fluorescein ($C = 8.0$ mg/l). The number next to the graph indicates the distance ($\mathbf{e}_z$, [mm]) traversed in the solution. Notice how the profile first grows both in width and amplitude (a) and subsequently diminishes with increasing distance (b).

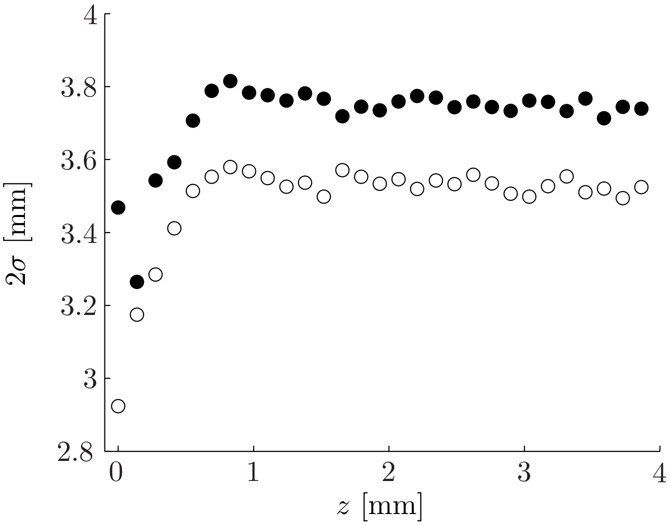

**Figure 11.8:** The standard deviation ($\sigma$) of the normalized beam signature vs. $z$ for a dye concentration of $C = 0.5$ mg/l and $P_0 = 800$ mW (●), and $C = 8.0$ mg/l and $P_0 = 66$ mW (○). The leveling of the standard deviation after an entrance length of roughly 1 mm indicates that the influence of beam scattering on the beam signature has reached a steady state.

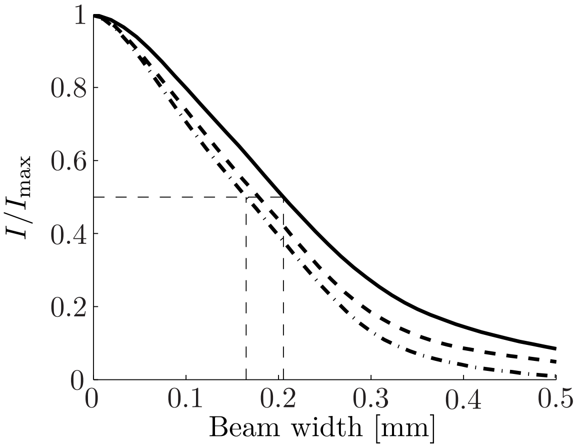

**Figure 11.9:** The normalized intensity profile at $z = 3.2$ mm for laser power $P_0 = 800$ mW and $C = 0.5$ mg/l (solid line), $P_0 = 24$ mW and $C = 8.0$ mg/l (dash–dotted line), and $P_0 = 66$ mW and $C = 8.0$ mg/l (dashed line). Based on a 50% threshold, the beam width is between 0.33 and 0.41 mm.

## 11.5 Calibration Measurements

### 11.5.1 Procedure

The fluorescent response of a wide range of concentrations ($C = 0.0625$ to 24 mg/l) to a wide range of laser intensities ($P_0 = 24$ to 800 mW) using standard experimental scanning parameters (scan time = 0.96 ms) was imaged using the 8-bit CMOS high speed camera. Constructive background noise is related to specific electronic CMOS noise and can be characterized statistically with an average intensity $\langle I_{\mathrm{BG}} \rangle = 9.8$ pixel levels, and a standard deviation $\sigma_{\mathrm{BG}} = 3.7$ pixel levels. We subtract the structured noise by hardware upon acquisition. Ten 3D scans were averaged to filter random electronic noise (of the order of ±1%, see figure 11.5). No zoom was used, and the image was focused on the outside wall of the outer glass cylinder. Because the distance of the camera to the glass tubes is fixed, it is possible to reestablish the exact camera settings when required.

The resulting image planes were corrected with equation 11.4. Regions away from the walls are distorted and influenced by to the limited resolution of our system and not included in the analysis. The remaining data was integrated over $x$ and $y$ to yield $I_{\mathrm{f}}(z)$, where $z$ is the optical axis. The response of a certain dye concentration to laser power was defined as the maximum of the intensity trace ($I_{\mathrm{f,max}}$). Finally, we fit Lambert–Beer law to $I_{\mathrm{f}}(z > z_{\mathrm{ent}})$ by taking into account the background subtraction.

### 11.5.2 Amplitude Dependence

At constant laser intensity $I_{\mathrm{f,max}}$ varies linearly with concentration $C$. This is illustrated with several examples in figure 11.10. We determined the slope for each laser power $P_0$ by fitting a first order polynomial ($I_{\mathrm{f,max}} = p_1 C + p_2$, $p_2 \leqslant 0$). A negative intercept ($p_2$) is a direct result of the background subtraction. Positive intercepts are related to noise and are not taken into consideration. The calibration constant $p_1$ is linearly dependent on the laser power $P_0$ as is shown in figure 11.10(b). This relationship is convenient experimentally because the optimal laser power $P_0$ can be set as a function of dye concentration without a new calibration.

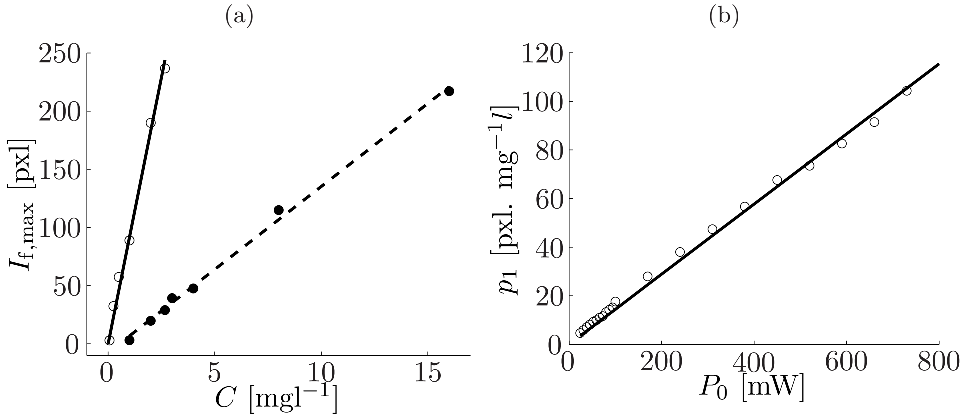

**Figure 11.10:** (a) two representative calibration curves of $I_{\mathrm{f,max}}$ for $P_0 = 87$ mW (solid line), and $P_0 = 660$ mW (dashed line), and (b) the linear relationship between the calibration slopes and the $P_0$.

### 11.5.3 Absorption

The limited sensitivity of our system requires us to work with relatively high concentrations. Unfortunately, at high concentrations the attenuation of the laser beam due to absorption becomes significant. We investigate the attenuation of the laser beam to estimate the error induced by neglecting it. As explained in section 11.4.3 we fit the Lambert–Beer law on $z > z_{\mathrm{ent}}$, and correct for the background subtraction of the images:

$$I_{\mathrm{f}} = A\mathrm{e}^{-a_m z} - \langle I_{\mathrm{BG}}\rangle(z) \tag{11.10}$$

where $\langle I_{\mathrm{BG}}\rangle(z)$ is the average value of the background image at each $z$. As shown in figure 11.11(a), $a_m$ varies linearly with $C$, and is independent of $P_0$.

### 11.5.4 Error Analysis

First we note the important detection threshold of $9.8/2^8 = 3.8\%$ imposed by the background subtraction of the electronic noise. This is more than is usual for 3D dispersion problems, for which the benchmark is a 12-bit CCD camera characterized by a detection threshold of $1/2^{12} = 0.02\%$. However, by far the most important measurement error of $I_{\mathrm{f}}(z)$ is the attenuation due to absorption. In the remainder of this section we attempt to estimate this error based on the typical distance ($h_{\mathrm{typ}}$) the laser beam needs to traverse, defined as:

$$h_{\mathrm{typ}} = \frac{V_{\mathrm{dye}}(t)}{F\pi(r_o^2 - r_i^2)} \tag{11.11}$$

where $F$ represents the fraction of the annular gap that is occupied by the dye solution, and $V_{\mathrm{dye}}$ is the volume of dispersion. We investigate the effect of diluting an initial volume of dye. If we assume a homogenous concentration $C = C(t)$, a typical absorption coefficient

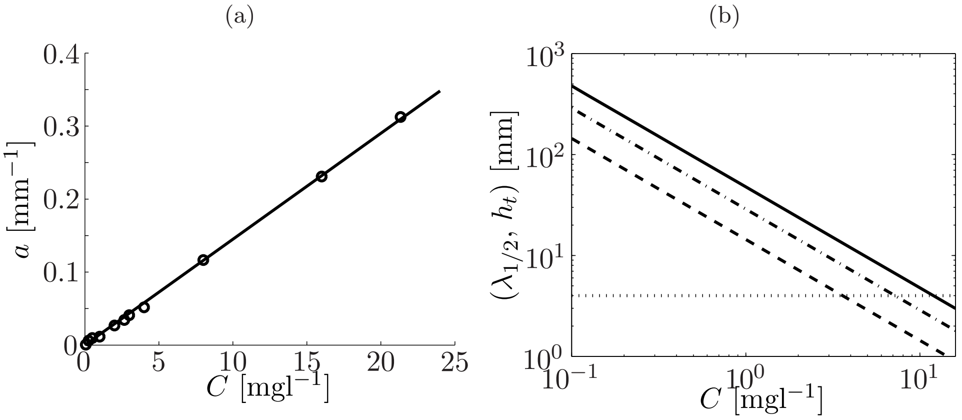

**Figure 11.11:** (a) The attenuation coefficient $a$ vs. $C$, and (b) the distance $\lambda_{1/2}$ (solid line), and $h_{\rm typ}$ for an initial volume $V_B = 50$ $\mu$l and $C_0 = 16$ mg/l that spreads homogeneously to fill half the annular gap (dash/dotted line), or the entire annular gap (dashed line). The $\lambda_{1/2}$ inside an undiluted solution of the same $C_0$ is also indicated (dotted line).

($a_{\rm typ}$) is characterized by the amount the dye that has been diluted with respect to its initial concentration:

$$a_{\rm typ} = K_{\rm abs}C(t) = K_{\rm abs}\frac{C(0)V_{\rm dye}(0)}{V_{\rm dye}(t)} \tag{11.12}$$

$K_{\rm abs}$ is the slope of the linear relation between the absorption coefficient and concentration shown in figure 11.11(a). We define $\lambda_{1/2}$ as the distance at which $I_{\rm f}(z = \lambda_{1/2}) = I_{\rm f}(z = 0)/2$, which we calculate with $\lambda_{1/2} = -1/a\ln(1/2)$. We compare $\lambda_{1/2}$ with $h_{\rm typ}$ in figure 11.11(b) for an initial volume of 50 $\mu$l and concentration of 16 mg/l for a fill factor $F$ of 1/2 and 1. Although $h_{\rm typ}$ always lies beneath $\lambda_{1/2}$ they are comparable in magnitude. We can examine the influence of absorption on the amount of dye ($m$) that can be measured in the laser path:

$$m = A\int_0^{h_{\rm typ}} {\rm e}^{-a_{\rm typ}z}{\rm d}z \tag{11.13}$$

The relative error induced by the attenuation of the laser beam can therefore be calculated using:

$$\varepsilon_a = \frac{m_{\rm r} - m}{m_{\rm r}} = 1 - \frac{1}{a_{\rm typ}h_{\rm typ}}\left(1 - {\rm e}^{-a_{\rm typ}h_{\rm typ}}\right) \tag{11.14}$$

where $m_{\rm r} = h_{\rm typ}A$ is the actual amount of dye in the path. If we take into an account an initial volume of 50 $\mu$l, and an initial concentration of 16 mg/l the error is approximately 35%. The error is 9% (18%) is the annular gap is (half) filled. The error therefore depends on the azimuthal spread of the dye. Several authors have used an iterative pixel correction based on the Lambert–Beer law to compensate the measured signal for high absorption, see for example Hertz and Alden [35] for a 1D and Abu-Gharbieh et al. [1] for a 2D application. Unfortunately, this is not easily implemented in this study because:

- During the injection of the bolus the dye will leave the field of view of the camera. We therefore do not know the initial laser power $P_0$ at the top of the image, a value required for an iterative correction procedure.

- The 3D dispersion quickly dilutes the dye, so that any correction is dependent on small relatively noisy values, limiting the accuracy of the method.

Versluis et al. [75] presented an experimental method that compensates for laser beam attenuation by separately scanning in opposite directions. Unfortunately, this doubles the time and data generation for a 3D scan. More importantly a bi-directional scan is not compatible with our chosen scanning direction.

## 11.6 Increasing Dynamic Range

We employ two methods to artificially increase the dynamic range of our system. First, planes near the catheter are scanned twice in rapid succession at a higher scan speed $\dot{\xi}$. This is equivalent to scanning at higher $P_0$. The image at high scan speed is only used to resolve regions of high concentration that saturate on the lower scan speed image. The lower $\dot{\xi}$ image ensures an optimal detection of low concentrations. Using this method we were able to effectively roughly add one bit to our dynamic range.

Second, we can increase the laser power $P_0$ during an experiment. We do this by taking away a neutral density filter from the optical path. Low concentrations are better resolved at the expense of changing the signal to noise ratio during the experiment. Concentrations that fall below the detection threshold at lower $P_0$ can be detected at higher $P_0$. Because we measure dye previously undetected, we have a discontinuity in the total measured mass $m$ and also measure a different dispersion. Although insightful and used throughout the experiments reported on in the next chapter, the jump in overall signal complicates the calculation of time derivatives. Furthermore, one can only compare experimental values of concentration if the laser powers are the same. Although useful, these methods to increase the dynamic range are no ideal substitute for a higher dynamic range camera.

## 11.7 Summary

We conclude that quantitative LIF with our system can lead to considerable errors, some of which we can correct. For example we systematically correct the raw images for lens aberrations and scan speeds. Furthermore photo-bleaching will decrease the fluorescein efficiency during an experiment and we must therefore limit the total scanning time per experiment to below 200 3D scans for $P_0 \leqslant 520$ mW. The scattering of the laser beam in the solution decreases the overall resolution of the system and makes it impossible to measure steep concentration gradients. For typical concentrations the laser plane thickness is estimated to be $\sim 0.4$ mm, giving us a good measure for determining the optimal number of planes (37) in a 3D scan covering the entire annular gap.

The background subtraction required to eliminate electronic noise implies a detection threshold of roughly 4% of the total 8-bit range. Of course if the initial concentration is slightly lower than 256 pixel values to avoid saturation, the relative detection threshold is higher. Although both the fluorescent signal and the absorption coefficient of fluorescein depend linearly on concentration, accurately measuring concentration using LIF remains a challenging problem. We scan 7 planes near the catheter at double the scan speed to artificially increase the dynamic range.

We underestimate the total amount of dye in the system by as much as 35%. The relative error $\varepsilon_a$ is dependent on the amount of azimuthal spread. Accurate compensation is not deemed feasible with our limited field of view, relatively noisy measurements and experimental design. Finally, given the sensitivity of our camera, the maximum $P_0$, and our desired scan speed, we have determined that the optimal initial concentration for a dispersion experiment is 16 mg/l.

# Chapter 12

# Experimental Investigation of Mixing in ITDD

## 12.1 Introduction

In the previous chapter we have analyzed the optimal way fluorescein can be used in our high frequency laser scanning setup. In this chapter we experimentally investigate the dispersion of the dye for a large number of experimental parameters: the injection catheter and orientation $\varphi$, the amplitude $A_{\text{osc}}$ and frequency $f_{\text{osc}}$ of oscillation, the injection speed $Q_{\text{inj}}$, a slowly varying cross section characterized by its slope $\epsilon$, and finally buoyancy.

The setup and scanning system is the same as used to characterize the steady streaming and the reader is referred to section 4 for a detailed description. We discuss the procedure and the parameters used during the experiments in section 12.2. Throughout this chapter we identify specific system responses that characterize the dispersion process. In section 12.3 we show the method by which we create parametric models based on these responses. In this section we also describe the justification of reducing the planar concentration measurements we obtain with our optical system to $(\theta, z)$-projections, i.e. the radial integration of the data, the mean axial profile $\bar{C}(z,t)$, and finally the total measured mass inside our volume of observation ($m_{\text{CV}}(t)$).

The remainder of this chapter is organized roughly in term of the dimensionality of the data we characterize. In section 12.4 we first use $(\theta, z)$-projections of the measurements to qualify the dispersion inside the straight annular gap, in particular the direction of spread. In section 12.5 we discuss the dispersion in the $(\theta, z)$-projections by analyzing the state of mixing using a newly defined parameter. In section 12.6 we primarily use single plane concentration measurements to qualitatively describe the combined influence of the catheter and a slowly varying cross section annular gap on the dispersion of the dye. We study the mean axial concentration in time $\bar{C}(z,t)$ in section 12.7. We focus on the influence of $\epsilon$, but also attempt to use the 1D enhanced diffusion model discussed in section 3.4 to compute an enhanced diffusion coefficient in the constant cross section geometry. Finally, in section 12.9 we look at how $m_{\text{CV}}(t)$ is primarily influenced by the injection and oscillation parameters. We also study several parametric models of characteristic features of $m_{\text{CV}}$ that give us more insight in the interactions between these parameters. Finally, in section 12.10 we qualitatively investigate the influence of $\text{Pe}_{\text{inj}}$, Pe and buoyancy on the dispersion.

## 12.2 Procedure

Fluorescein is always injected as a slow or a quick bolus using a KD Fisher scientific syringe pump (Model 1008). The maximum flow rate used is 0.45 $\mu$l/s, and the injections times range between $133 \leqslant t_{\text{inj}} \leqslant 1500$ s. Although ITDD bolus volumes typically range between 10 to 100 $\mu$l, only 60 $\mu$l boli are included in the analysis of this study. Besides reducing the number of variables, we also avoid changing the optimal concentration, i.e. 16 mg/l, in order to always inject the same amount of fluorescein.

The temperature was monitored before and after the injection of the bolus to ensure that the temperature gradient inside the annular gap remained below $\sim 1^{\circ}\text{Cm}^{-1}$ to avoid temperature induced buoyancy of the dye.

As described in section 11.6, we artificially increase the dynamic range of our concentration measurements by composing our 3D cross sections out of 37 planes, of which 8 near the catheter are scanned a second time at twice the scan speed to increase the dynamic range. The distance between planes was chosen to be 0.4 mm, ensuring the best possible spatial sampling of the dye (see section 11.4.3). We use the hardware to trigger a full 3D scan at the turning point of the oscillation cycle where the piston is at the positive maximum. This ensures that the scalar distribution is minimally deformed between the first and last plane of the 3D scan. Furthermore, because the dye is furthest away from the catheter at this point in the cycle we reduce the amount of dye that is hidden behind the catheter. We limit ourselves to a single phase in the oscillation cycle for two reasons:

1. The scan time of a full 3D cross section is $\sim 0.12$ s, which is not fast enough to obtain a sufficient temporal resolution for relevant $f_{\text{osc}}$.
2. The data generation would limit the reasonable duration of an experiment.

Unfortunately, this makes it impossible to directly measure $D_{\text{enh}} = D_{\text{enh}}(t)$ which, as explained in section 3.4, can be distinctly oscillatory with a frequency of $\omega$, or $2\omega$. However, this method does give a very good impression of the dispersion of the dye in time.

A 3D scan was taken each 3 seconds during the first 4 minutes of a bolus injection. This is longer than the injection time ($t_{\text{inj}} = 150$ s) of a fast ($Q_{\text{inj}} \approx 0.4$ $\mu$l/s), $V_B = 60$ $\mu$l bolus. Afterwards, a scan is taken every 20 seconds. The total time per experiment was 35 minutes, 10 minutes more than the longest injection time. Two different catheters were used: the clinically used silicone catheter whose tip slightly drops under the influence of gravity, and an idealized straight catheter. The orientation $\varphi$ of the catheter influences the direction of injection, and the steady streaming induced by the (uncontrollable) inclination of the catheter.

In a first large series of experiments we tested both catheters in two configurations, namely $\varphi = 0$ and $\varphi = \pi/2$, inside the constant cross section annular gap. For each configuration we varied the parameters $Q_{\text{inj}}$, $f_{\text{osc}}$, and $A_{\text{osc}}$ according to a composite factorial design [9]. Our parameter space, summarized in table 12.1, is restricted to clinically relevant values. We performed 16 experiments per configuration and for each set at least one experiment was redone using exactly the same parameters to estimate the measurement error. The parametric modeling with which we analyze the data is described in detail in section 12.3.

A second large set of experiments was performed with the slowly varying cross section geometries. We varied the characteristic slope $\epsilon = \Delta r_o/L$ and the position of the catheter

| $\hat{X}_i$ | $\min(\hat{X}_i)$ | $\hat{X}_{i,\text{ref}}$ | $\max(\hat{X}_i)$ | Dim. |
|---|---|---|---|---|
| $\varphi$ | 0 | $\pi/4$(*) | $\pi/2$ | rad |
| $Q_{\text{inj}}$ | 0.04 | 0.25 | 0.45 | $\mu$l/s |
| $d_{\text{osc}}$ | 4.4 | 7.9 | 11.2 | mm |
| $f_{\text{osc}}$ | 0.86 | 1.5 | 2.15 | Hz |
| $L$ | 25 | 50(*) | 75 | mm |
| $\Delta r_o$ | 0.7 | 1.4(*) | 2.1 | mm |

**Table 12.1:** The range of variables used for the investigation of mixing. In addition two different catheters were used, a perfectly straight metallic catheter, and a flexible silicone catheter. Values with a (*) were not systematically investigated to avoid an excessive number of parameter variations.

| # | Type | $L$ [mm] | $\epsilon$ |
|---|---|---|---|
| 1 | Constricted | 25 | 0.056 |
| 2 | Constricted | 75 | 0.019 |
| 3 | Expanded | 25 | 0.056 |
| 4 | Expanded | 25 | 0.168 |
| 5 | Expanded(*) | 3·25=75 | 0.112 |

**Table 12.2:** The different types of perturbations on the outer wall of the annular gap used for LIF experiments. (*) refers to a stacked version of three expanded sections of $L = 25$ mm. Its typical slope $\epsilon$ is based on $L = 25$, and $\Delta r_o = 1.4$ mm.

in 7 different configurations. As shown in table 12.2, we used both a constricted ($\max(r_o) = 2.5$) and an expanded ($\min(r_o) = 2.5$) geometry with respect to the constant cross section annular gap. Because of the relatively small size of the annular gap $r_{\text{H}} = 3$ mm the constricted geometries could not be used to vary $\Delta r_o$. Instead they were used to vary $L$ and the position of the catheter tip with respect to the perturbation. We placed the tip at both the maximum slope (i.e. $z$ where $r_o(z) = (\max(r_o) - \min(ro))/2$), and the local minimum ($z$ where $ro(z) = \min(r_o)$) of the perturbation. The expanded geometries were used to study the effect of varying $\Delta r_o$. The catheter tip was placed at the maximum radius of the geometry, i.e. at $z$ where $r_o(z) = \max(r_o)$. We note that the laser scanning setup as described in section 4.2 was not originally designed for precise quantitative measurements with varying cross section geometries. Therefore, during these experiments the laser light sheet was reflected of the doubly curved outer wall, and/or zones were not illuminated. It is therefore impossible to perform LIF measurements with the same degree of accuracy as in the constant cross section geometry. To achieve a higher degree of accuracy an optically matched system would have to be used. This would require a fluid with a refractive index of 1.49 and a viscosity similar to water. The latter requirement is imposed to conserve the Womersley number without affecting the basic geometry of the setup, which would have required to upscale the entire experiment, including the injection characteristics. Also the fluid should be compatible with fluorescein, and not alter the diffusion characteristics.

Given the time it takes to prepare and thermally equilibrate the experiment we could only test a selection of the factors used in the constant cross section experiments. Specifically, we chose to perform mostly fast ($t_{\text{inj}} = 150$ s) bolus experiments ($Q_{\text{inj}} = 0.4$ $\mu$l/s) at $A_{\text{osc}} = 1.49, 0, 3.74$ at $f_{\text{osc}} = 1.5$ Hz, and $f_{\text{osc}} = 0.86, 2.15$ Hz at $A_{\text{osc}} = 2.62$. A single experiment at $A_{\text{osc}} = 1.74$ and $f_{\text{osc}} = 1$ Hz was performed to check for interactions. For comparison, only a single slow injection ($Q_{\text{inj}} = 0.04$ $\mu$l/s) was tested at $f_{\text{osc}} = 1.5$ Hz, and $A_{\text{osc}} = 2.62$. In total $6 + 1 = 7$ experiments were tried with each varying cross section configuration.

Finally, we qualitatively investigated the effect of buoyancy on the dispersion by adding 0.3% of glucose to the fluorescent dye in a limited number (16) of experiments. The results are qualitatively discussed in section 12.10. In total 129 experiments were performed, each lasting 1 hour and generating about 1Gb of data each. Although additional experiments were performed to study the effect of the bolus volume $V_B$ and dye concentration $C$, these are not discussed because of an insufficient signal to noise ratio (SNR).

## 12.3 Analysis

### 12.3.1 Parametric Modeling

An important aspect of this study is to determine how enhanced mixing and steady streaming influence the dispersion of the dye as a function of the injection rate $Q_{\text{inj}}$. Given the complexity and variety of the dispersion mechanisms no analytical model can be easily constructed to predict the system response. We therefore resort to the modeling of any single system response ($\hat{Y}$, where the hat denoting dimensional quantities) around a reference state determined at reference ITDD parameters (see table 12.1). Each variable $\hat{Y}$ is chosen to characterize a specific aspect of the dispersion and is a function of a multitude of factors (i.e. $Q_{\text{inj}}$, $f_{\text{osc}}$, $A_{\text{osc}}$, etc.), which we denote by $\hat{X}_i$, where $i$ is a number assigned to each factor. $N_f$ is the number of factors, or variables, varied during the experiments. If we assume that $\hat{Y}$ is a continuous function of the factors, we can approximate the functional relation $\hat{Y} = \mathcal{F}(\hat{X}_i)$ by the first two terms of its Taylor expansion:

$$(\hat{Y} - \hat{Y}_{\text{ref}}) \approx \sum_{i=1}^{N_f} b_i(\hat{X}_i - \hat{X}_{i,\text{ref}}) + \sum_{i \leqslant j}^{N_f} b_{ij}(\hat{X}_i - \hat{X}_{i,\text{ref}})(\hat{X}_j - \hat{X}_{j,\text{ref}}) \tag{12.1}$$

where $b_{ij}$ are unknown model constants, and the subscript $_{\text{ref}}$ refers to a reference state. The values for $\hat{X}_{i,\text{ref}}$ are given in table 12.1, and the value of $\hat{Y}_{\text{ref}}$ is given separately for each model. If we take into account all the model constants, there are $N = N_f + N_f(1 + N_f)/2$ coefficients in the Taylor expansion in equation 12.1. Because equation 12.1 is an approximate relation and because the experimental response is subject to variance, the constants $b$ are determined using multi-linear regression. To determine all the unknown constants $b$ we must measure the response $k \geqslant (N + 1)$ times, at well chosen values of $\hat{X}_i$, where $k$ is the number of experiments. For easier comparison, we non-dimensionalize the factors $\hat{X}_i$ and responses $\hat{Y}$ according to:

$$X_i = \frac{2(\hat{X}_i - \hat{X}_{i,\text{ref}})}{\Delta \hat{X}_i} \qquad Y = \frac{2(\hat{Y} - \hat{Y}_{\text{ref}})}{\Delta \hat{Y}} \tag{12.2}$$

Hence, the non-dimensional $X_i$ ranges between -1 and 1 around its reference state, $X_{i,\text{ref}} = 0$. $\hat{Y}_{\text{ref}}$ is the average value of $\hat{Y}$ that was measured during all the experiments. To

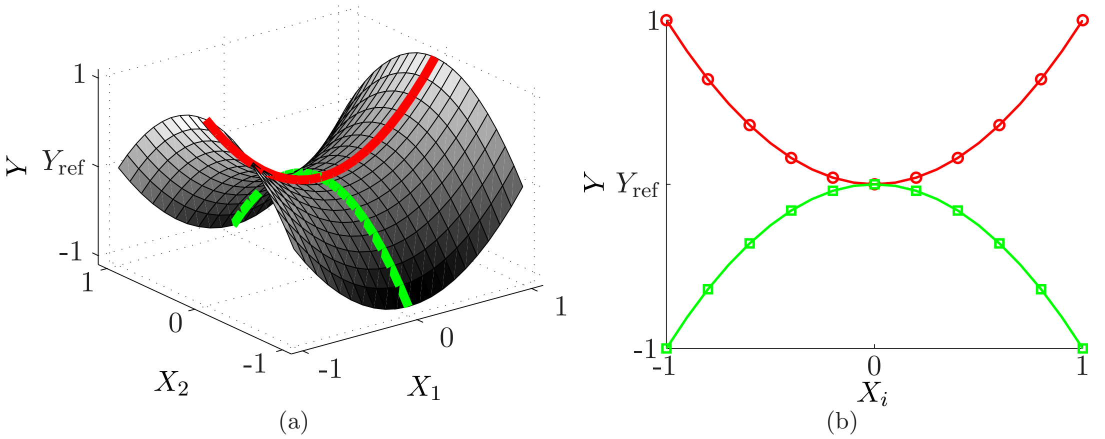

**Figure 12.1:** Illustration of the method of presenting the parametric models based on the model described by equation 12.3. Figure (a) shows the non-dimensional response surface $Y$, and (b) shows the amplitude of both variables $X_i$ on $Y$ by setting the other variable $X_j$, $\forall j \neq i$ to its reference state $X_{j,\text{ref}} = 0$. In this example $Y_{\text{ref}} = 0$.

determine whether the effect of $X_j$ is statistically significant, we calculate its $p$-value[1]. If for example the $p$-value for the effect of $X_j$ is larger than 0.05, we consider it statistically insignificant, and set $b_j = b_{ij} = 0$. With a relatively small number of experiments, it is more likely that the interactions $b_{ij}$ are statistically insignificant. This explains why the number of terms in the models we discuss is always smaller than $N$.

As a demonstration of our method we examine a hypothetical model described by:

$$Y = b_{11}X_1^2 + b_{22}X_2^2 = X_1^2 - X_2^2 \tag{12.3}$$

where $b_{11} = 1$, and $b_{22} = -1$ are the only statistically significant model constants. The most visual way to interpret this relation is to use a different axis for each term in the Taylor expansion, as is done in figure 12.1(a). Although this is possible if there are only 1 or 2 terms (such as our example), this is unpractical for 3 or more terms[2]. For the models we present in this thesis, we therefore limit our analysis to the importance of each $X_i$ separately by plotting $Y$ and setting all the other factors $X_j$ to their reference state $X_{j,\text{ref}} = 0$, $\forall j \neq i$. This is shown for our example model in figure 12.1(a). We only deviate from this principle to plot interaction terms of the form $b_{ij}X_iX_j$, $\forall i \neq j$, which are saddle points in space. For those terms we plot $Y$ by setting all the other constants $b$ to zero. Although these models are sufficient to investigate the order of magnitude of an effect, they give no insight into the physics of the dispersion. For this we rely on qualitative observations.

For each model we give the adjusted r-square value $r^2_{\text{adj}}$. This indicates the percentage of experimental variance that is accounted for by the model[3]. Only models with $r^2_{\text{adj}} \geqslant 0.75$

---

[1] The p-value is the probability of obtaining a result at least as extreme as a given data set due to chance.

[2] In this case the response can be considered as an $N$-dimensional hypersurface

[3] Compared to the normal $r^2$ value, $r^2_{\text{adj}}$ is adjusted for the number of terms in the model, and can only increase if the value of a newly included term is significant, defined by the p-value.

that are valid for at least three out of four different configurations of catheter type and $\varphi$ are considered. Unfortunately an experiment with a slowly varying cross section is characterized by a large number of parameters, such as the position of the injection ports and the catheter tip with respect to the cross section variation, $L$, and $\epsilon$. Therefore not enough experiments were performed to identify statistically significant models for these experiments.

### 12.3.2 Data Reduction

As hypothesized in section 11.4.3 an incremental step of the light sheet $\Delta x \approx 0.4$ mm results in an optimal sampling of the dye. We define a discrete voxel as the volume equal to

$$(V_{\text{vox}})_{i,j,k} = \chi_{j,k}^2 d_{\text{plane},i} \tag{12.4}$$

where $\chi_{j,k}$ is the pixel width and height inside an image, $d_{\text{plane},i} = 0.4$ is the approximate laser plane thickness, and where $(i\mathbf{e}_x, j\mathbf{e}_y, k\mathbf{e}_z)$ is its discrete position in Cartesian space. If we ignore the image deformations by the inner tube as shown in section 11.3.2 and compensate for lens effects, we can assume that $(V_{\text{vox}})_{i,j,k} = K,\ \forall(i,j,k)$, where $K$ is a constant. Therefore, $m(\mathbf{x}_i, t) = KC(\mathbf{x}_i, t)$, where $m$ is the mass of dye inside the voxel. Under the same hypotheses, it is not unreasonable to approximate the concentration of the scalar in between the measured planes by linear interpolation. We use this to transform the scanned data from a cartesian to the more appropriate cylindrical coordinate system. As used throughout this thesis, the origin is placed at the axis of the annular gap with the catheter tip at $\theta = 0, r = 2, z = 0$. This coordinate system was previously shown in figure 4.2. Under these assumptions it is easy to integrate $m$ with respect to the coordinates and consider section area averages such as $\bar{C}(z,t)$, useful for comparison with the 1D enhanced mixing theory in section 3.4. The integration over all the directions gives the total amount of measured mass inside the control volume (CV, defined by the field of view of the camera). The mass conservation is written as:

$$\dot{m}_{\text{inj}} = \dot{m}_{\text{CV}} + \dot{m}_{\text{out}} + \dot{\varepsilon} \tag{12.5}$$

where $\dot{m}_{\text{inj}}$ is a source term corresponding to the injection rate of fluorescein, $\dot{m}_{\text{CV}}$ is the species mass flow measured inside the control volume, $\dot{m}_{\text{out}}$ is the mass flow out of the CV, and $\varepsilon$ is an error term expressing primarily the limited sensitivity and dynamic range of our system, but also includes the effect of laser attenuation (see section 11.5.3). $m$ is always non-dimensionalized with the total injected mass, which depends on the volume and concentration of the injected scalar. When $m_{\text{CV}}(t) \approx 1$ this indicates either a small axial spread $m_{\text{out}}$, or a small error term $\varepsilon$. Although the error term is always influenced by laser beam attenuation, for large $t$ the error term is primarily determined by the detection threshold of the camera and the limited height of the CV. Low initial concentrations are indicative of a diffusion dominated regime, and will give rise to a relatively large initial $\varepsilon$.

## 12.4 Straight Tube and Catheter

### 12.4.1 Qualitative Observations

A typical distribution of the dye has been observed to have two main features. First, a considerable portion of the dye will remain localized near the catheter and travel axially along its length. This is probably related to enhanced mixing. Second, when the dye reaches the catheter tip, it is dispersed in both the $\mathbf{e}_\theta$ and $\mathbf{e}_z$ directions by steady streaming recirculation zones near the catheter tip. The shape of the dispersion therefore often resembles a mushroom. This is due to steady streaming effects and can be observed in for example figure 12.2. The similarity of these projections of dye concentration with the numerically computed steady streaming patterns in section 7.5 confirms the importance of the catheter tip. We note that the specific spread of the scalar is dependent on catheter orientation $\varphi$, even though the shape of the distribution is conserved. We observe in figure 12.2 that the dye stays near the injection ports longer for $\varphi = \pi/2$. Although we have speculated in chapter 7 that the enhanced mixing might be increased in the $\varphi = 0$ direction (see in particular figure 7.6), movement and positioning errors of the catheter also have an (unknown) influence.

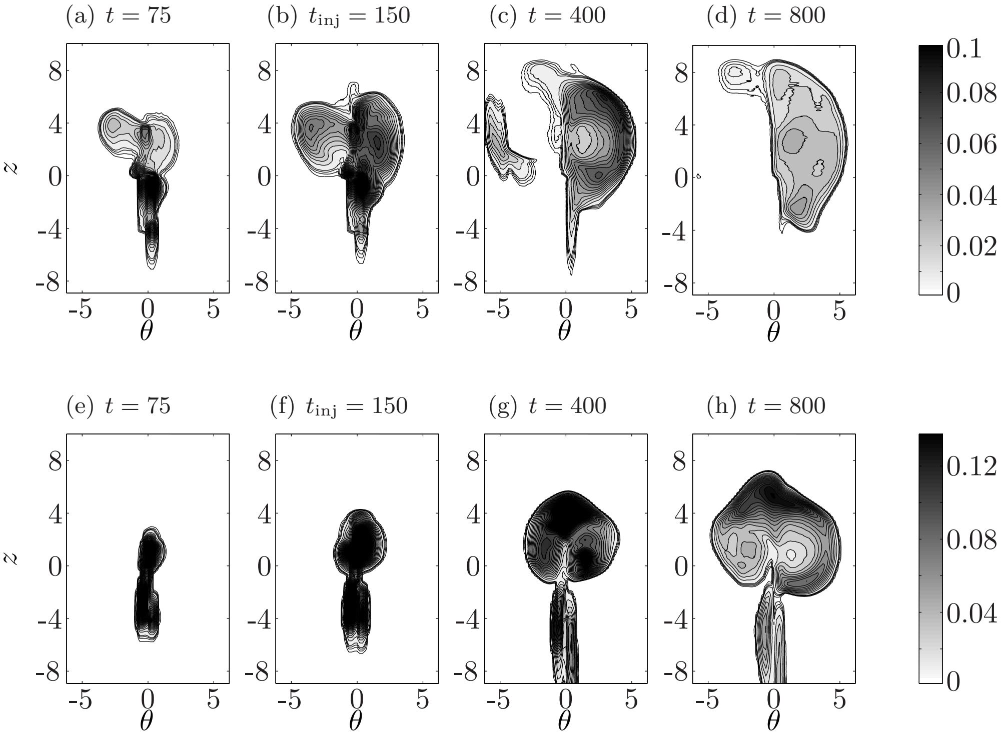

**Figure 12.2:** $(\theta, z)$-projection of a single $V_B = 60$ $\mu$l injected with the straight metal catheter at $Q_{\text{inj}} = 0.4$ $\mu$l/s. The orientation of the catheter was $\varphi = 0$ for (a)-(d), and $\varphi = \pi/2$ for (e)-(h). The oscillation parameters were the same for both injections, namely $f_{\text{osc}} = 1$ Hz, and $A_{\text{osc}} = 1.74$. The catheter tip is at $(\theta = 0, z = 0)$, shown in figure 4.2.

We qualitatively study the influence of the orientation $\varphi$ of the flexible silicone catheter in figure 12.3. The dispersion is much higher in the case of $\varphi = \pi/2$ compared with the

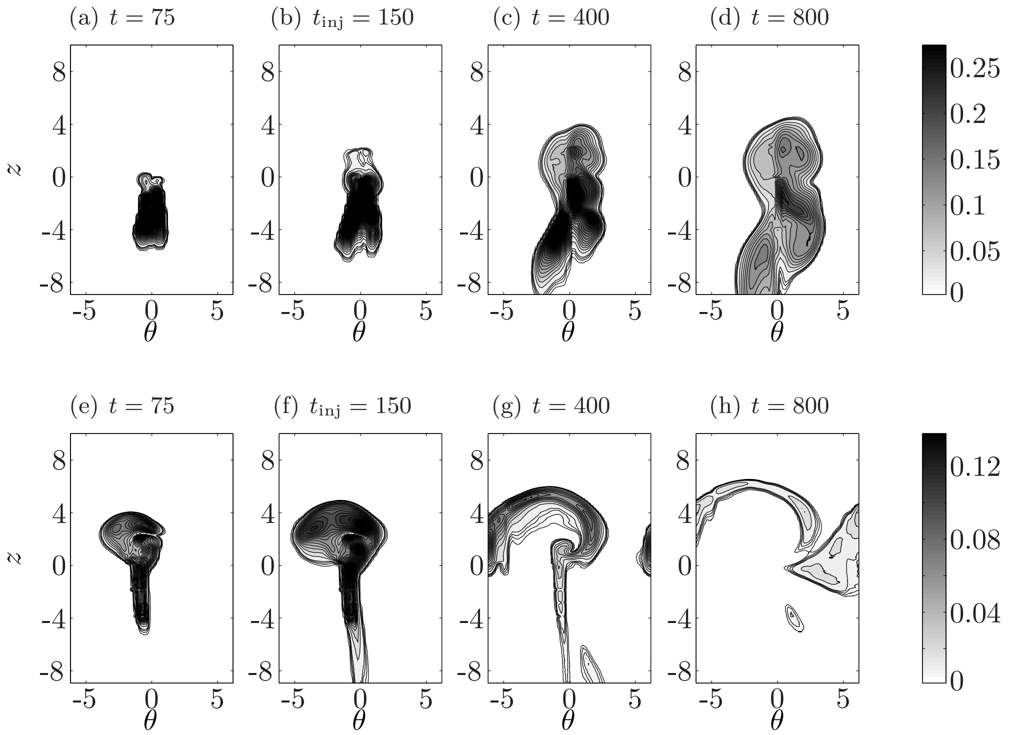
(a) $t = 75$ (b) $t_{\mathrm{inj}} = 150$ (c) $t = 400$ (d) $t = 800$

(e) $t = 75$ (f) $t_{\mathrm{inj}} = 150$ (g) $t = 400$ (h) $t = 800$

**Figure 12.3:** $(\theta, z)$-projection of a single $V_B = 60$ $\mu$l injected with the silicone Medtronic catheter at $Q_{\mathrm{inj}} = 0.4$ $\mu$l/s. The orientation of the catheter was $\varphi = 0$ for (a)-(d), and $\varphi = \pi/2$ for (e)-(h). The oscillation parameters are the same as in figure 12.2 with $f_{\mathrm{osc}} = 1$ Hz, and $A_{\mathrm{osc}} = 1.74$.

metal catheter at the same orientation. This is probably because of the slight curvature of this specific catheter, which, due to its specific inclination, is larger for $\varphi = \pi/2$. We hypothesize that this curvature also generates recirculations that can trap the dye and keep it from quickly reaching the tip. This would explain the deviant distribution pattern observed in figures 12.3(a)-12.3(d). We conclude that the metal catheter is a better reference for catheter tip related recirculations, but think that the Medtronic catheter more accurately models the clinical reality.

### 12.4.2 Bulk movement

In the previous section we have observed that the dye can remain relatively near the catheter instead of being entrained into the recirculation cell near the tip (see figures 12.3(a)-12.3(d)). We quantitatively investigate the nature of this phenomenon by calculating the center of gravity $(\theta_{\mathrm{g}}, z_{\mathrm{g}})$ of the dye in the $(\theta, z)$-projections, using a 2D version of equation 3.10. We have observed that the dye is usually centered on $\theta_{\mathrm{g}} = 0$, while $z_{\mathrm{g}}$ gives an indication of the direction of the bulk of the dye. An example is shown in figure 12.4(a). Initially $z_{\mathrm{g}}(t = 0) \approx -12$ mm which corresponds to the location of the injection ports. Usually $z_{\mathrm{g}}(t)$ tends towards the catheter tip at $z = 0$ and subsequently reaches a

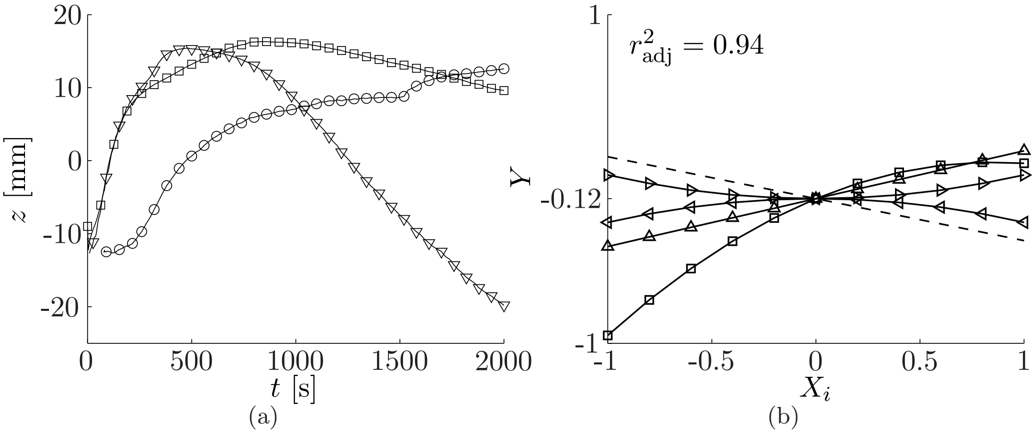

(a) (b)

**Figure 12.4:** (a) shows the axial position of the center of gravity $z_{\mathrm{g}}(t)$. The arbitrarily chosen curves were obtained with a $V_B = 60$ $\mu$l injection with the metal catheter at $\varphi = 0$, and (□) $Q_{\mathrm{inj}} = 0.4$ $\mu$l/s, $A_{\mathrm{osc}} = 1.74$, $f_{\mathrm{osc}} = 2$ Hz, (○) $Q_{\mathrm{inj}} = 0.04$ $\mu$l/s, $A_{\mathrm{osc}} = 1.74$, $f_{\mathrm{osc}} = 2$ Hz, and finally (▽) $Q_{\mathrm{inj}} = 13.2$ $\mu$l/s, $A_{\mathrm{osc}} = 2.62$, and $f_{\mathrm{osc}} = 2.1$ Hz. (b) shows the parametric model for $\bar{z}_{\mathrm{g}}(t)$ ($\Delta\hat{Y} = 20$ mm, and $\hat{Y}_{\mathrm{ref}} = -0.8$ mm). The factors included in the model are: $f_{\mathrm{osc}}$ (−−), $A_{\mathrm{osc}}$ (△), $Q_{\mathrm{inj}}$ (□), $A_{\mathrm{osc}}f_{\mathrm{osc}} \propto$ Re (◁), and finally $A_{\mathrm{osc}}Q_{\mathrm{inj}}$ (▷).

maximum above it. This is the influence of the steady streaming. The longer the dye stays localized around the catheter tip, the longer $z_{\mathrm{g}} > 0$. This is a function of the dispersion characteristics. As dye leaves the CV from above, the $z_{\mathrm{g}}$ moves down again to $z_{\mathrm{g}} < 0$, where small quantities of dye remain. To characterize the position of $z_{\mathrm{g}}$ we calculate the temporal mean $\bar{z}_{\mathrm{g}}(t)$. The parametric model constructed with $\bar{z}_{\mathrm{g}}(t)$ is shown in figure 12.4(b). It has a $r^2_{\mathrm{adj}} = 0.94$, and the largest effect is $Q_{\mathrm{inj}}$. Importantly, the mean position of the dye over all the experiments is $\hat{Y}_{\mathrm{ref}} = -0.8$ mm, directly at the catheter tip. This is therefore the region that is, on average, subject to the most dye. This observation can be directly correlated to the formation of granulomas at the catheter tip. All other factors constant, a lower $Q_{\mathrm{inj}}$ implies that the dye stays nearer the injection ports for longer. The dispersion for low $Q_{\mathrm{inj}}$ has been observed to be much more diffuse, so there might be more dye near or above the catheter tip than we can measure. The other factors in the model are of similar amplitude, and cannot be easily interpreted.

To further our understanding of the axial spread we constructed a simple bin model that estimates how much dye has left the top, or the bottom, of the entire control volume. We calculated how much dye was inside a central control volume (height of CV is smaller than the image height) bounded by two smaller exit volumes (the top and bottom of the images). The rate at which the dye leaves the central volume is estimated by calculating the time derivative $\dot{m}_{\mathrm{CV}}$. The fraction of $m_{\mathrm{out}}$ leaving the CV from the top is modeled as the ratio of the dye in the upper exit volume to the dye in the lower volume. We identified a parametric model for the ratio of the average rate at which the dye leaves the top compared to the average rate the dye leaves the bottom. The result is shown in figure 12.5. The oscillation amplitude $A_{\mathrm{osc}}$ is modeled as a linear term, and has the largest effect on the relative rate the dye leaves the control volume from the top. Importantly, $Q_{\mathrm{inj}}$ only

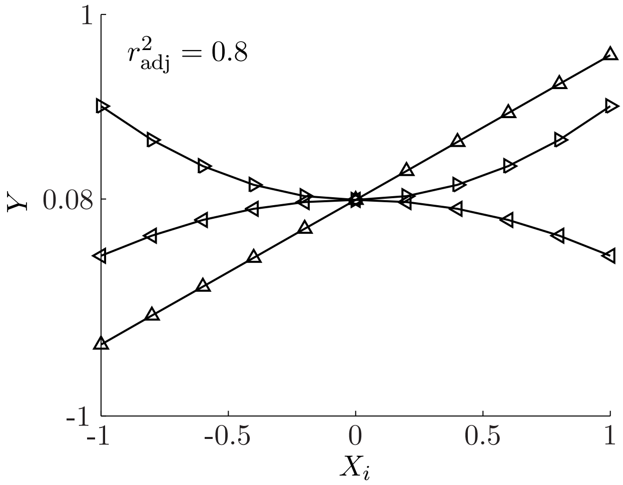

**Figure 12.5:** The parametric model for the ratio of the mean top and bottom disappearance rates computed with a simple bin model ($\Delta\hat{Y} = 1$, and $\hat{Y}_{\mathrm{ref}} = 0.55$). The factors included in the model are: $A_{\mathrm{osc}}$ ($\triangle$), $A_{\mathrm{osc}} f_{\mathrm{osc}} \propto \mathrm{Re}$ ($\triangleleft$), and finally $A_{\mathrm{osc}} Q_{\mathrm{inj}}$ ($\triangleright$).

appears in a positive interaction term with $A_{\mathrm{osc}}$. This implies that $Q_{\mathrm{inj}}$ could perhaps be used to obtain higher concentration of dye above the catheter tip, but only if $A_{\mathrm{osc}}$ is high enough. The third term is an interaction of $-bf_{\mathrm{osc}}A_{\mathrm{osc}}$, which is proportional to the Reynolds number ($= \alpha^2 A_{\mathrm{osc}}$) of the flow, but could also be related to enhanced diffusion. For high $A_{\mathrm{osc}}$ and $f_{\mathrm{osc}}$ the amount of dye leaving the top decreases.

## 12.5 Mixing Parameter Φ

To characterize the mixing in the $(\theta, z)$ projections, we introduce the concept of mixing using $\langle C_{\mathrm{rms}} \rangle$:

$$\langle C_{\mathrm{rms}} \rangle = \sqrt{\langle (C(\theta, z) - \langle C(\theta, z) \rangle)^2 \rangle} \tag{12.6}$$

or the root mean square deviation of $C(\theta, z)$ compared to the average concentration in the CV. We take into account the entire $(\theta, z)$-projection. $\langle C_{\mathrm{rms}} \rangle \to 0$ indicates a very homogeneous or diffuse spread, while $\langle C_{\mathrm{rms}} \rangle \to \max(\langle C_{\mathrm{rms}} \rangle)$ indicates an inhomogeneous spread, or one that is advection dominated. The value of $\max(\langle C_{\mathrm{rms}} \rangle)$ is dependent on the volume of the undiluted dye per CV. Because our CV is relatively large compared to $V_B$, and for convenience, we define a normalized mixing parameter $\Phi$:

$$\Phi = \frac{0.2 - \langle C_{\mathrm{rms}} \rangle}{0.2} \tag{12.7}$$

where $\Phi = 0$ refers to the most unmixed state observed during all experiments, and $\Phi = 1$ refers to a perfect homogeneous mixture. An example of $\Phi(t)$ for three different experiments is shown in figure 12.6. Each arbitrarily chosen curve shows a different tendency. We characterize the graphs using two points: $\min(\Phi(t))$ to indicate the minimal mixing state at any time during the experiment, and $\Phi(t = 1500)$. Because $t_{\mathrm{inj}} = 1500$ s was the longest injection time, $\Phi(t = 1500)$ is considered the mixing at equal dose. $\min(\Phi)$ is

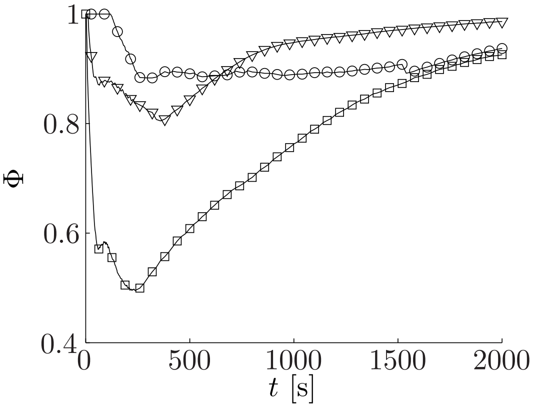

**Figure 12.6:** Three typical curves of $\Phi(t)$. The arbitrarily chosen curves were the results of a $V_B = 60\ \mu$l injection with the metallic catheter at $\varphi = 0$, and (□) $Q_{\text{inj}} = 0.4\ \mu$l/s, $A_{\text{osc}} = 1.74$, $f_{\text{osc}} = 2$ Hz, (○) $Q_{\text{inj}} = 0.04\ \mu$l/s, $A_{\text{osc}} = 1.74$, $f_{\text{osc}} = 2$ Hz, and finally (▽) $Q_{\text{inj}} = 0.22\ \mu$l/s, $A_{\text{osc}} = 2.62$, and $f_{\text{osc}} = 2.1$ Hz.

typically found at the end of the bolus injection time $t_{\text{inj}}$, indicating that the dispersion mechanisms need time to transport the dye. Furthermore, the minimum mixing state is lower for lower $Q_{\text{inj}}$. For each measure we were able to identify a parametric model, shown in figure 12.7. The models were calculated based on the constant cross section geometry measurements. First, we note that the model for min(Φ), shown in 12.7(a), has a relatively high $r^2_{\text{adj}} = 0.96$. The main effects are $Q_{\text{inj}}$ which decreases min(Φ), and $A_{\text{osc}}$, which increases min(Φ). This enforces the claim that the dispersion for high injection rates is initially advection dominated. From experimental observations we know that this spread is related to the steady streaming at the catheter tip and not to the energy imparted by

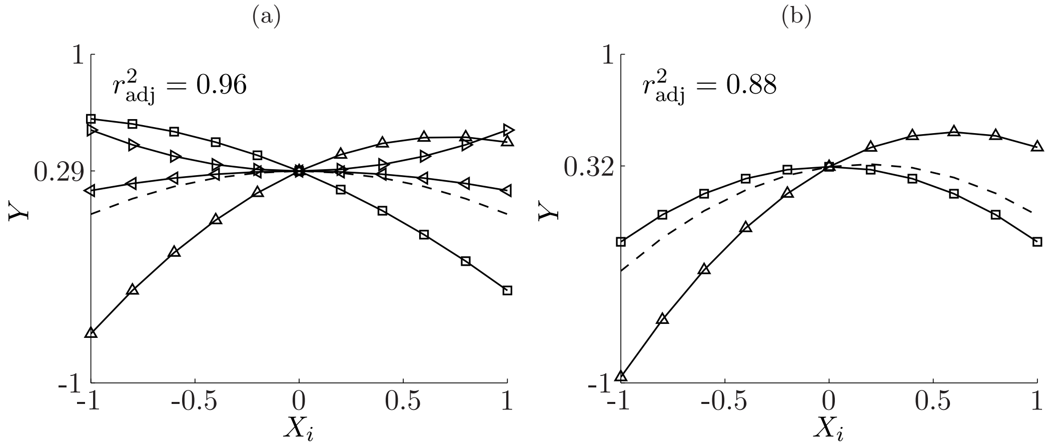

**Figure 12.7:** The parametric model for (a) $\min(\Phi(t))$, $\forall t$ ($\Delta\hat{Y} = 0.98$, and $\hat{Y}_{\text{ref}} = 0.79$), and (b) the mixing parameter $\Phi(t = 1500\text{s})$, or at equal dose ($\Delta\hat{Y} = 0.19$, and $\hat{Y}_{\text{ref}} = 0.96$). The factors included in the model are $f_{\text{osc}}$ (−−), $A_{\text{osc}}$ (△), and $Q_{\text{inj}}$ (□), $A_{\text{osc}}Q_{\text{inj}}$ (▷), and $f_{\text{osc}}Q_{\text{inj}}$ (◁).

the injection itself. The influence of $A_{\text{osc}}$ must be related to the enhanced diffusion which decreases the concentration gradients. We note that the diminishing of the effect observed at high $A_{\text{osc}}$ might be related to the limited sensitivity of our system, which makes it difficult to accurately distinguish between cases with high diffusion. The other effects in the model are $f_{\text{osc}}$, $Q_{\text{inj}} \cdot f_{\text{osc}}$, and $Q_{\text{inj}} \cdot A_{\text{osc}}$. They are relatively small and not easily interpreted.

Based on its parametric model shown in 12.7(b), the value of $\Phi(t = 1500\ s)$ is correlated with a quadratic term $A^2_{\text{osc}}$. A high $A_{\text{osc}}$ increases the mixing at equal dose, but the effect is diminished for high values of $A_{\text{osc}}$. This is caused by the fact that $\Phi(t)$ is bounded ($\max(\Phi) = 1$), so a higher diffusion can only marginally increase $\Phi$. The effects of both $f^2_{\text{osc}}$ and $Q^2_{\text{inj}}$ are similar and relatively small. They suggest that an optimal injection speed and oscillation frequency exist to achieve maximum mixing at equal dose. We consider the effect of $Q_{\text{inj}}$. The spread is less homogeneous (lower $\Phi$) for lower $Q_{\text{inj}}$. This can be linked to the observation that at low injection rates there is always a small but relatively high concentration zone near the injection ports. At high $Q_{\text{inj}}$ the dye has had more time to disperse, but maybe not sufficiently to clear the CV. The smaller our CV, the higher the optimal $Q_{\text{inj}}$ would therefore be. At high mixing we must be careful to interpret the results, because we cannot accurately measure low concentrations. For what it is worth, we note that the optimum $Q_{\text{inj}}$ predicted by the model is significantly higher than the slow continuous infusion used clinically.

## 12.6 Varying Outer Wall and Catheter

Based on the results discussed in part I we expect that slowly varying cross section geometries will increase the axial dispersion through convective transport and influence the steady streaming at the catheter tip. First we qualitatively investigate the influence of a constricted geometry on the dispersion using the $(\theta, z)$-projection of the dye in figure 12.8. Although the shape of the dispersion tends towards the characteristic mushroom shape observed in the constant cross section geometry (see figures 12.2 and 12.3), there is clear evidence of increased axial dispersion. The mushroom shape never fully develops, and dye is axially dispersed.

To qualitatively study this phenomenon we measured the dispersion in a single plane $(r, \theta = 0, z)$ directly above a metal injection catheter with orientation $\varphi = \pi/2$. To increase the signal directly above the tip we used a slightly modified version with two injection ports just below the tip, at $z \approx -1$ mm. The catheter was placed in a constant cross section annular gap, or directly below a constricted (#1, $\epsilon = 0.028$), or an expanded perturbation (#4, $\epsilon = 0.084$)[4]. We injected a large bolus ($V_B = 100\ \mu$l, $Q_{\text{inj}} = 0.4\ \mu$l/s) of high concentration ($C = 32$ mgl$^{-1}$) and studied the evolution in time. We used a relatively low amplitude oscillation of $A_{\text{osc}} = 1.67$ and $f_{\text{osc}} = 1$ Hz.

The concentration in the plane in the constant cross section geometry is shown in figure 12.9. For easier comparison with the results of the constricted and expanded geometries, we have organized the images according to the height above the tip. Close inspection reveals a small recirculation cell near the inner wall of the annular gap. This cell must be due to the catheter inclination, because when placed perfectly in the annular gap, the

---

[4] The number is reference to a specific geometry in table 12.2

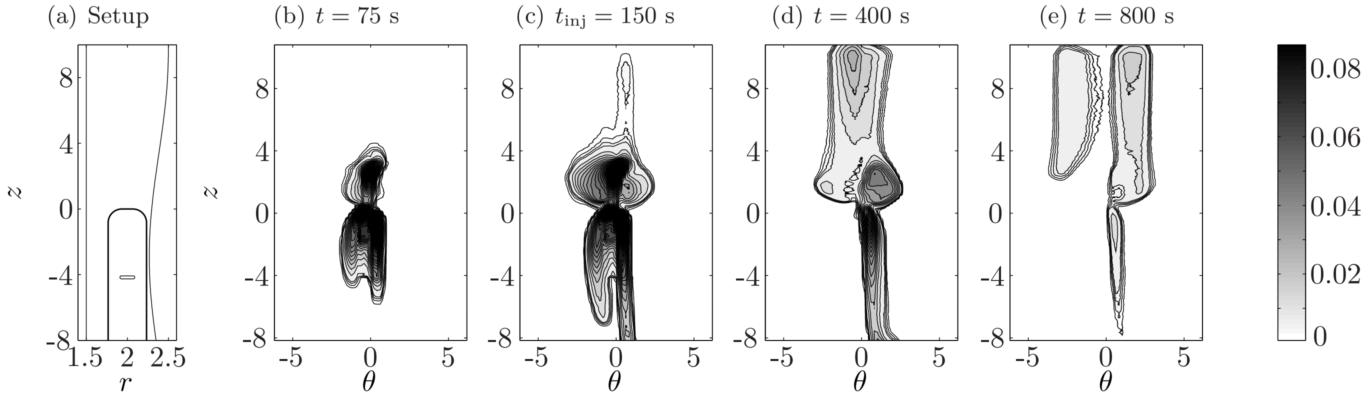

**Figure 12.8:** $(\theta, z)$-projection of a single $V_B = 60$ $\mu$l bolus injected into a constricted geometry (a) annular gap with $\epsilon = 0.019$ (#2) with the metallic ideal catheter at $Q_{\mathrm{inj}} = 0.4$ $\mu$l/s after $t = 75$ (b), $t_{\mathrm{inj}} = 150$ (c), 400 (d), and 800 seconds (e). The orientation of the catheter is $\varphi = 0$, and the oscillation parameters are $f_{\mathrm{osc}} = 1.5$ Hz, and $A_{\mathrm{osc}} = 1.49$.

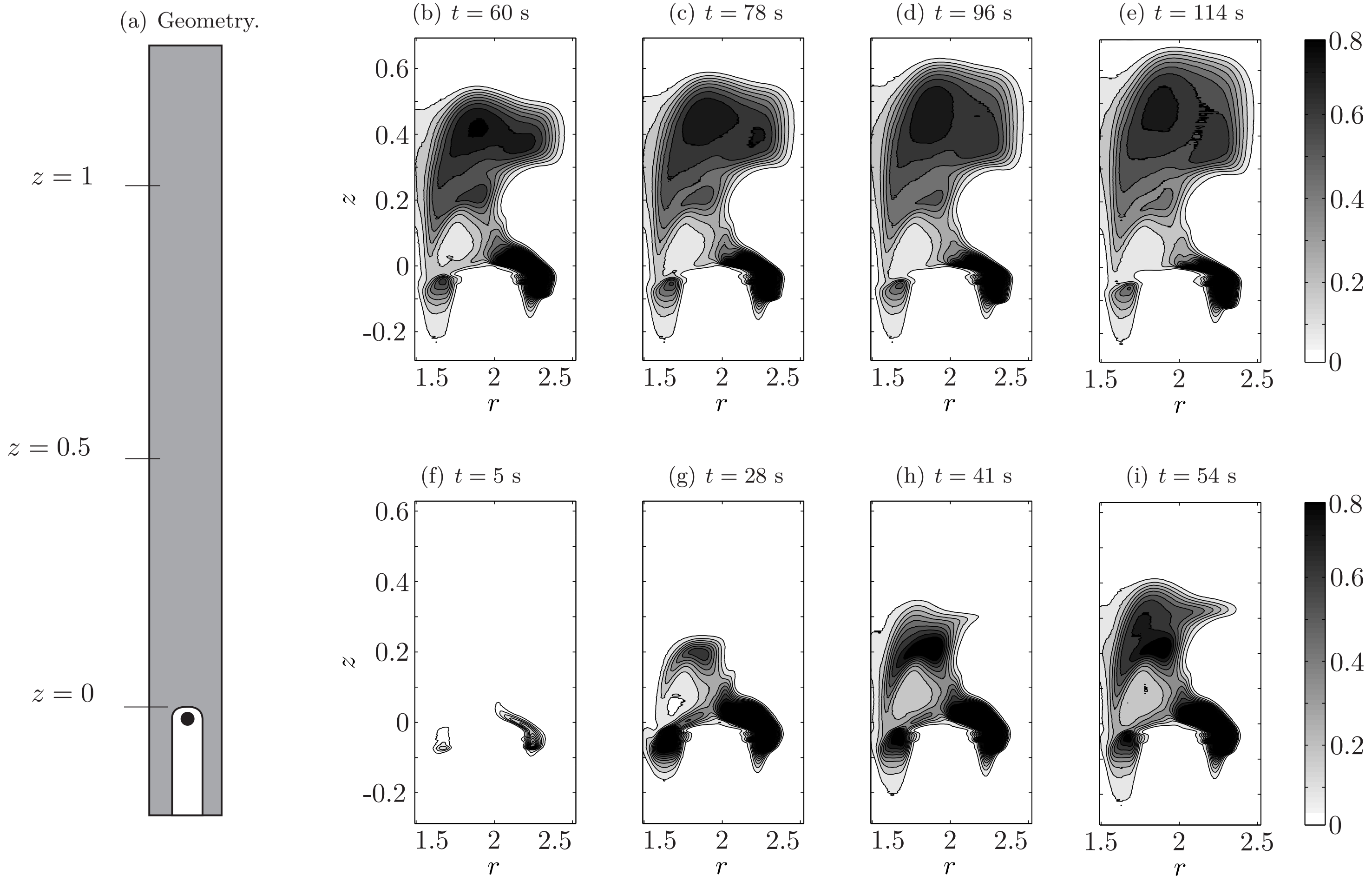
(a) Geometry.

(b) $t = 60$ s

(c) $t = 78$ s

(d) $t = 96$ s

(e) $t = 114$ s

(f) $t = 5$ s

(g) $t = 28$ s

(h) $t = 41$ s

(i) $t = 54$ s

**Figure 12.9:** Concentration $C$ in a single plane $(r, \theta = 0, z)$ directly above the injection catheter inside the constant cross section annular gap at different moments. The annular gap, shown in (a) is drawn to scale, the graphs are not. The figures at the top, i.e. (b)–(e) show the dispersion in the upper part of the geometry, while (f)–(i) show the dispersion in the bottom half. The $z$-coordinate is normalized to $L = 25$ mm (the height of the perturbations in figures 12.10 and 12.11), while $r$ is normalized with the hydraulic radius $r_{\mathrm{H}}$ of the annular gap. $C$ is given in normalized pixel values.

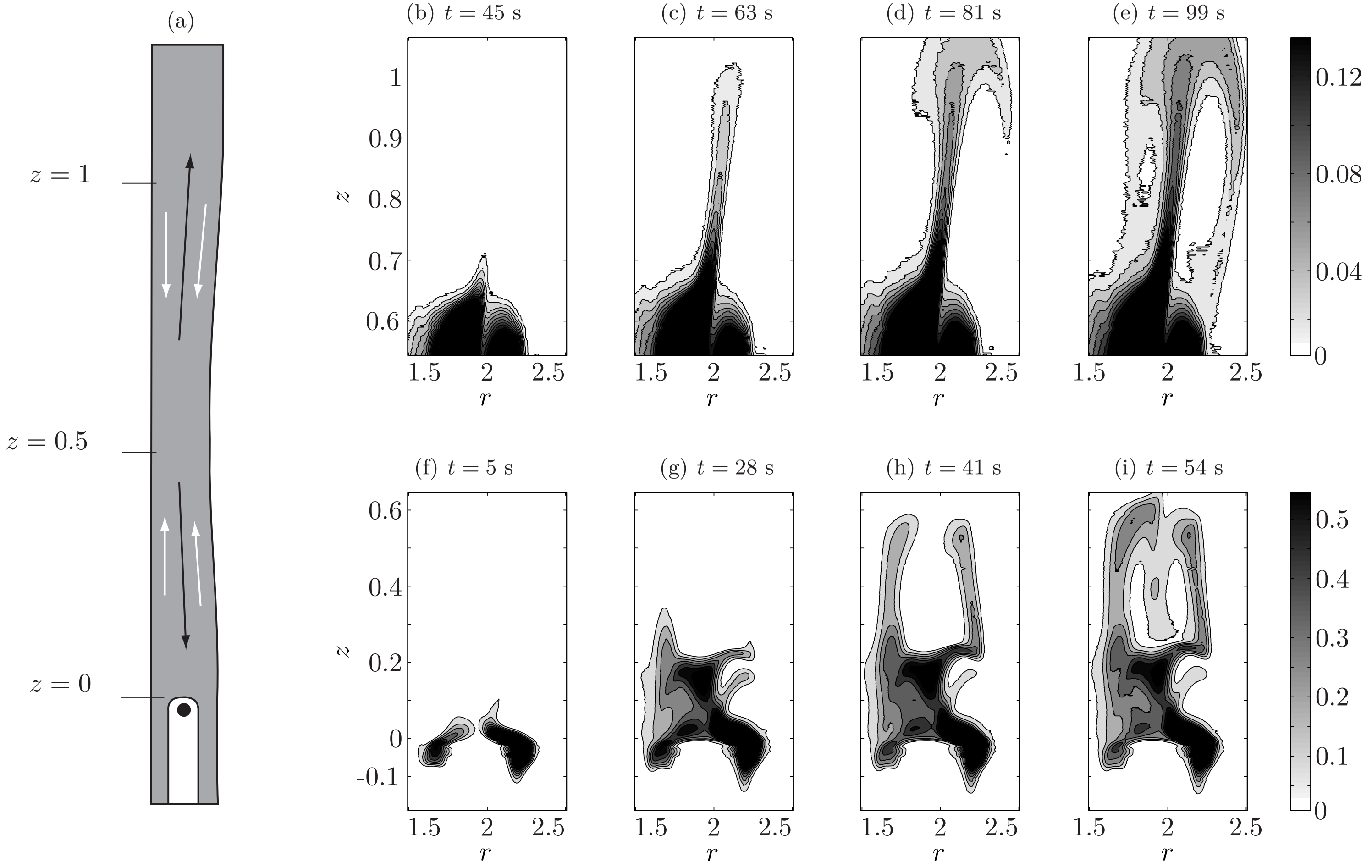

**Figure 12.10:** Concentration $C$ in a single plane inside the lower and upper part of the constricted geometry (#1, $\epsilon = 0.028$) at different moments. The geometry, shown in (a), is drawn to scale but the graphs are not. The figures at the top, i.e. (b)–(e) show the dispersion in the upper half of the geometry, while (f)–(i) show the dispersion in the bottom half. The black arrows indicate the theoretical direction of the midline velocity, while the white arrows the velocity direction near the walls. The $z$-coordinate is normalized to the height of the perturbation $L = 25$ mm, while $r$ is normalized with the hydraulic radius $r_{\mathrm{H}}$ of the constant cross section annular gap. The concentration is given in normalized pixel values and the injected $V_B$ and $C$ are the same for figures 12.9 and 12.11. Because the light sheet comes from above, the area below the dent is poorly illuminated.

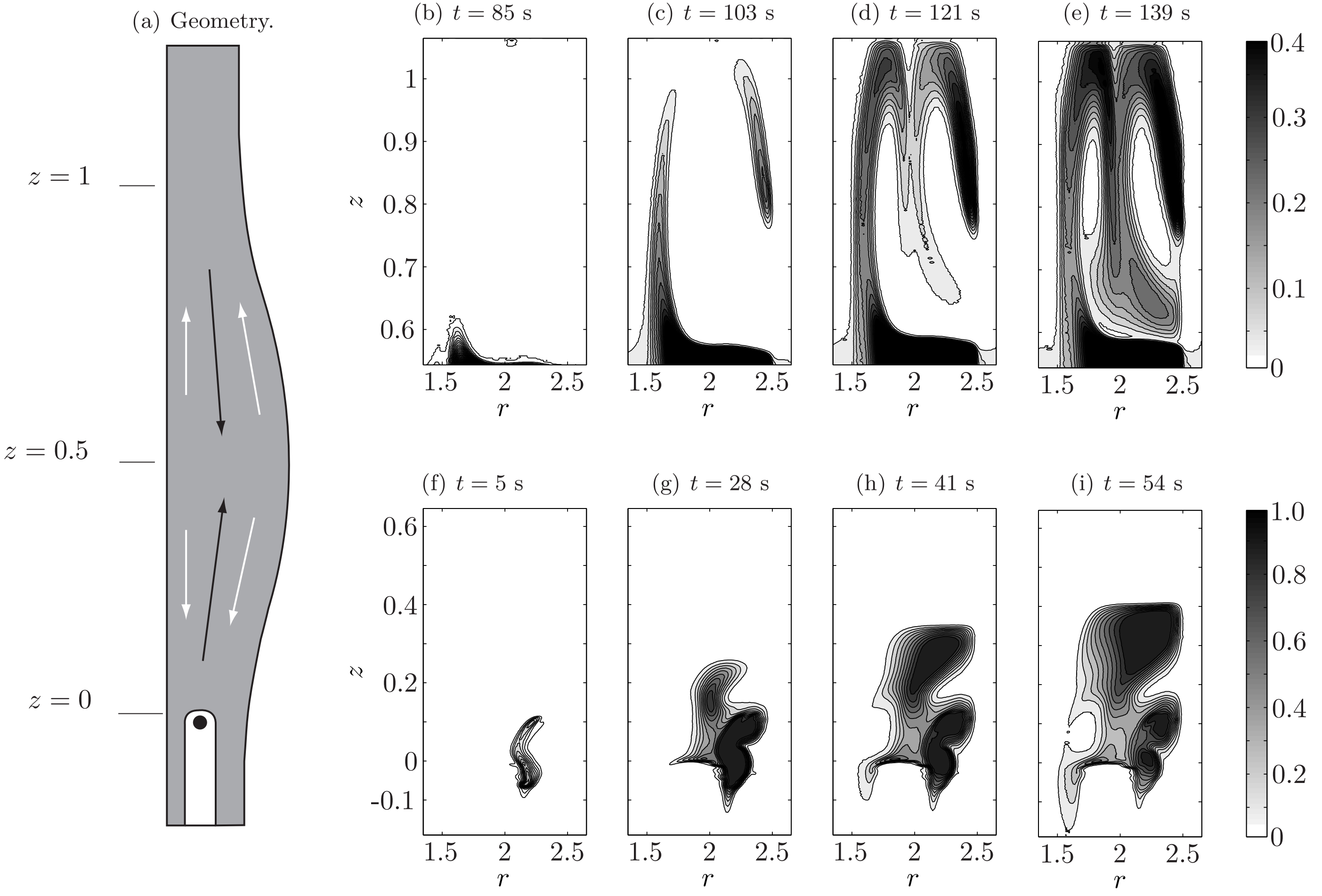

**Figure 12.11:** Concentration $C$ in a single plane inside the lower and upper part of the expanded geometry (#4, $\epsilon = 0.084$) at different moments. The geometry, shown in (a), is drawn to scale, but the graphs are not. The figures at the top, i.e. (b)–(e) show the dispersion in the upper part of the geometry, while (f)–(i) show the dispersion in the bottom part. The black arrows indicate the theoretical direction of the midline velocity, while the white arrows the velocity direction near the walls. The $z$-coordinate is normalized to the height of the perturbation $L = 25$ mm, while $r$ is normalized with the hydraulic radius $r_{\mathrm{H}}$ of the constant cross section annular gap. The concentration is given in normalized pixel values and the injected $V_B$ and $C$ are the same for figures 12.9 and 12.10. Because the light sheet comes from above, the radial extension in the expanded perturbation is not illuminated.

steady streaming in this plane would be exclusively in the downwards direction.

The concentration evolution in the plane inside the constricted geometry is shown in figure 12.10. We can immediately appreciate the effect of geometry generated steady streaming. The images are organized to link the direction of the dispersion to the geometry. The axial displacement of the dye is limited directly above the catheter, but is dramatically increased in the boundary layers. After $t = 54$ s, at $z \approx 0.5$, the dye is entrained downwards, following the streamlines of the lower recirculation cell. The same phenomena can be observed in the upper part of the geometry, except that the centerline velocity is now directed upwards.

At first, the concentration in the expanded geometry is remarkably similar to that observed in constant cross section gap. In comparison however, the dye remains more concentrated while its axial transport is similar. In line with the conclusions from the experimental PIV study in chapter 8 we hypothesize that because the local leading order velocity is lower in an expanded geometry compared to the constricted and constant cross section geometries, this decreases the (dimensional) amplitude of the steady streaming at the catheter tip. Furthermore, it is not unlikely that in the bottom half of the geometry the downward direction of the steady streaming generated by the catheter tip counters the upward steady streaming on the midline of the changing cross section geometry, thereby limiting the steady streaming in this plane. Compared to the constricted geometry, the dye takes longer to cross the symmetry plane of the geometry, probably because it needs to travel a larger distance to reach the boundary layers. Once on the other side of the geometry ($z \geqslant 0.5$), however, the influence of the catheter streaming is negligible and the dye qualitatively follows the steady streaming pattern.

In conclusion, we first note that the effect of the high injection rate is negligible. Furthermore, whereas the dye travels roughly 13 mm above the catheter tip during 72 oscillation cycles in the constant cross section annular gap, it travels the full height of the changing section and back again in the same time in the constricted and expanded geometries ($\approx 50$ mm). We note that the dye experiences limited diffusion on the short time scale of these experiments. This confirms that steady streaming is relatively quick even though the characteristic velocities of the varying cross section geometries are small ($O(0.01\ \omega d_{\mathrm{osc}}) \approx 0.3\ \mathrm{mms}^{-1}$).

## 12.7 Axial Spread $\bar{C}(z,t)$

The only azimuthal steady streaming is expected to occur in a small region surrounding the catheter tip. To study the dispersion, we therefore calculate the mean axial concentration as a function of time. To obtain $\bar{C}(z,t)$, we integrate the concentration $C = C(r,\theta,z,t)$ over the entire cross section, and divide by $S(z)$, where $S(z)$ is the local cross section. We normalize $\bar{C}(z,t)$ to $\max(\bar{C})$ of all the experiments performed. We recall that if $\bar{C}$ converges to a normal distribution, the time derivative of its variance may be used to calculate an enhanced diffusion constant $D_{\mathrm{exp}}$ (see equation 3.9), which can be compared to the 1D enhanced diffusion theory described in section 3.4. Before the dye will achieve a normal distribution, the injection must be finished, and the dye should not be influenced by steady streaming such as discussed in sections 12.4 and 12.6

### 12.7.1 Qualitative Observations

In figure 12.12 we compare $\bar{C}(z,t)$ for a bolus injected with the standard metal catheter (i.e. with the injection ports at $z = -12$ mm) to $\bar{C}(z,t)$ for the same bolus injected with the silicone catheter. We observe that $\bar{C}(z > 0)$ is substantially increased for the metal catheter compared to the Medtronic catheter. The opposite is true for $\bar{C}(z < 0)$. The total axial spread is comparable between the two cases. Although it seems that the ideal metal catheter is slightly more efficient in promoting positive axial spread, this is probably due to the limited sensitivity of the system.

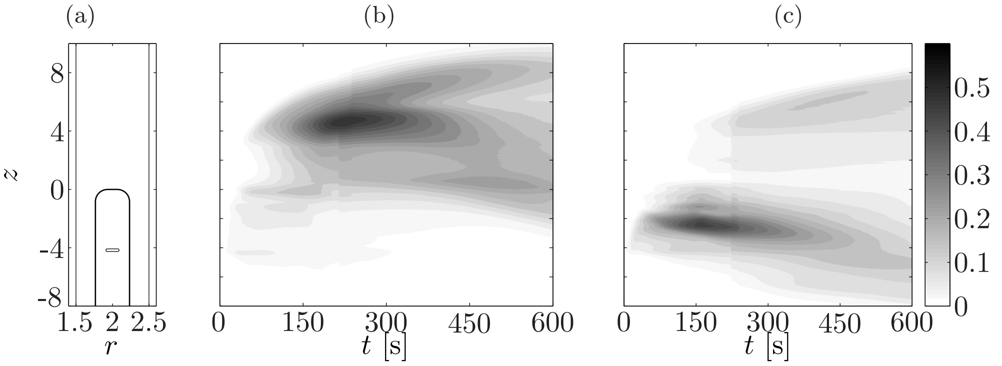

**Figure 12.12:** $\bar{C}(z,t)$ for an injection of a $V_B = 60$ $\mu$l and $Q_{\text{inj}} = 0.45$ $\mu$l/s injected with (b) the metal catheter and (c) the Medtronic catheter into a constant cross section annular gap. The oscillation parameters were $f_{\text{osc}} = 1.5$ Hz, and $A_{\text{osc}} = 2.62$. The values are normalized to the maximum $\bar{C}$ measured during all experiments that were performed using the same bolus volume and concentration.

Using the same injection and oscillation parameters, we investigate $\bar{C}$ in several annular gaps with slowly varying sections. The results are shown in figures 12.13–12.15. Several errors related to the optical setup influence the measurements. For example in 12.13(a) the apparent absence of dye in a band at $z \approx 6$ is caused by an O-ring in the field of view of the camera that is used in the assembly of the varying cross section geometry. A decrease in the signal at $z \approx 2$, amongst others, in the same figure is caused by a step increase of the outer diameter of the outer cylinder used to make the annular gap. Furthermore, as mentioned in section 11.6 we increased the laser power during a run to increase the dynamic range of our LIF measurements. For these experiments we increased the laser power after $t = 240$ seconds. Because some heavily diluted dye is brought above the signal to noise ratio, a discontinuity appears at $\bar{C}(z, t = 240)$. These limitations complicate a quantitative analysis of the results. We eliminate the influence of non-controllable catheter inclination and movement by showing only results for the straighter metal catheter. Although the color scales used in figures 12.13(c)-12.15 are different from the one in figure 12.12, the lowest shown contour is at the same level so that the spread can be compared.

### 12.7.2 Influence of Characteristic Length $L$ and Catheter Position

First, we look at the influence of a constricted geometry with $\epsilon = 0.056$ (#1) and $\epsilon = 0.019$ (#2) and the position of the catheter on the axial dispersion in figure 12.13. We may observe in figure 12.13(a) that the axial spread pattern is similar to that of the dye injected into the constant cross section geometry, however convective transport increases the rate at which the envelope travels upwards. Less dye reaches $z > 0$, which is easily explained by the position of the injection port, which is below the midpoint of the varying cross section. Dye in the lower part of the varying cross section will be entrained into another recirculation cell. Figure 12.13(b) shows the effect of lowering the catheter tip to below the midpoint of the varying cross section. A substantial part of the dye still travels above the midpoint, aided by the combined action of the catheter and varying cross section related steady streaming. The effect of changing the slope of the constricted geometry is shown in figure 12.13(c). Compared to previous cases, the dye is more quickly diluted, and reaches the top of the experimental axis quickest. Although we know that the typical steady streaming velocities are lower compared to previous cases (constant cross section or lower $L$), they are extend over 3 times the range. This important result implies that minor variations in the subarachnoid space over a long distance will likely determine the total distance a dye can travel before it is absorbed by the spinal cord.

### 12.7.3 Influence of the amplitude of the varying cross section $\Delta r_o$

We increase the value of $\epsilon$ in the expanded geometry by increasing the outer radius of the varying cross section, rather than decreasing $L$. We investigate the effect of the same bolus as in the constricted geometry on $\bar{C}(z,t)$ in two different geometries in figure 12.14. We observe that the axial spread between the two cases is relatively similar. The maximum in dye concentration is clearly linked to the catheter tip, rather than to the expanded cross section. We observe a slight increase in the axial spread above and below the varying cross section which might indicate that the assumption of a slowly varying cross section is no longer strictly applicable, in fact $\mathrm{Re}_{\mathrm{s}}\epsilon = 27 \gg 1$. Therefore, similar to the catheter related steady streaming, this would likely create recirculation zones above and below the actual varying cross section. The larger steady streaming velocities for larger $\epsilon$ also contribute by enhancing diffusion.

To model regular variations of the subarachnoid space related to the vertebral body structure of the spine (see figure 3.1), we explore the influence of several expanded sections stacked on top of each other, geometry $\epsilon = 0.112$ (#5). The result is shown in figure 12.15. The dye travels in both directions, with the majority being affected by the steady streaming at the catheter tip. Although it concerns an expanded cross section, this is qualitatively similar to the results of the constricted varying cross section shown in figure 12.13(b). This is due to the similarity in catheter tip position with respect to the cross section. In fact, we only observe the dye at $z > 4$ after $t = 240$ s, the moment we switched to a higher laser intensity. The delay in axial transport at $z = 4$ might be related to the step in concentration seen in figure 12.11(b)-12.11(e), thereby representing the time required for the dye to enter the boundary layer before it can cross over to the adjacent recirculation cell.

### 12.7.4 Measured Diffusion Coefficient $D_{\mathrm{exp}}$

In this section we aim to characterize the dispersion by calculating an enhanced diffusion coefficient. Several phenomena complicate this procedure. From the previous section it is obvious that the dye is often not normally distributed on the axis, thereby complicating

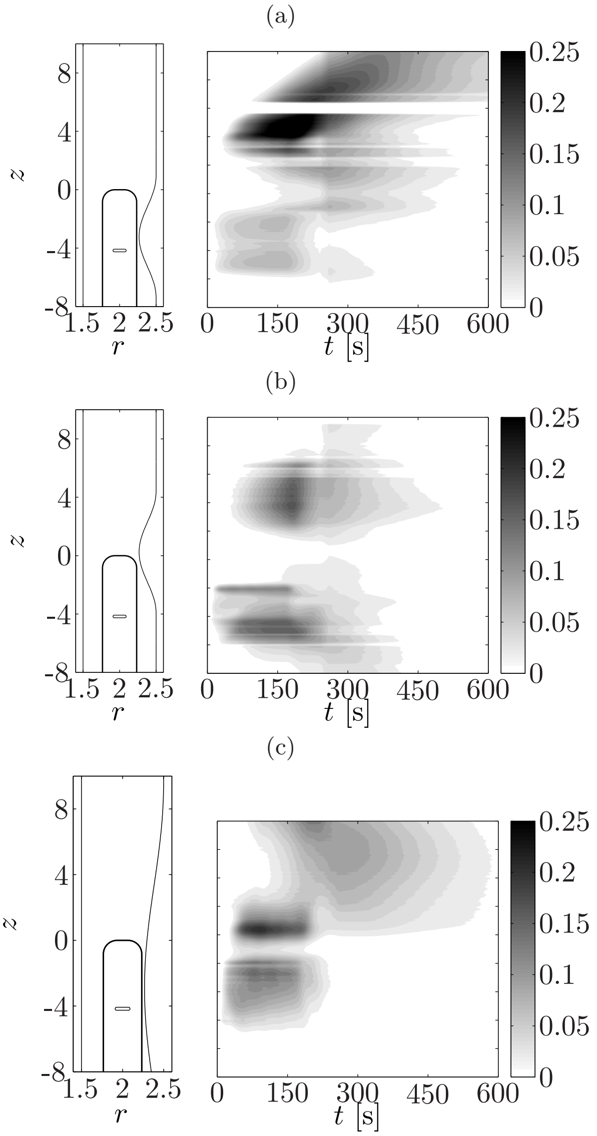

**Figure 12.13:** $\bar{C}(z,t)$ for a $V_B = 60$ $\mu$l and $Q_{\text{inj}} = 0.45$ $\mu$l/s bolus, injected with the metal catheter into a constricted cross section annular gap with (a),(b) $\epsilon = 0.056$ (#1), and (c) $\epsilon = 0.019$ (#2).

the use of using equation 3.14 to derive an enhanced mixing coefficient. The dye is also observed to leave our limited height CV during an experiment. Furthermore, the 3D dispersion quickly dilutes the dye so that the concentration can fall below the detection threshold of our system (see section 11.5.4). In figure 12.16 we investigate the effect of the limited height of our CV and the detection threshold on measuring the variance $\sigma^2$. For this, we assume a normal distribution defined by the solution of the 1D diffusion equation given in equation 3.4. We observe that the measured variance is underestimated when the distribution falls beyond the CV, or is too diluted to be detected. Finally, the concept of an enhanced mixing coefficient in zones of steady streaming is questionable because the primary mode of dispersion is advection. We therefore calculate $\bar{C}$ using only the dye

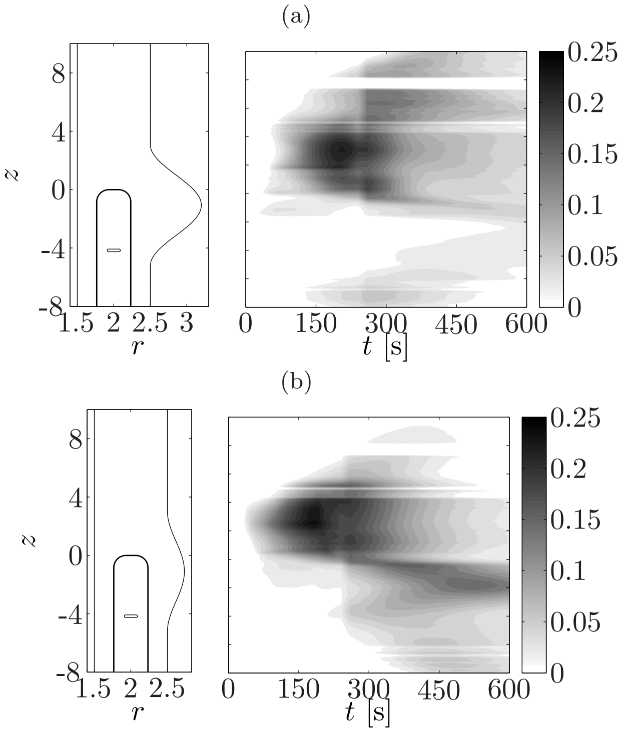

**Figure 12.14:** $\bar{C}(z,t)$ for a $V_B = 60$ $\mu$l and $Q_{\text{inj}} = 0.45$ $\mu$l/s bolus, injected with the metal catheter into an expanded annular gap geometry, with (a) $\epsilon = 0.168$ (#4), and (b) $\epsilon = 0.056$ (#3).

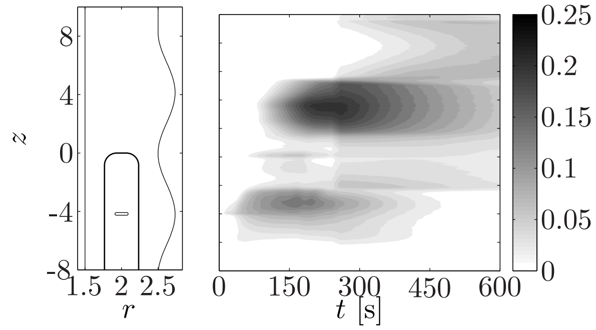

**Figure 12.15:** $\bar{C}(z,t)$ for a $V_B = 60$ $\mu$l and $Q_{\text{inj}} = 0.45$ $\mu$l/s bolus, injected with the metal catheter into a periodic varying cross section annular gap geometry with a characteristic $\epsilon = 0.112$ (#5).

found between $\pi/2 < \theta < 3\pi/2$, thereby largely ignoring mixing due to steady streaming. Unfortunately, because of increased axial dispersion (see figure 12.8) there is not enough dye found in this area when using the $\epsilon$ geometries. We therefore limit ourselves to the 64 experiments performed in the straight annular gap.

As shown in figure 12.17(a), using three typical measurements, the experimental $\sigma(t)^2$ is linear at first but can be reduced to zero when the dye is no longer detected. This is in line with the theoretical prediction shown in figure 12.16, but happens on a shorter time scale. Figure 12.17(b) shows that, when averaged over all the experiments, the obtained

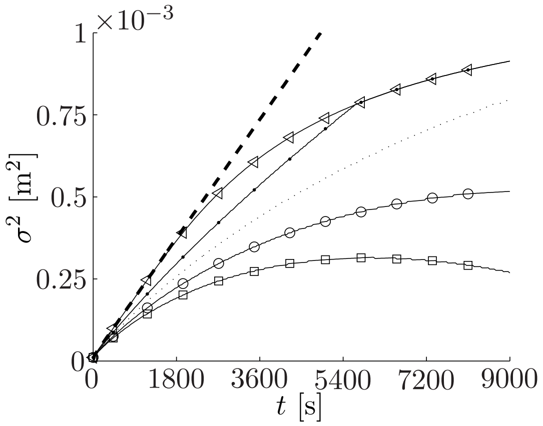

**Figure 12.16:** The theoretical variance $\sigma^2$ for 1D axial diffusion in a limited size ($L = 6$ cm) CV and a detection threshold of 0% (◁), 3% (·), 5% (dotted line), 7% (○), and 9% (□). The initial dye distribution is given by $\bar{C}(z \le 0.1, 0) = 1$ and $\bar{C}(z > 0.1, 0) = 0$, with $z$ normalized to $L$, and $D_{\text{enh}} = 150D$. The dashed line indicates the variance in a CV with $L \to \infty$ and a threshold of 0.

$D_{\text{exp}}$ is of the same order magnitude as the theoretical values, however, the variation on our calculated diffusion coefficient is high. The average $D_{\text{exp}}$ is too high, contrary to what should be expected for a limited sensitivity system. This discrepancy is related to the rate at which the dye enters the modified CV ($\pi/2 < \theta < 3\pi/2$), which is in turn dependent on the steady streaming induced by the catheter. Also 3D (azimuthal) diffusion will be enhanced because of the larger surface area of the dye. We think that the linear trend shown in the figure 12.17(b) represents the increasing importance of the detection threshold on the calculation of $\sigma^2$ at higher diffusion rates. Finally, $D_{\text{enh}} = D_{\text{enh}}(t)$, so we should have averaged the time derivative of the variance over one oscillation cycle. This can also contribute to a high $D_{\text{exp}}$ compared to theory.. Although the 1D enhanced mixing model is an easy way to characterize the added dispersion, its application is rather limited in our system. The 3D aspect of the diffusion, the non-normal axial distribution of the dye, and the influence of several steady streaming sources (i.e. the catheter and $S(z)$) all complicate a more quantitative analysis of the phenomena.

## 12.8 The Dye's Envelope

A threshold was used to identify the axial envelope of the dye based on $\bar{C}(z, t)$. We use the 1D-diffusion equation, using the same parameters as in figure 12.22, to investigate the effect of using a threshold to detect the envelope of the dye. The results are shown in figure 12.18. As can be observed, there are two main problems when using the threshold to detect the envelope, either the threshold falls outside the CV, or the envelope reduces in size as the concentration diminishes to below the detection threshold. Similar to section 12.9, 3D dispersion is expected to increase this phenomenon as diffusion is increasingly important. Due to this phenomenon, we solely use the envelope to investigate the initial advection of the scalar, when the effect of diffusion in limited. Use of the 50% threshold is not possible because of the non-normal distribution of the dye. We show two examples of the way the envelope was calculated in figure 12.19.

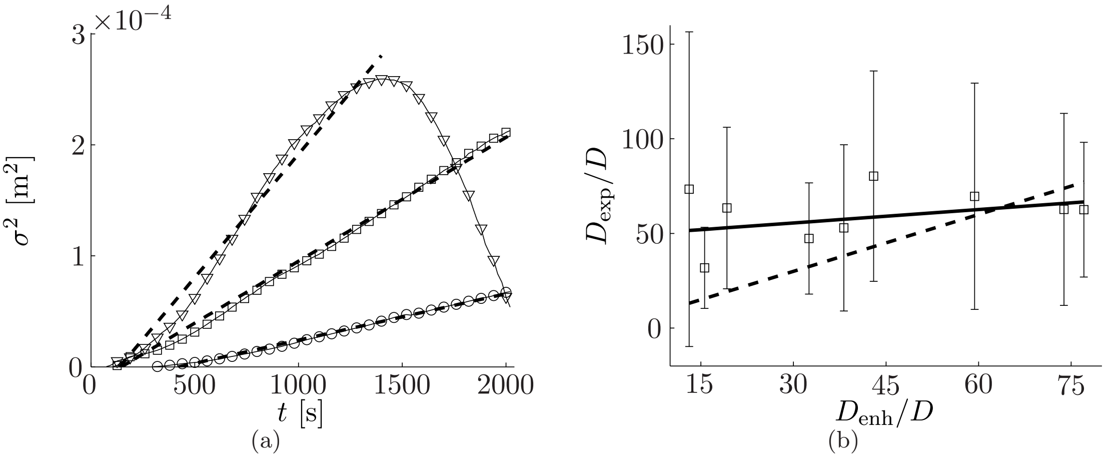

(a) (b)

**Figure 12.17:** (a) shows 3 arbitrary examples of the measured variance vs. t inside the constant cross section annular gap obtained with the metal catheter. The initial signal is fitted with a first order polynomial (dashed line) of which the slope is used to calculate the enhanced diffusion coefficient $D_{\text{exp}}$. (b) shows the calculated $D_{\text{exp}}$ as a function $D_{\text{enh}}$, both are normalized with the molecular diffusion coefficient $D$ of fluorescein. The □ indicates the mean measured value, while the error bars indicate the standard deviation [-] of the measurements. The dashed line indicates $D_{\text{exp}} = D_{\text{enh}}$, while the solid line is a linear fit on $D_{\text{exp}}$ showing the trend.

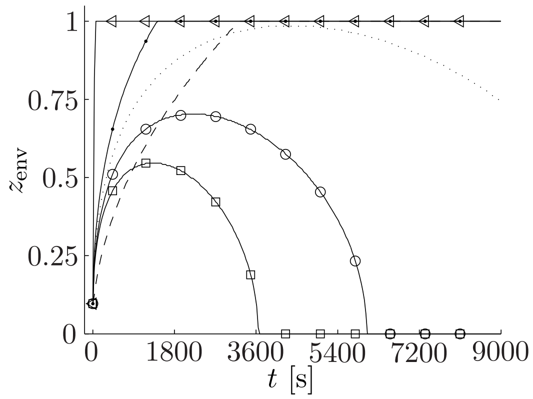

**Figure 12.18:** The envelope of the dye subject to 1D axial diffusion in a limited size CV as defined using a threshold of 0 (◁), 3% (·), 5% (−−), 7% (○), and 9% (□). The dashed line indicates the envelope when calculated with 50% threshold. Only the top half of the envelope is shown, and $z$ was non-dimensionalized with the length $L = 6$ cm of the CV. The initial dye distribution is given by $m(z \leq 0.1, t = 0) = 1$ and $m_{\text{CV}}(z > 0.1, t = 0) = 0$ and $D_{\text{enh}} = 150D$ is an estimate based on the theoretical considerations shown in section 3.4.

### 12.8.1 Dispersion Above the Catheter Tip

First, we use the complete $(\forall\theta)$ axial profile $m_{\text{CV}}(z,t)$ to investigate the initial envelope propagation above the catheter tip, thought to be primarily influenced by steady streaming. Two parametric models shown in figure 12.20 are used to characterize the advection. The model, of moderate accuracy, that expresses the initial extent of the envelope is shown

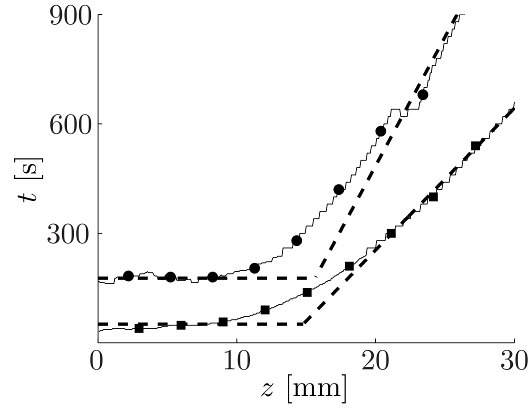

**Figure 12.19:** Two typical dye boundary curves as determined using the detection limit of the setup as a threshold on the axial concentration. Two weighted linear fits were calculated and identify the initial extent of the envelope, and provide a rough estimate of the subsequent growth rate of the envelope. The arbitrarily chosen curves were the results of a $Vb = 60$ $\mu$l injection with the metal catheter at $\varphi = 0$, and (■) $Q_{\text{inj}} = 0.4$ $\mu$l/s, $A_{\text{osc}} = 1.74$, $f_{\text{osc}} = 2$ Hz, and (●) $Q_{\text{inj}} = 0.04$ $\mu$l/s, $A_{\text{osc}} = 1.74$, $f_{\text{osc}} = 2$ Hz.

in figure 12.20(a). As we have observed qualitatively in the beginning of this chapter, the initial extent is ∼15 mm. This model only includes a single linear term of $A_{\text{osc}}$. A higher $A_{\text{osc}}$ leads to a higher initial extent of the envelope. Although it should be a quadratic effect, this is probably related to the characteristic streaming velocity.

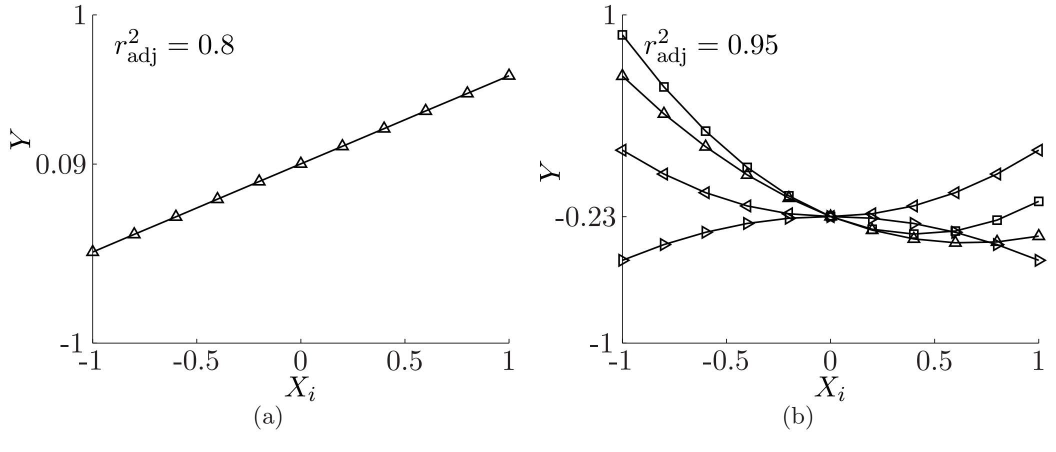

(a)

(b)

**Figure 12.20:** The parametric model for (a) the initial extent, or distance above the catheter tip that the dye reaches nearly instantly after reaching the catheter tip itself ($\Delta\hat{Y} = 18$ mm, and $\hat{Y}_{\text{ref}} = 16.4$ mm), and figure (b) the time it takes the dye to travel 14 mm above the catheter tip ($\Delta\hat{Y} = 1111$ s, and $\hat{Y}_{\text{ref}} = 228$ s). The factors included in the model are: $A_{\text{osc}}$ (△), $Q_{\text{inj}}$ (□), $A_{\text{osc}}f_{\text{osc}}$ (◁), $f_{\text{osc}}Q_{\text{inj}}$ (▷).

In nearly all the trials the dye reached at least a point $z = 14$ mm above the catheter tip. The time the dye took to reach this height is modeled in figure 12.20(b). Logically the largest effect is that of $Q_{\text{inj}}$. If dye is injected slowly it takes longer for a measurable quantity of the dye to reach a point above the catheter tip. This is consistent with the assumption that a high $\mathrm{Pe}_{\mathrm{inj}}$ will lead to higher concentrations further away from the injection site. $A_{\mathrm{osc}}$ is almost as important as $Q_{\mathrm{inj}}$. A higher $A_{\mathrm{osc}}$ leads to a more rapid dispersion, which is logical considering its influence in both steady streaming and enhanced mixing. The interaction term $A_{\mathrm{osc}} f_{\mathrm{osc}} \propto \mathrm{Re}$ is a term related to the intensity of the mixing, and delays the time for which a measurable quantity reaches the 14 mm mark. Although the relatively small interaction term $f_{\mathrm{osc}} Q_{\mathrm{inj}}$ increases the accuracy of the fit, we have no simple explanation for it.

### 12.8.2 Growth Rate of the Envelope

Finally, by calculating the axial profile $m_{\mathrm{CV}}(z,t)$ in the region $(\pi/2 < \theta < 3\pi/2)$ we investigate the growth rate of the envelope in the relative absence of steady streaming. This is similar to calculating $D_{\mathrm{exp}}$ in the same region as in section 12.5. The parametric model, shown in figure 12.21, fits the experimental results with $r^2_{\mathrm{adj}} = 0.97$. The model should therefore provide insight into the reasons why our prediction of $D_{\mathrm{enh}}$ is relatively high and predicts a slightly different trend. We note that the average growth rate of the envelope is small $\hat{Y}_{\mathrm{ref}} = 0.05$ mm/s. This confirms that the effect of increased axial dispersion through enhanced diffusion is small compared to that of steady streaming, which is of $O$(mm/s). The most important effect is that of $A^2_{\mathrm{osc}}$, which increases the growth rate of the envelope. Besides determining how fast the dye is transported into the CV, it is likely to be related to the functional dependence of $D_{\mathrm{enh}} \propto A^2_{\mathrm{osc}}$. We hypothesize that the interaction term of $A_{\mathrm{osc}} Q_{\mathrm{inj}}$ might be related to the amount of dye that is detected in the modified CV, as $Q_{\mathrm{inj}}$ and $A_{\mathrm{osc}}$ will both have a positive effect on the initial dispersion of the dye. The linear effect of $Q_{\mathrm{inj}}$ is thought to express the same phenomenon. This will be analyzed in subsequent sections. The final term in the model, $f_{\mathrm{osc}}$, also increases the growth rate of the envelope. It is logically related to enhanced mixing ($D_{\mathrm{enh}} \propto \sqrt{f_{\mathrm{osc}}}$), but could also indicate the rate at which dye enter the CV though steady streaming ($V_s \propto f_{\mathrm{osc}}$).

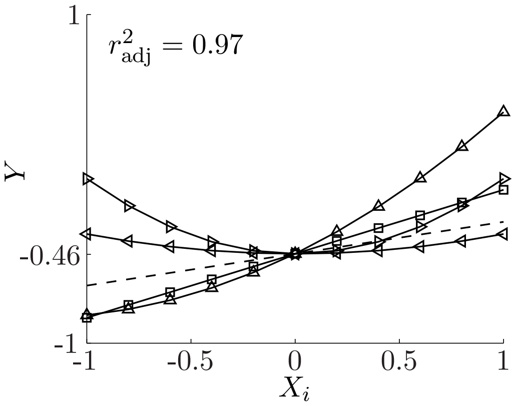

**Figure 12.21:** The parametric model for the average of the growth rate of the dye envelope based on the axial concentration away from the catheter $(\pi/2 < \theta < 3\pi/2)$, $(\Delta\hat{Y} = 0.20$ mm/s, and $\hat{Y}_{\mathrm{ref}} = 0.05$ mm/s). The factors included in the model are: $f_{\mathrm{osc}}$ (−−), $A_{\mathrm{osc}}$ (△), $Q_{\mathrm{inj}}$ (□), $A_{\mathrm{osc}} f_{\mathrm{osc}}$ (◁), $A_{\mathrm{osc}} Q_{\mathrm{inj}}$ (▷).

## 12.9 Total Measured Mass in the Control Volume $m_{\mathrm{CV}}$

As we have proposed in section 12.3.2, the total mass in the control volume is a convenient measure of spread. We therefore analyze typical $m_{\mathrm{CV}}$ vs. $t$ curves to obtain specific information on how $A_{\mathrm{osc}}$, $f_{\mathrm{osc}}$, $Q_{\mathrm{inj}}$, and $\epsilon$ influence the total dispersion. By doing so, we neglect important interactions between the different factors, such as the catheter and its orientation $\varphi$. The second part of this section therefore discusses parametric models for specific characteristics of the $m_{\mathrm{CV}}(t)$, namely $\max(m_{\mathrm{CV}})$, a linear fit on $\dot{m}_{\mathrm{CV}}(t < t_{\mathrm{inj}})$, and an exponential fit on $\dot{m}_{\mathrm{CV}}(t > t_{\mathrm{inj}})$, where $t_{\mathrm{inj}}$ is the time of injection. We first, however, characterize the influence of the limited sensitivity of our system on the measurement error.

### 12.9.1 The Influence of the Detection Threshold

We again use the solution of the 1D diffusion equation, equation 3.4 to examine the influence of the size of the CV and the detection threshold on the total mass measured in the CV as a function of time. The result is shown in figure 12.22. We observe that in the case of 1D diffusion, in similar conditions as our experiment, at best 42% of the dye can be detected after 4 hours due to the limited size of the CV. For thresholds of 9% no dye can be detected after 1 hr. Obviously, the 3D dispersion observed in the experiment will further increase the negative role of the detection threshold, as more dye inside the CV will be below the detection threshold.

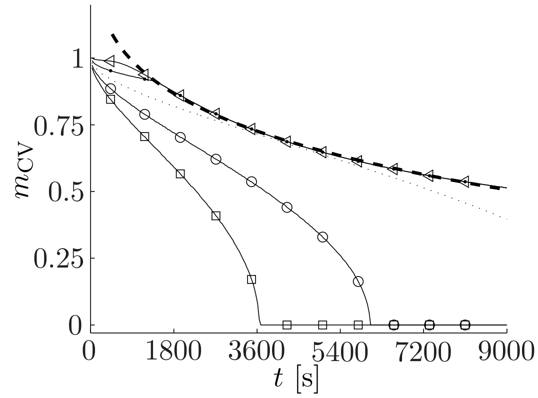

**Figure 12.22:** The computed theoretical $m_{\mathrm{CV}}$ for 1D axial diffusion in a limited size ($L = 6$ cm) CV and a detection threshold of 0% (◁), 3% (·), 5% (dotted line), 7% (○), and 9% (□). The initial dye distribution is given by $m(z \leq 0.6\ \mathrm{cm}, t = 0) = 1$ and $m_{\mathrm{CV}}(z > 0.6\ \mathrm{cm}, t = 0) = 0$ and $D_{\mathrm{enh}} = 150D$. The upper bound is obtained when the detection limit is lower than the lowest concentration inside the CV and can be approximated using power law (dashed line).

### 12.9.2 Primary Effect of $A_{\mathrm{osc}}$ on $m_{\mathrm{CV}}$

Figure 12.23 shows that amplitude of oscillation $A_{\mathrm{osc}}$ is an important parameter in determining the spread of the injected bolus, whether inside a constant cross section geometry, or in a varying cross section annular gap. The maximum of $m_{\mathrm{CV}}$ decreases as $A_{\mathrm{osc}}$ increases. This indicates a higher spread or diffusion. This effect of the amplitude is more

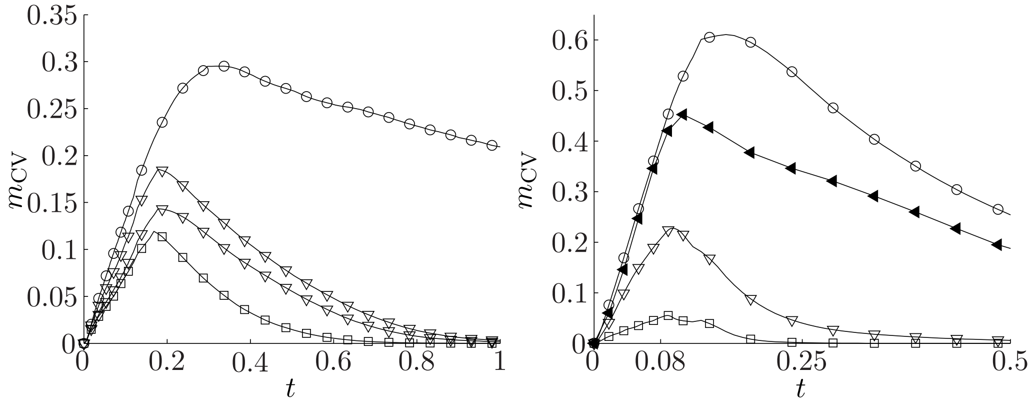

(a) (b)

**Figure 12.23:** The influence of $A_{\mathrm{osc}}$ on $m_{\mathrm{CV}}$ as a function of time $t = \hat{t}/\max(\hat{t})$ during and after the injection of a $V_B = 60$ $\mu$l into (a) the constant cross section geometry with the silicone catheter at $Q_{\mathrm{inj}} = 0.22$ $\mu$l/s, compared to (b) into the constricted cross section with $\epsilon = 0.056$ (#1) with the ideal metal catheter at $Q_{\mathrm{inj}} = 0.4$ $\mu$l/s. The oscillation amplitude is $A_{\mathrm{osc}}$ of 1.49 (○), 2.62 (▽), and 3.74 (□), with $f_{\mathrm{osc}} = 1.5$ Hz. The ◀ in (b) is a reference measurement in the constant cross section geometry with the same oscillation parameters as ▽.

pronounced in the varying cross section annular gap. By comparing the two curves with the same oscillation parameters in figure 12.23(b), we observe that the spread inside the varying cross section annular gap is considerably higher than in the constant cross section geometry. These results are unsurprising given that both $D_{\mathrm{enh}} \propto A_{\mathrm{osc}}^2$, and $V_s \propto A_{\mathrm{osc}}^2$. Steady streaming is quick to whisk the scalar away from the catheter, and enhanced diffusion will further increase the axial spread. We note that it is difficult to compare the amplitudes of $m_{\mathrm{CV}}$ between the two figures because the injection rates and catheters are not the same.

### 12.9.3 Primary Influence of $f_{\mathrm{osc}}$ on $m_{\mathrm{CV}}$

Figure 12.24 shows the influence of changing the frequency $f_{\mathrm{osc}}$ in a constant or varying cross section annular gap. The difference between the curves is small. In the constant cross section annular gap, the $m_{\mathrm{CV}}$ increases as $f_{\mathrm{osc}}$ decreases thereby indicating poorer spread. The intermediate frequency curve is, however, very similar to the highest frequency curve. This is surprising because from the theory of enhanced mixing $D_{\mathrm{enh}} \propto \sqrt{f_{\mathrm{osc}}}$, and steady streaming $V_s \propto f$, the spread at higher frequency should be higher. This is in fact the case inside the varying cross section, but the difference is small. By direct comparison in figure 12.24 we observe that the spread is markedly higher in the varying cross section annular gap. We observe that this effect is considerably bigger than the influence of the frequency. Two explanations are put forward for the unexpected behavior found in figure 12.24(a). First, the silicone catheter position is not identical between experiments. A slightly different inclination could give rise to smaller local recirculation cells, albeit at higher $V_s$, which could limit spread. Secondly, and probably more important in this

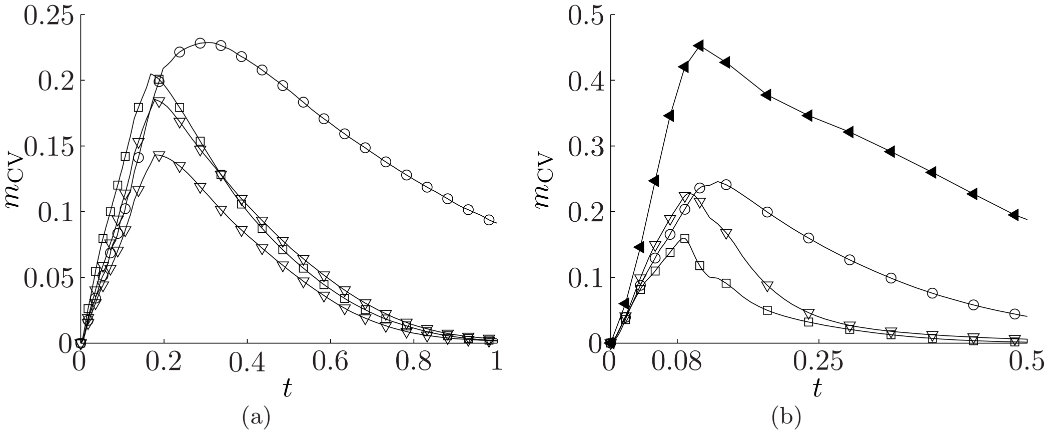

(a) (b)

**Figure 12.24:** The influence of $f_{\text{osc}}$ on $m_{\text{CV}}(t)$, where $t = \hat{t}/\max(\hat{t})$, during and after the injection of $V_B = 60$ $\mu$l into (a) the constant cross section geometry with the silicone catheter with $Q_{\text{inj}} = 0.22$ $\mu$l/s, compared to (b) into the constricted cross section with $\epsilon = 0.056$ (#1) with the ideal metal catheter and $Q_{\text{inj}} = 0.4$ $\mu$l/s. The oscillation frequency is $f_{\text{osc}} = 0.86$ (○), 1.5 (▽), and 2.15 (□) Hz, and the $A_{\text{osc}} = 2.62$. The ◀ is a reference measurement in the constant cross section geometry with the same oscillation parameters as ▽

specific case, the lower $m_{\text{CV}}$ can also simply indicate a higher error $\varepsilon$.

### 12.9.4 Primary Influence of $Q_{\text{inj}}$ on $m_{\text{CV}}$

Figure 12.25 shows the influence of the injection rate. At any time during the experiments the total mass $m_{\text{CV}}$ in the CV is much lower for lower injection speeds. After the injection of the bolus $m_{\text{CV}}(t \approx 1)$ reaches a peak. This expresses the importance of $\text{Pe}_{\text{inj}}$ which indicates that diffusion – and the related error $\varepsilon$ – is more important for lower injection rates. In other words, the scalar remains relatively concentrated, and more easily measurable, over longer distances for higher injection rates. One would also expect a high $m_{\text{out}}$ for higher injection rates, because the entire scalar volume is subject to axial spread favoring forces for a longer time compared to lower rate bolus injections.

### 12.9.5 Primary Influence of $\epsilon$ on $m_{\text{CV}}$

We first explore the influence of the slope of the varying cross section, $\epsilon$, on $m_{\text{CV}}$ by changing the length $L$ of the constricted varying cross section for high and low injection rates, figure 12.26. We find that the spread is higher for the geometry with the lower $\epsilon$, but higher $L$. Although the transport of the dye might be slower in the geometry with higher $L$, this is compensated by the physical size of the recirculation cells. This behavior is therefore consistent with the observations made in section 12.7.

We further explore the influence of $\epsilon$ on $m_{\text{CV}}$ by changing the $\Delta r_o$ of the expanded varying cross section for high and low injection rates in figure 12.27. We observe that the spread is increased for higher $\epsilon$. Because in this case the heights of the varying cross sections are the same, the higher characteristic steady streaming velocity is likely to be responsible for this effect. Caution is required, however, because the shaded area where

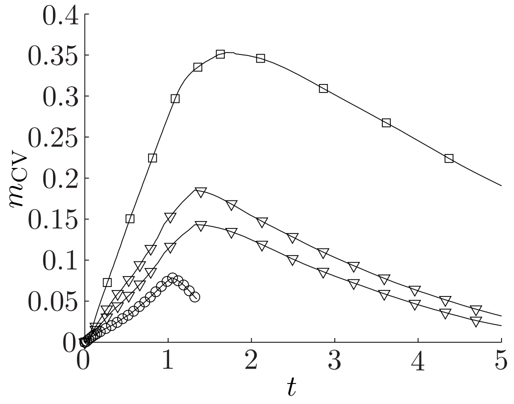

**Figure 12.25:** The total mass in the CV, $m_{\mathrm{CV}}$, as a function of time $t = \hat{t}/t_{\mathrm{inj}}$ for an injection rate $Q_{\mathrm{inj}}$ of 0.04 (–), 0.22 (▽), and 0.45 $\mu$l/s (□). Catheter type - Medtronic, $\varphi = 0$, $f_{\mathrm{osc}} = 1.5$ Hz, $A_{\mathrm{osc}} = 2.62$, and $V_B = 60$ $\mu$l.

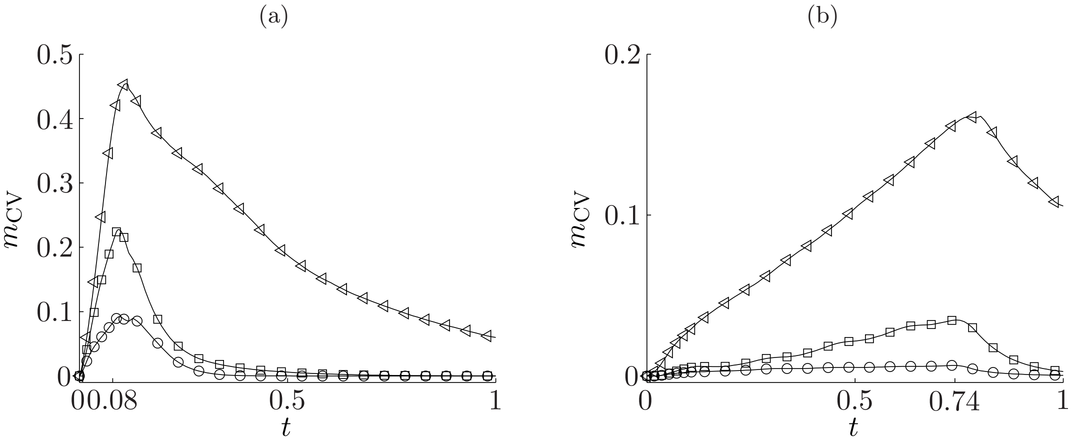

**Figure 12.26:** The influence of the constricted axi-symmetric varying cross section with $\epsilon = 0.056$ (#1, □), $\epsilon = 0.019$ (#2, ○), on $m_{\mathrm{CV}}$. The ◁ marker line is a reference experiment in the constant cross section annular gap. Figure (a) is the result of a fast $Q_{\mathrm{inj}} = 0.4$ $\mu$l/s injection while (b) was a slow $Q_{\mathrm{inj}} = 0.04$ $\mu$l/s injection. The oscillation parameters were $f_{\mathrm{osc}} = 1.5$ Hz, and $A_{\mathrm{osc}} = 2.62$ for all plots.

we cannot measure the dye concentration also increases with the amplitude of the varying cross section. This will erroneously amplify the considered effect.

We calculated the maximum of $m_{\mathrm{CV}}$ for all the experiments performed with varying cross section geometry and a reference set of measurements with a constant cross section annular gap. Each configuration (6 in total) is characterized with 7 measurements with different $A_{\mathrm{osc}}$, $f_{\mathrm{osc}}$, and $Q_{\mathrm{inj}}$. We calculate the mean of all data with the same characteristic height $L$, making no distinction between the constricted, expanded, or stacked geometries, or the amplitude of the varying cross section. The results are shown in figure 12.28. The bars indicate the standard deviation of the set population. As expected, the total mass is significantly lower in the varying cross section geometries, and lowest for $L = 75$ mm.

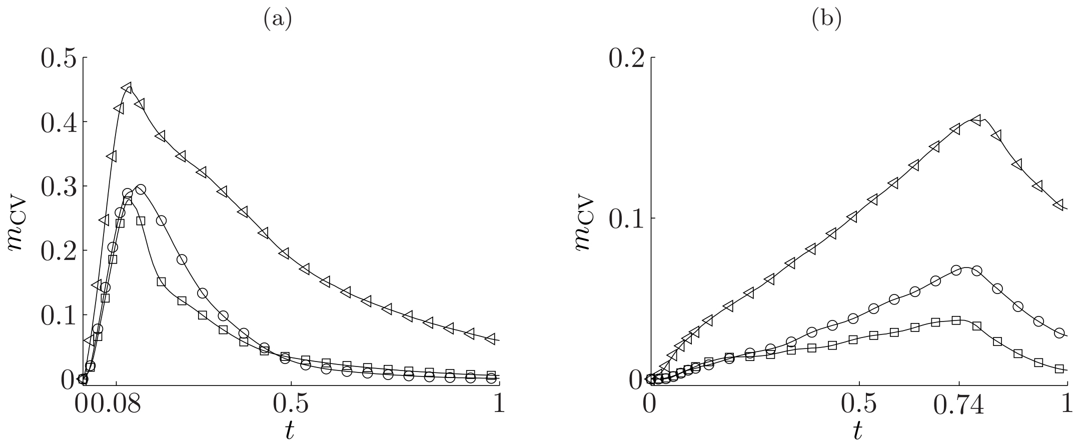

**Figure 12.27:** The influence of the expanded axi-symmetric varying cross section with $\epsilon = 0.168$ (#3, $\square$), $\epsilon = 0.056$ (#4, $\circ$), on $m_{\mathrm{CV}}$. The $\triangleleft$ marker line is a reference experiment in the constant cross section annular gap. Figure (a) is the result of a fast $Q_{\mathrm{inj}} = 0.4$ $\mu$l/s injection while (b) was a slow $Q_{\mathrm{inj}} = 0.04$ $\mu$l/s injection. The oscillation parameters are the same as figure 12.26, namely $f_{\mathrm{osc}} = 1.5$ Hz, and $A_{\mathrm{osc}} = 2.62$ for all plots.

Although figure 12.27 implies that a similar relation should exist for the amplitude of the varying cross section, this could not be confirmed because the effect is small compared with the range of $m_{\mathrm{CV}}$ for the amplitudes, frequencies and injection speeds taken into account. More measurements are therefore required, specifically taking into account the systematic error induced by the shaded zone.

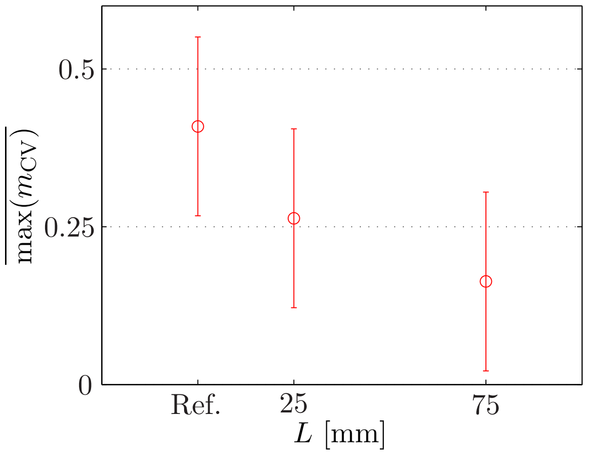

**Figure 12.28:** The average maximum mass in the CV vs. the characteristic length of the varying cross section $L$. The reference set (Ref.) was calculated over a set of the same set of experiments ($A_{\mathrm{osc}}$, $f_{\mathrm{osc}}$, and $Q_{\mathrm{inj}}$) with the same metal catheter and $\varphi$ in the constant cross section geometry. Results are statistically significant (p=0.012).

### 12.9.6 The Maximum of $m_{\mathrm{CV}}$

A distinct maximum of $m_{\mathrm{CV}}(t)$ is usually found at the end of the injection or with a small time lag. We have never measured $\max m_{\mathrm{CV}} > 0.75$, which can be explained due to the attenuation of the laser beam. One will recall that the relative error due to approximation can initially be as much as $\varepsilon_a \approx 35\%$. The average $\max(m_{\mathrm{CV}}) = 0.29$, indicating a considerably larger error. This is due to the dye leaving the CV and not attenuation, and therefore justifies our decision not to compensate for the attenuation. In spite of this error, $\max(m_{\mathrm{CV}})$ primarily indicates how much of the dye has left the CV, or how much is too diluted to be detected. The maximum of the measured mass can be delayed to after the $t_{\mathrm{inj}}$, and we hypothesize that this is due to dye coming into view of the camera from behind the catheter, or by an increase in signal due to diminished laser attenuation at lower concentrations. Figure 12.29(a) shows relevant information on the calculated parametric model. It predicts that a higher $Q_{\mathrm{inj}}$ will increase $\max(m_{\mathrm{CV}})$, or equivalently (using the same CV) a higher concentration. Logically, $A_{\mathrm{osc}}$ reduces the $\max(m_{\mathrm{CV}})$ because it increases the typical steady streaming velocities and the enhanced diffusion. The model predicts that the $f_{\mathrm{osc}}$ can either positively ($f_{\mathrm{osc}} \propto X_i \approx 0.3$), or negatively ($f_{\mathrm{osc}} \propto X_i \approx \pm 1$) influence the spread. This trend, or in fact the size of the effect compared to $A_{\mathrm{osc}}$, cannot be explained based on enhanced diffusion of steady streaming theories that predict an increased dispersion for increasing $f_{\mathrm{osc}}$. Given the relatively poor prediction at $X_i \to 1$ and the relatively poor $r^2_{\mathrm{adj}} = 0.81$, this model should therefore be treated with some care.

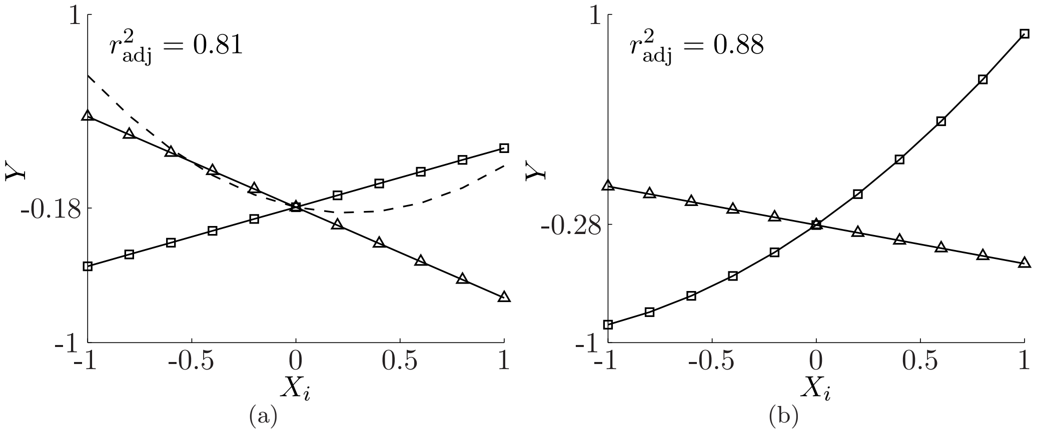

(a) (b)

**Figure 12.29:** The parametric models for (a) the $\max(m_{\mathrm{CV}})$, ($\Delta\hat{Y} = 0.75$, and $\hat{Y}_{\mathrm{ref}} = 0.28$) and (b) the slope of the linear fit on $m_{\mathrm{CV}}(t \leqslant t_{\mathrm{inj}})$ ($\Delta\hat{Y} = 0.23\ \mathrm{min}^{-1}$, and $\hat{Y}_{\mathrm{ref}} = 0.06\ \mathrm{min}^{-1}$). The factors included in the model are $f_{\mathrm{osc}}$ (−−), $A_{\mathrm{osc}}$ (△), and $Q_{\mathrm{inj}}$ (□).

### 12.9.7 Factors Influencing $\dot{m}_{\mathrm{CV}}$ During Injection

We calculate $\dot{m}_{\mathrm{CV}}$ by fitting a linear equation on $m_{\mathrm{CV}}(t \leqslant t_{\mathrm{inj}})$. This should provide a similar measure as the maximum $m_{\mathrm{CV}}$ presented in the previous section. The relevant information of the parametric model is shown in figure 12.29(b). As could be expected based on figure 12.25 the primary influence is that of $Q_{\text{inj}}$. Furthermore, the slope is lower for higher $A_{\text{osc}}$, indicating the effect of enhanced mixing and steady streaming. The model includes a term $Q_{\text{inj}}^2$ which might express the limited influence of diffusion at lower time scales representative for large $Q_{\text{inj}}$.

### 12.9.8 The Decay of $m_{\text{CV}}$ after Injection

We investigate whether the spread of the drug can be influenced by increasing $Q_{\text{inj}}$ by examining the decay of $m_{\text{CV}}(t > t_{\text{max}})$, where $t_{\text{max}}$ is the time at which $\max(m_{\text{CV}})$ is measured. We note that there no is no source term $\dot{m}_{\text{inj}}$. As observed in previous sections, a substantial quantity of dye can leave the CV due to advection. Furthermore, the dispersion is 3D. It is therefore impossible to identify a theoretical function that will systematically fit onto $m_{\text{CV}}(t > t_{max})$. Instead we simply fitted a decaying exponential of the form $m_{\text{CV}}(t > t_{max}) = a\mathrm{e}^{\beta t}$ on all $m_{\text{CV}}(t > t_{max}) > 0.01$. With a typical $r^2 > 0.99$ the fit was surprisingly accurate. A lower $\beta$ corresponds to a quicker dispersion of the dye. The parametric model is shown in figure 12.30. The primary effect on $\beta$ is $A_{\text{osc}}^2$, increasing the dispersion. A higher $f_{\text{osc}}$ also marginally increases the dispersion. These observations show the influence of $D_{\text{enh}} \propto \alpha A_{\text{osc}}^2$ and the characteristic steady streaming velocity $V_s \propto \alpha^2 A_{\text{osc}}^2$.

The model includes an increased dispersion for high and low $Q_{\text{inj}}$. This is probably related to the influence of $Q_{\text{inj}}$ on the initial dye distribution. A fast injection helps to distribute the dye over a larger surface, enhancing the dispersion afterwards. For a slow injection, diffusion increase the surface area. Based on this model the rate of decay is the same for very high ($Q_{\text{inj}} = 0.4$ $\mu$l/s) or low ($Q_{\text{inj}} = 0.04$ $\mu$l/s) injection rates. We conclude that increasing the injection rate by a tenfold does not dramatically increase the rate of decay after the injection has finished. We note that the model also includes an interaction term of $Q_{\text{inj}}$ and $f_{\text{osc}}$ for which we have no simple interpretation.

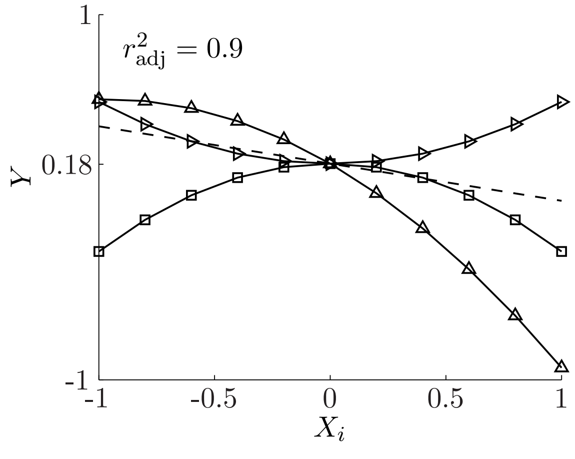

**Figure 12.30:** The parametric model for $\beta$ from the fit $m_{\text{CV}}(t > t_{max}) = a\mathrm{e}^{\beta t}$ ($\Delta\hat{Y} = 0.31$ min$^{-1}$, and $\hat{Y}_{\text{ref}} = -0.09$ min$^{-1}$), The curves indicate the relative importance of all the factors $-1 \leq X_i \leq 1$ that were included in the model, $A_{\text{osc}}$ ($\triangle$), $f_{\text{osc}}$ ($--$), $Q_{\text{inj}}$ ($\square$), and the interaction term $Q_{\text{inj}} f_{\text{osc}}$ ($\triangleright$).

## 12.10 Qualitative Observations Regarding Buoyancy

As introduced in section 3.7, the dispersion due to buoyancy is though to be dependent on the square of the Rayleigh number Ra. Influencing the dispersion through the addition of glucose is a common technique using in for example the epidural administration of local anesthetics. We qualitatively investigated the effect of buoyancy on the dispersion by adding glucose to the fluorescent dye in a limited number of experiments (16). Although water containing 0.3% (mass) glucose at 20°C is only 0.11% lighter than pure water at the same temperature, this is sufficient to dramatically alter the dye dispersion. For most realistic oscillation parameters, the dye quickly leaves the CV from beneath. This is shown in figures 12.31(a)–12.31(d) for a slowly injected $Q_{\text{inj}} = 2.4$ $\mu$l/s, $V_B = 60$ $\mu$l bolus at $f_{\text{osc}} = 1$ Hz, and $A_{\text{osc}} = 1.74$. Below the field of view of the camera we observed the breakup and full dispersion of the dye. Because only a fraction of the injected dye stays in the CV, our experimental setup is not well suited to quantify the dispersion. It is not illogical to assume, however, that the total dispersion is increased as the buoyancy will introduce secondary flow.

By independently doubling the Pe of the flow by doubling $A_{\text{osc}} = 3.49$ we can observe a radically different dispersion as shown in figures 12.31(e)–12.31(h). Contrary to before, the effect of buoyancy is less marked because a substantial portion of the dye remains in the CV. A substantial portion of the dye moves downwards after reaching the catheter, instead of being entrained by the steady streaming at the catheter tip. More dye leaves the CV from below compared to solutions without glucose, and more azimuthal spread is evident. Generally, the overall shape of the cloud is geometrically different and more dispersed than the mushroom shape that is observed for the plain solution of fluorescein. This is probably due to the interaction of the secondary flow induced by the buoyancy with the steady streaming. Buoyancy therefore seems successful in increasing the spread of the dye.

Figures 12.31(i)–12.31(l) show the results of a quick $Q_{\text{inj}} = 0.4$ $\mu$l/s injection using the $A_{\text{osc}} = 3.49$ and $f_{\text{osc}} = 1$ Hz. The dye remains much more concentrated compared to lower injection rates and almost instantly leaves the CV. We conclude that besides Ra, $\text{Pe}_{\text{inj}}$ is an important parameter to predict the site of action. For all cases, it seems that the concentration of the dye remains higher over a larger distance compared to plain fluorescein. The high concentration gradients manifest themselves until the buoyancy is diminished and the dye disperses in a cloud. These results suggest that if one were to consider using glucose to influence the spread only relatively low concentrations should be considered. If the buoyancy forces compared to the forces of steady streaming and enhanced mixing are too large, the injected solution could remain concentrated for too long making the site of action unpredictable, while it poses the risk of unacceptably high drug concentrations for a relatively long time period, especially near the injection ports and just below.

## 12.11 Summary of Experimental Observations

In this chapter we have presented a large number of qualitative and quantitative observations related to the dispersion of the dye. Where possible we have commented on the negative impact of our detection threshold on the $\sigma$, $m_{\text{CV}}$, and the dye's boundary detec-

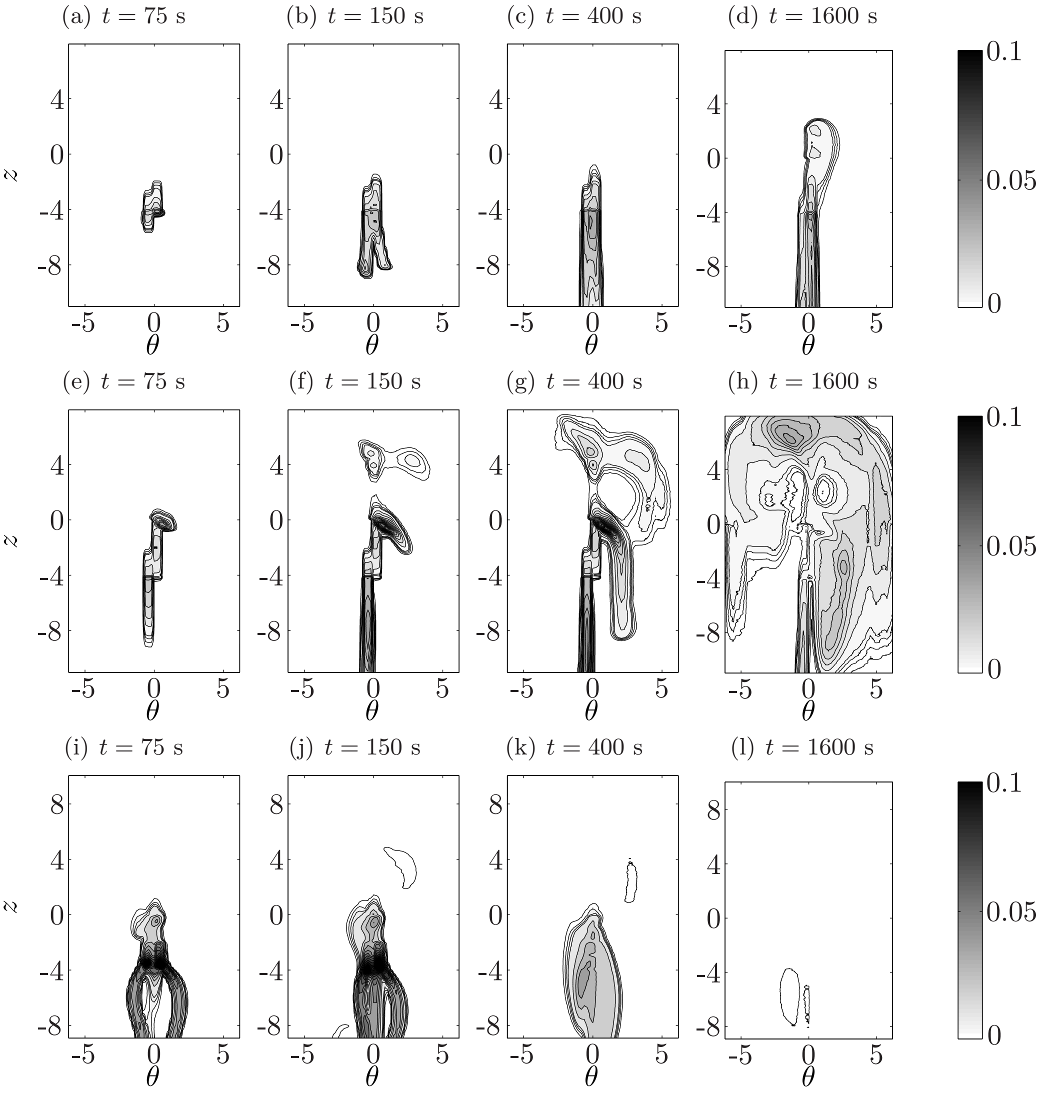

**Figure 12.31:** $(\theta, z)$-projection of a single 60 $V_B = 60\mu$l injected into the constant cross section geometry with the metallic ideal catheter with $f_{\text{osc}} = 1$ Hz, and $Q_{\text{inj}} = 0.04$ $\mu$l/s and $A_{\text{osc}} = 1.74$ (a) - (d), $Q_{\text{inj}} = 0.04$ $\mu$l/s and $A_{\text{osc}} = 3.49$ (e) - (h), and finally $Q_{\text{inj}} = 0.4\mu$l/s and $A_{\text{osc}} = 3.49$ (i) - (l).

| $\hat{Y}$ | Dim. | $\hat{Y}_{\text{ref}}$ | $\min(\hat{Y})$ | $\max(\hat{Y})$ | Figure |
|---|---|---|---|---|---|
| $\bar{z}_g$ | mm | -0.8 | -13.0 | 7.1 | 12.4(b) |
| Mean Top ratio | - | 0.55 | 0 | 1 | 12.5 |
| $\min(\Phi)$ | - | 0.79 | 0.01 | 0.99 | 12.7(a) |
| $\Phi(t = 1500)$ | - | 0.96 | 0.81 | 1 | 12.7(b) |
| Initial extent | mm | 16 | 6 | 24 | 12.20(a) |
| $t$ for $h = 14$ mm | s | 228 | 9 | 1120 | 12.20(b) |
| Growth rate | mm/s | 0.05 | 0.01 | 0.2 | 12.21 |
| $\max(m_{\text{CV}})$ | - | 0.28 | 0 | 0.75 | 12.29(a) |
| $\dot{m}_{\text{CV}}(t \leqslant t_{\text{inj}})$ | $\text{min}^{-1}$ | 0.06 | 0 | 0.23 | 12.29(b) |
| $\beta$ | $\text{min}^{-1}$ | -0.1 | -0.32 | -0.01 | 12.30 |

**Table 12.3:** The range of responses measured in the parametric models.

tion. We conclude that the high detection threshold and the relatively small height of our CV substantially limit the accuracy of the measurements. Furthermore, we have generally ignored the influence of attenuation on our measurements, the largest experimental error for determining $m_{\text{CV}}$. This is justified if one looks at the typical extent of the dye above the catheter tip, which is very near the top limit of our CV volume. Dye quickly leaves the CV, as is also expressed by the low maximum of the $m_{\text{CV}}$ curves, meaning that it is impossible to systematically correct for laser beam attenuation. These issues are more pertinent than, for example, optical aberrations for slowly varying cross sections, which should nonetheless also be addressed in future work. Due to these limitations and the limited number of experiments that could be performed, we have relied on parametric models and our interpretation of these models to characterize the dispersion process. The responses are summarized in table 12.3. The number of observations in an illustration of the complexity of the mixing phenomena and their interactions. Several observations, in particular the mean axial position of the cloud, indicate that the dispersion is symmetric around the catheter tip, which could explain why granulomas form here. Also, as is illustrated by for example the model for the growth rate of the envelope in the absence of steady streaming, enhanced diffusion is a relative slow process to increase the axial dispersion of the dye. In these parametric models we were not able to capture the influence of the catheter and it orientation $\varphi$, or the variables related to the varying cross section geometries.

In general, the dispersion is generally characterized by a mushroom shape cloud near the catheter tip. The azimuthal spread is symmetrical with respect to the symmetry plane. It is very limited near the catheter itself, even for high (but still clinically relevant) $Q_{\text{inj}}$ and optimal catheter orientation. A fast bolus injection does not dramatically increase the azimuthal spread. The basic mushroom shape can be marginally influenced by the orientation of the catheter, but more dramatically by the specific curvature and inclination of the catheter, slowly varying cross section geometry, and buoyancy.

The axial spread is primarily determined by the steady streaming, and to a lesser extent by the enhanced diffusion. The axial spread is generally non-normal. Slightly more dye seems to travel to the top for high $A_{\text{osc}}$, and high $A_{\text{osc}}Q_{\text{inj}}$. Slowly varying cross section geometries significantly increase the axial spread as dye is entrained into the recirculation cells. The typical height $L$ of the perturbation determines how far the dye spreads quickly. Only a relatively small change in section, but over a large distance can dramatically increase the axial dispersion. The influence of the slope $\epsilon$ of the perturbation itself also increases the axial spread, but not as much as $L$. The enhanced diffusion coefficient that we measured in a region away from the catheter tip in a straight annular gap is considerably higher for low $A_{\text{osc}}$ and $f_{\text{osc}}$ than according to the 1D theory, and is subject to large variations. We conclude that the enhanced diffusion model gives a reasonable first estimate of the spread that can be obtained in the absence of large steady streaming structures.

The influence of the injection velocity $Q_{\text{inj}}$ on the initial spread is rather limited, confirming that the injection jet is dominated by viscous diffusion. However, $Q_{\text{inj}}$ can still have a clinical significance. Using the mixing coefficient $\Phi$ we have shown that the initial concentration gradients are substantially higher for high $Q_{\text{inj}}$. This implies that a small section of the spinal cord would be subject to higher local concentrations of drug before it is dispersed. This observation is backed up by the parametric model for the slope of $m_{\text{CV}}$ during the injection. A low $Q_{\text{inj}}$ gives the steady streaming and enhanced diffusion more time to dilute the dye below the detection threshold of our system before it disperses.

Given the same initial conditions and geometry, $A_{\text{osc}}$ is the primary determinant of dispersion, at least in our model, because of the functional dependence of both steady streaming and enhanced mixing on this parameter. This observation is confirmed by the model for the mixing state of the CV at equal dose and the decay of mass in the control volume after the injection. The decay of $m_{\text{CV}}$ is also increased for higher $Q_{\text{inj}}$, probably because dye injected at high $Q_{\text{inj}}$ is subject to the dispersing mechanisms during a longer time. A high $Q_{\text{inj}}$ might also be more effective in slightly increasing the initial volume of dispersion, increasing the effect of enhanced diffusion.

Finally, we have commented on how low concentrations of glucose affect the dispersion. We have observed that the overall axial and azimuthal spread can be successfully increased due to buoyancy, confirming unpublished results by Bernards[5]. The $\text{Pe}_{\text{inj}}$, $A_{\text{osc}}$, and the Rayleigh number Ra will determine whereto the dye will mainly disperse with respect to the injection ports of the catheter, potentially making the site of action unpredictable. The dye remains highly concentrated for low Pe, or high $\text{Pe}_{\text{inj}}$, much more so than in dye experiments without glucose.

---

[5] Bernards showed preliminary evidence of increased dispersion inside a pig model at a meeting for European Continuing Medical Training (ECMT) in Lausanne in January 2008

# Chapter 13

# Conclusions

A clinical observation that a short bolus with a higher injection rate could provide pain relief was the principal reason for investigating the fluid mechanics of ITDD. This observation can not be explained by pharmacology. However, within the practical limits of a small patient number study, it has been confirmed multiple times. Although not completely predictable due to many uncontrolled and/or uncontrollable factors, intermediate bolus administration of bupivacaine should therefore be considered as a reasonable alternative to the slow chronic injection of drug to increase the clinical effect. The appearance of the dermatomes in this study suggests that the drugs can spread over as much as 30 cm in the CSF, but this also is unpredictable and often the spread is much smaller. Anticipating patient specific drug spread could help to determine a safe drug concentration, or even contribute to optimal pain relief. Based on the diffusivity of bupivacaine in the CSF we have concluded that molecular diffusion, in the CSF or inside the spinal cord itself, cannot explain the order of magnitude of this spread. Furthermore, the time scales of the dispersion mechanisms we have discussed (steady streaming, enhanced diffusion, etc) are much shorter than that of the clinical effect $O(30\text{ min})$. It is therefore logical to consider the drug spread in two separate steps: an initial dispersion in the CSF inside the SAS and subsequently the absorption in the spinal cord.

Except for glucose induced buoyancy, steady streaming is the mechanism that can transport the dye the furthest in the shortest time period. For oscillatory frequencies and amplitudes relevant to ITDD the typical steady streaming velocities are $\sim 1$ mm/s in slowly varying cross section annular gaps, or at the catheter tip. For clinically relevant parameters, we have shown that the steady streaming velocity is in the direction of the wider end of the channel on the midline of the geometry, and reverse near the wall. We have shown that the analytical axi-symmetric model can be successfully used to qualitatively explain the numerically calculated steady streaming in a human like geometry of the subarachnoid space. We have shown that the scalar will qualitatively follow these steady streamlines for ITDD parameters. On a clinical time scale, the height rather than the slope of the varying cross section is the determinant for spread. Therefore, small variations in the SAS cross section can be responsible for significant differences in spread between patients.

The typical mean velocities around the catheter tip are high compared to the steady streaming generated by a slowly varying cross section of the annular gap, but they are localized in a small region surrounding the tip. The steady streaming velocities at the catheter tip inside a constricted annular geometry are increased: this effect is thought to be related to, at leading order, to the RMS velocity at the tip. Steady streaming at the catheter tip is responsible for the characteristic mushroom shape of the dispersion of the dye. The specific shape is subject to the exact catheter orientation, or surrounding geometry. The shape of the catheter could be used more efficiently than is the case with commercial catheters to augment both the axial and azimuthal spread.

Compared to steady streaming, enhanced diffusion is a relatively slow mechanism $O(0.05 \text{ mm/s})$ increasing the axial spread of the dye. Importantly, enhanced diffusion substantially lowers the local concentrations gradients inside the spinal canal faster than molecular diffusion alone and is therefore clinically important. An enhanced diffusion coefficient valid for 1D enhanced mixing is $\propto \alpha A_{\text{osc}}^2$. Our attempt to measure $D_{\text{enh}}$ was subject to considerable variance and shows that this mechanism cannot be considered in isolation from steady streaming and the injection rate.

The influence of clinically used injection rates on the dispersion is limited because of viscous attenuation of the injection jet. However, we have shown with a parametric model that the decay of measured mass inside a CV, an important measure for spread, is increased for increased $Q_{\text{inj}}$. It is likely that this effect will be increased for higher injection rates. The most important influence of $Q_{\text{inj}}$ however is the initial mixing state, which is low for high injection rates. Confirming the influence of the injection Péclet number $\text{Pe}_{\text{inj}}$, it implies that the dye remains more concentrated over a longer distance for high $Q_{\text{inj}}$, and is more diffuse for low $Q_{\text{inj}}$. Assuming that a higher drug concentration in the CSF results in a higher local drug concentration at the site of action and therefore an increased clinical effect, this could explain the increased efficacy of a bolus administration of a quick acting local anesthetic.

We have investigated the effect of glucose on the dispersion and have observed that buoyancy increases the final azimuthal and axial dispersion of the dye. However, the dye can travel far before it is sufficiently diluted to disperse into a cloud. This effect is dependent on the Péclet number of the flow, the injection Péclet number $\text{Pe}_{\text{inj}}$, as well as the Rayleigh number. Although the specific site of action might be difficult to predict, it would probably be nearer the injection site for low $\text{Pe}_{\text{inj}}$, high Pe, and low concentrations of glucose. The fact that the dye remains highly concentrated before it disperses into a cloud is an important factor to take into account for the chronic administration of hyperbaric drugs.

Finally, understanding how to increase the non-dimensional amplitude of the oscillation $A_{\text{osc}}$ in a specific patient could be useful to increase drug spread, given its importance in both steady streaming and enhanced diffusion. One could imagine that patient exercise, breathing, or bending could for example be used to increase $A_{\text{osc}}$. Measuring $A_{\text{osc}}$ using MRI might be a reasonable way to predict drug spread in ITDD, especially when combined with intimate knowledge of the local, patient specific geometry of the spinal canal.

# Outlook

Despite the difficulties in obtaining quantitative results, the experimental setup is well suited to describe the dispersion as a function of the oscillation of the fluid, injection catheter and the local geometry. Due to time restrictions we have not been able to exploit the experiment to its fullest potential. More experiments should be done with for example the varying cross section geometries and glucose solutions. We have not been able to determine for example if there is an optimal position of the catheter with respect to the varying cross section geometry. Also in its present form the experimental model is an unexploited test bench for catheter prototypes. Finally, we have restricted ourselves to clinically used flow rates, but there is no reason why future ITDD pumps shouldn't be able to provide larger injection rates.

The experiment model is a relatively simple version of the subarachnoid space and could be easily developed to include more complex geometries, such as for example nerve branches. Each increase in complexity however, makes the measurement technique less accurate for dispersion measurements. An optically-matched test section and the use of (several) more precise cameras would certainly negate this effect, but would require a considerable investment in time and money. Additionally, there is a distinct lack of knowledge of the patient specific geometry of the subarachnoid space and the oscillation characteristics of the CSF. This increases the risk that a more advanced model would be only of academic interest.

# Nomenclature

## Roman letters

| | | |
|---|---|---|
| $A_{\mathrm{osc}}$ | Dimensionless peak to peak oscillation amplitude $= d_{\mathrm{osc}}/r_{\mathrm{H}}$ | |
| $a$ | Attenuation coefficient due to laser absorption | $\mathrm{m}^{-1}$ |
| $b_i$ | Calculated model coefficient, $i \in [1, N]$ | |
| $B$ | Photobleaching constant | |
| $c$ | Speed of light $3 \cdot 10^8$ | $\mathrm{m.s}^{-1}$ |
| $C$ | Concentration | $\mathrm{mg.l}^{-1}$ |
| $C_B$ | Concentration of injected bolus | $\mathrm{mg.l}^{-1}$ |
| $\langle C_{\mathrm{rms}} \rangle$ | Average root mean square concentration | mg |
| $D_{\mathrm{enh}}$ | Effective diffusion coefficient | $\mathrm{m}^2.\mathrm{s}^{-1}$ |
| $d_{\mathrm{plane}}$ | Laser plane thickness | m |
| $D$ | Molecular diffusion coefficient | $\mathrm{m}^2.\mathrm{s}^{-1}$ |
| $d_{\mathrm{osc}}$ | Peak to peak oscillation amplitude | m |
| $f_{\mathrm{osc}}$ | Frequency of oscillation | Hz |
| $F$ | Azimuthal fill factor | |
| $f_{\mathrm{T}}$ | Functional dependence enhanced mixing (Watson) | |
| $f_{\xi}$ | Function used for correction mirror acceleration | |
| $g$ | Gravitational acceleration constant | $\mathrm{m.s}^{-2}$ |
| $G$ | Functional dependence enhanced mixing (Elad et al.) | |
| $h_{\mathrm{typ}}$ | Typical height of a constant $C$ dispersion | |
| $\langle I_{\mathrm{BG}} \rangle$ | Mean pixel value of the subtracted background image | Pixel Value |
| $I_{\mathrm{f}}$ | The measured fluorescent intensity | $\mathrm{W.m}^{-2}$ |
| $I$ | Intensity | $\mathrm{W.m}^{-2}$ |
| $\langle I_{\mathrm{f}} \rangle$ | Mean pixel value of an image | Pixel Value |
| $k_q$ | Collisional quenching constant | $\mathrm{K}^{-1}$ |
| $L_c$ | Characteristic length | m |

| | | |
|---|---|---|
| $L$ | Length of the axi-symmetric perturbation | m |
| $M$ | Correction matrix for rotating mirror acceleration | |
| $k$ | The number of experiments taken into consideration | |
| $\dot{m}$ | Mass flow rate | $\mathrm{mg.s^{-1}}$ |
| $m$ | Mass | mg |
| $i, j, n, l$ | Natural number | |
| $N$ | The number of factors, or variables, included in a model | |
| $N_f$ | The number of factors, or variables varied | |
| $N_s$ | Number of scatterers | |
| $N_{\mathrm{nop}}$ | Number of planes scanned for a 3D cross section | |
| $P_0$ | Incident laser power | W |
| $p$ | Pressure | $\mathrm{kg.s^{-2}.m^{-1}}$ |
| $Q$ | Oscillatory flow rate | $\mathrm{m^3.s^{-1}}$ |
| $q$ | Diffusion flux | $\mathrm{mg.m.s^{-1}}$ |
| $Q_{\mathrm{inj}}$ | Injection rate | $\mu\mathrm{l.s^{-1}}$ |
| $\Delta r_o$ | Peak to peak amplitude of the perturbation on the outer wall | m |
| $r_{\mathrm{H}}$ | Hydraulic radius $= 3 \cdot 10^{-3}$ m | m |
| $r_i$ | Radius of the spinal cord, or of the inner wall of the annular gap | m |
| $r_o$ | Radius of the arachnoid, or of the outer wall of the annular gap $= r_o(z)$ | m |
| $S$ | Cross section of the annular gap $= \pi(r_o(z)^2 - r_i^2)$ | $\mathrm{m^2}$ |
| $s$ | Attenuation coefficient due to laser scattering | $\mathrm{m^{-1}}$ |
| $T$ | Temperature | °C |
| $V_T$ | Tidal volume $= d_{\mathrm{osc}} S$ | $\mathrm{m^3}$ |
| $V_s$ | Characteristic steady streaming velocity | $\mathrm{m.s^{-1}}$ |
| $V_B$ | Injection bolus volume | $\mu$l |
| $V_{\mathrm{vox}}$ | Voxel volume | $\mathrm{m^3}$ |
| $X_i$ | Variable, or factor $i \in [1, N_f]$ | |
| $Y$ | A response of the system. | |

| | | |
|---|---|---|
| $z_{\mathrm{ent}}$ | Scattering entrance length | m |
| $z_{\mathrm{g}}$ | Center of gravity of the axial dispersion ($\mathbf{e}_z$) | m |

**Greek letters**

| | | |
|---|---|---|
| $\beta$ | Decay coefficient for $m_{\mathrm{CV}}$ after injection | $\mathrm{s}^{-1}$ |
| $\beta^*$ | Coeficient of density variation with concentration $= (1/\rho) \cdot (\partial\rho/\partial C)$ | $\mathrm{l.mg}^{-1}$ |
| $\delta$ | A characteristic distance | m |
| $\epsilon$ | Slope of cylindrical outer wall | |
| $\varepsilon_a$ | Relative error due to attenuation of the laser beam | % |
| $\varepsilon$ | Absolute error of $m_{\mathrm{CV}}$ | mg |
| $\varepsilon_\xi$ | Relative error due to rotating mirror acceleration | % |
| $\theta_{\mathrm{g}}$ | Center of gravity of the azimuthal dispersion ($\mathbf{e}_\theta$) | m |
| $\lambda$ | Wavelength of the incident light | nm |
| $\lambda_{1/2}$ | Distance over which $I_{\mathrm{f}}$ is halved | m |
| $\nu$ | Kinematic viscosity | $\mathrm{m}^2.\mathrm{s}^{-1}$ |
| $\rho$ | Fluid density | $\mathrm{kg.m}^{-3}$ |
| $\sigma$ | Standard deviation of dye dispersion | $\mathrm{m}^2$ |
| $\tau$ | A characteristic time | s |
| $\varphi$ | Catheter orientation | rad |
| $\phi_{\mathrm{c}}$ | Diameter injection ports | m |
| $\Phi$ | Mixing parameter | |
| $\Omega$ | Solid angle | sr |
| $\omega$ | Natural frequency of oscillation | $\mathrm{rad.s}^{-1}$ |
| $\chi$ | Camera pixel width or height | m |
| $\dot{\xi}$ | Laser scan speed | $\mathrm{m.s}^{-1}$ |
| $\Psi_s$ | Non-dimensional steady streaming stream function | |

## Coordinate systems

| | | |
|---|---|---|
| $x, y, z$ | Cartesian coordinates | m |
| $r, \theta, z$ | Cylindrical coordinates | m,rad,m |
| $r_{\mathrm{im}}, \theta_{\mathrm{im}}$ | Polar coordinates with respect to the camera axis ($\mathbf{e}_x$) | m,rad |
| $t$ | Time | s |

## Velocity

| | | |
|---|---|---|
| $(U, V, W)$ | Spatial dependence of velocity | $\mathrm{m.s}^{-1}$ |
| $\mathbf{v_s} = \begin{pmatrix} u_s \\ v_s \\ w_s \end{pmatrix}$ | Steady first order velocity (steady streaming) | $\mathrm{m.s}^{-1}$ |
| $\mathbf{v_{us}} = \begin{pmatrix} u_{us} \\ v_{us} \\ w_{us} \end{pmatrix}$ | Unsteady first order velocity in cylindrical coordinates | $\mathrm{m.s}^{-1}$ |
| $\mathbf{v} = \begin{pmatrix} u \\ v \\ w \end{pmatrix}$ | Fluid velocity | $\mathrm{m.s}^{-1}$ |

## Dimensionless Numbers

| | |
|---|---|
| $\alpha$ | Womersley number $= r_{\mathrm{H}}\sqrt{\frac{\omega}{\nu}}$ |
| Ra | Rayleigh number $= g\beta^{*}\Delta C r_{\mathrm{H}}^{3}/(\nu D)$ |
| Re | Reynolds number $= \alpha^{2} A_{\mathrm{osc}}$ |
| $\mathrm{Re}_{\mathrm{inj}}$ | Injection Reynolds number $= Q_{\mathrm{inj}}/(\phi_{\mathrm{c}} D A_{\mathrm{osc}})$ |
| $\mathrm{Re}_{\mathrm{s}}$ | Steady streaming Reynolds number $= \alpha^{2} A_{\mathrm{osc}}^{2}$ |
| Gr | Grashof number $\equiv \mathrm{Ra}/\mathrm{Sc} = g\beta^{*}\Delta C r_{\mathrm{H}}^{3}/\nu^{2}$ |
| Pe | Péclet number $\equiv \mathrm{ReSc} = \alpha^{2} A_{\mathrm{osc}}\mathrm{Sc}$ |
| $\mathrm{Pe}_{\mathrm{inj}}$ | Péclet number for injection of scalar $= Q/(\phi_{\mathrm{c}} D)$ |
| $\mathrm{Pe}^{*}$ | Modified Péclet number $= (\alpha/A_{\mathrm{osc}})\mathrm{Sc}$ |
| Sc | Schmidt number $= \nu/D$ |

### Mathematical conventions

| | |
|---|---|
| $\mathbf{v}$ | 2, or 3D Vector |
| $\mid\ \mid$ | Vector norm |
| $\bar{\ }$ or $\langle\ \rangle$ | Average |
| $\hat{\ }$ | Dimensional variable |

### Abbreviations

| | |
|---|---|
| CNS | Central nervous system |
| CSF | Cerebrospinal fluid |
| CV | Control volume |
| ITDD | Intrathecal drug delivery |
| LA | Local anesthetic |
| LIF | Laser induced fluorescence |
| PIV | Particle image velocimetry |
| RMS | Root mean square |
| SAS | Subarachnoid space |
| SNR | Signal to noise ratio |

# Bibliography

[1] R. Abu-Gharbieh, J. L. Persson, M. Forsth, A. Rosen, A. Karlstrom, and T. Gustavsson. Compensation method for attenuated planar laser images of optically dense sprays. *Applied Optics*, 39(8):1260–1267, March 2000.

[2] J. W. Allen, K. A. Horais, N. A. Tozier, K. Wegner, J. A. Corbeil, R. F. Mattrey, S. S. Rossi, and T. L. Yaksh. Time course and role of morphine dose and concentration in intrathecal granuloma formation in dogs - a combined magnetic resonance imaging and histopathology investigation. *Anesthesiology*, 105(3):581–589, September 2006.

[3] R. Aris. On the dispersion of a solute in a fluid flowing through a tube. *Proceedings Of The Royal Society Of London Series A-Mathematical And Physical Sciences*, 235(1200):67–77, 1956.

[4] J. Bannister, J. H. McClure, and J. A. W. Wildsmith. Effect of glucose-concentration on the intrathecal spread of 0.5-percent bupivacaine. *British Journal Of Anaesthesia*, 64(2):232–234, February 1990.

[5] N. G. Barton. Dispersion of a buoyant solute in laminar-flow in a straight horizontal pipe .2. approach to asymptotic state. *Journal Of Fluid Mechanics*, 74(MAR9):91–112, 1976.

[6] C. M. Bernards. Cerebrospinal fluid and spinal cord distribution of baclofen and bupivacaine during slow intratbecal infusion in pigs. *Anesthesiology*, 105(1):169–178, July 2006.

[7] R. A. Bhadelia, A. R. Bogdan, and S. M. Wolpert. Analysis of cerebrospinal-fluid flow wave-forms with gated phase-contrast mr velocity-measurements. *American Journal Of Neuroradiology*, 16(2):389–400, February 1995.

[8] I. G. Bloomfield, I. H. Johnston, and L. E. Bilston. Effects of proteins, blood cells and glucose on the viscosity of cerebrospinal fluid. *Pediatric Neurosurgery*, 28(5):246–251, May 1998.

[9] G.E.P. Box, W.J. Hunter, and J. Hunter. *Statistics for Experimenters, An Introduction to Design, Data Analysis and Model Building.* Wiley Series in Probability and Mathematical Statistics. J. Wiley & Son, 1978.

[10] F. Brouneus, K. Karami, P. Beronius, and L. O. Sundelof. Diffusive transport properties of some local anesthetics applicable for iontophoretic formulation of the drugs. *International Journal Of Pharmaceutics*, 218(1-2):57–62, May 2001.

[11] E. Buchser, A. Durrer, D. Chedel, and J. P. Mustaki. Efficacy of intrathecal bupivacaine: How important is the flow rate? *Pain Medicine*, 5(3):248–252, September 2004.

[12] K. L. Cabbell, J. A. Taren, and O. Sagher. Spinal cord compression by catheter granulomas in high-dose intrathecal morphine therapy: Case report. *Neurosurgery*, 42(5):1176–1180, May 1998.

[13] P. C. Chatwin. Longitudinal dispersion of passive contaminant in oscillatory flows in tubes. *Journal Of Fluid Mechanics*, 71(OCT14):513–527, 1975.

[14] Z. J. Chen, G. T. Gillies, W. C. Broaddus, S. S. Prabhu, H. Fillmore, R. M. Mitchell, F. D. Corwin, and P. P. Fatouros. A realistic brain tissue phantom for intraparenchymal infusion studies. *Journal Of Neurosurgery*, 101(2):314–322, August 2004.

[15] E.F.F Chladni. *Die Akustik*. Breitkoph und H artel, 1802.

[16] D. W. Coombs, R. L. Saunders, M. S. Gaylor, M. G. Pageau, M. G. Leith, and C. Schaiberger. Continuous epidural analgesia via implanted morphine reservoir. *Lancet*, 2(8243):425–426, 1981.

[17] G. Cruccu, P. Anand, N. Attal, L. Garcia-Larrea, M. Haanpaa, E. Jorum, J. Serra, and T. S. Jensen. Efns guidelines on neuropathic pain assessment. *European Journal Of Neurology*, 11(3):153–162, March 2004.

[18] T. R. Deer, L. J. Raso, and T. G. Garten. Inflammatory mass of an intrathecal catheter in patients receiving baclofen as a sole agent: A report of two cases and a review of the identification and treatment of the complication. *Pain Medicine*, 8(3):259–262, April 2007.

[19] S. Deusch and T. Dracos. Time resolved 3d passive scalar concentration-field imaging by laser induced fluorescence (lif) in moving liquids. *Measurement Science & Technology*, 12(2):188–200, February 2001.

[20] I. Dobos, K. Toth, G. Kekesi, G. Joo, E. Csullog, W. Klimscha, G. Benedek, and G. Horvath. The significance of intrathecal catheter location in rats. *Anesthesia And Analgesia*, 96(2):487–492, February 2003.

[21] D. Elad, D. Halpern, and J. B. Grotberg. Gas dispersion in volume-cycled tube flow. i. theory. *J Appl Physiol*, 72(1):312–320, Jan 1992.

[22] M. E. Erdogan and P. C. Chatwin. Effects of curvature and buoyancy on laminar dispersion of solute in a horizontal tube. *Journal Of Fluid Mechanics*, 29:465–&, 1967.

[23] M. Faraday. On a peculiar class of acoustical figures; and on certain forms assumed by groups of particles upon vibrating elastic surfaces. *Philosophical Transactions of the Royal Society of London*, 121:299–340, 1831.

[24] D. P. Gaver, J. Solway, N. Punjabi, D. Elad, J. B. Grotberg, and N. Gavriely. Gas dispersion in volume-cycled tube flow .2. tracer bolus experiments. *Journal Of Applied Physiology*, 72(1):321–331, January 1992.

[25] W. N. Gill and Sankaras.R. Exact analysis of unsteady convective diffusion. *Proceedings Of The Royal Society Of London Series A-Mathematical And Physical Sciences*, 316(1526):341–&, 1970.

[26] W. N. Gill and Sankaras.R. Dispersion of a non-uniform slug in time-dependent flow. *Proceedings Of The Royal Society Of London Series A-Mathematical And Physical Sciences*, 322(1548):101–&, 1971.

[27] I. S. Goldberg, Z. Q. Zhang, and M. Tran. Steady streaming of fluid in the entrance region of a tube during oscillatory flow. *Physics Of Fluids*, 11(10):2957–2962, October 1999.

[28] H. Gray. *Anatomy of the Human Body.* Philadelphia: Lea & Febriger; Bartleby.com, 20 edition, May 2000.

[29] A. Griffiths. On the movement of a coloured index along a capillary tube, and its application to the measurement of the circulation of water in a closed circuit. *Proceedings Of The Physical Society Of London*, 23:190–197, 1911.

[30] J. B. Grotberg. Volume-cycled oscillatory flow in a tapered channel. *Journal Of Fluid Mechanics*, 141(APR):249–264, 1984.

[31] P. Hall. Unsteady viscous-flow in a pipe of slowly varying cross-section. *Journal Of Fluid Mechanics*, 64(JUN19):209–226, 1974.

[32] H. G. Harris and S. L. Goren. Axial diffusion in a cylinder with pulsed flow. *Chemical Engineering Science*, 22(12):1571–&, 1967.

[33] S. J. Hassenbusch and R. K. Portenoy. Current practices in intraspinal therapy - a survey of clinical trends and decision making. *Journal Of Pain And Symptom Management*, 20(2):S4–S11, August 2000.

[34] S. J. Hassenbusch, W. C. Satterfield, and T. L. Gradert. A sheep model for continuous intrathecal infusion of test substances. *Human & Experimental Toxicology*, 18(2):82–87, February 1999.

[35] H. M. Hertz and M. Alden. Calibration of imaging laser-induced fluorescence measurements in highly absorbing flames. *Applied Physics B-Photophysics And Laser Chemistry*, 42(2):97–102, February 1987.

[36] G. Hocking and J. A. W. Wildsmith. Intrathecal drug spread. *British Journal Of Anaesthesia*, 93(4):568–578, October 2004.

[37] P. E. Hydon and T. J. Pedley. Axial-dispersion in a channel with oscillating walls. *Journal Of Fluid Mechanics*, 249:535–555, April 1993.

[38] R. I. Issa, B. Ahmadibefrui, K. R. Beshay, and A. D. Gosman. Solution of the implicitly discretized reacting flow equations by operator-splitting. *Journal Of Computational Physics*, 93(2):388–410, April 1991.

[39] T. Kameyama, Y. Hashizume, and G. Sobue. Morphologic features of the normal human cadaveric spinal cord. *Spine*, 21(11):1285–1290, June 1996.

[40] J. L. Kinsey. Laser-induced fluorescence. *Annual Review Of Physical Chemistry*, 28:349–372, 1977.

[41] L. G. Larsen and J. P. Crimaldi. The effect of photobleaching on plif. *Experiments In Fluids*, 41(5):803–812, November 2006.

[42] F. Loth, M. A. Yardimci, and N. Alperin. Hydrodynamic modeling of cerebrospinal fluid motion within the spinal cavity. *Journal Of Biomechanical Engineering-Transactions Of The Asme*, 123(1):71–79, February 2001.

[43] M. L. Lowe and P. H. Kutt. Refraction through cylindrical-tubes. *Experiments In Fluids*, 13(5):315–320, September 1992.

[44] M. J. Manton. Low reynolds number flow in slowly varying axisymmetric tubes. *Journal Of Fluid Mechanics*, 49(OCT15):451–&, 1971.

[45] G. A. McLeod. Density of spinal anaesthetic solutions of bupivacaine, levobupivacaine, and ropivacaine with and without dextrose. *British Journal Of Anaesthesia*, 92(4):547–551, April 2004.

[46] V. J. Miele, K. O. Price, S. Bloomfield, J. Hogg, and J. E. Bailes. A review of intrathecal morphine therapy related granulomas. *European Journal Of Pain*, 10(3):251–261, April 2006.

[47] Y. E. Mironer, J. C. Haasis, I. Chapple, C. Brown, and J. R. Satterthwaite. Efficacy and safety of intrathecal opioid/bupivacaine mixture in chronic nonmalignant pain: A double blind, randomized, crossover, multicenter study by the national forum of independent pain clinicians (nfipc). *Neuromodulation*, 5(4):208–213, October 2002.

[48] C. Muhle, J. Wiskirchen, D. Weinert, A. Falliner, F. Wesner, G. Brinkmann, and M. Heller. Biomechanical aspects of the subarachnoid space and cervical cord in healthy individuals examined with kinematic magnetic resonance imaging. *Spine*, 23(5):556–567, Mar 1998.

[49] P. M. Murphy and M. J. Cousins. *The Paths of Pain : 1975-2005*, chapter Neural Blockade and Neuromodulation in Persistent Pain Management, pages 471–468. IASP Press, 2005.

[50] C. Nicholson. Diffusion and related transport mechanisms in brain tissue. *Reports On Progress In Physics*, 64(7):815–884, July 2001.

[51] R.A. Rao and R. Devanathan. Pulsatile flow in tubes of varying cross-sections. *Zeitschrift Fur Angewandte Mathematik Und Physik*, 24(2):203–213, 1973.

[52] Lord Rayleigh. On the circulation of air observed in kundt's tubes, and on some allied acoustical problems. *Philosophical Transactions of the Royal Society of London*, 175:1–21, 1884.

[53] M. L. Rigler and K. Drasner. Distribution of catheter-injected local-anesthetic in a model of the subarachnoid space. *Anesthesiology*, 75(4):684–692, October 1991.

[54] N. Riley. Steady streaming. *Annual Review Of Fluid Mechanics*, 33:43–65, 2001.

[55] R. A. Robinson, S. F. C. Stewart, M. R. Myers, L. F. Llien, J. R. Rinaldi, J. L. Swisher, and K. Drasner. In-vitro modeling of spinal-anesthesia - a digital video image-processing technique and its application to catheter characterization. *Anesthesiology*, 81(4):1053–1060, October 1994.

[56] D. Rockwell, C. Magness, J. Towfighi, O. Akin, and T. Corcoran. High image-density particle image velocimetry using laser scanning techniques. *Experiments In Fluids*, 14(3):181–192, January 1993.

[57] B. K. Ross, B. Coda, and C. H. Heath. Local-anesthetic distribution in a spinal model - a possible mechanism of neurologic injury after continuous spinal-anesthesia. *Regional Anesthesia*, 17(2):69–77, March 1992.

[58] A. Sarkar and G. Jayaraman. Correction to flow rate - pressure drop relation in coronary angioplasty: steady streaming effect. *Journal Of Biomechanics*, 31(9):781–791, September 1998.

[59] M. Sarntinoranont, R. K. Banerjee, R. R. Lonser, and P. F. Morrison. A computational model of direct interstitial infusion of macromolecules into the spinal cord. *Annals Of Biomedical Engineering*, 31(4):448–461, 2003.

[60] L. Saroul, S. Gerlach, and R.D. Hersch. Exploring curved anatomic structures with surface sections. In *VIS '03: Proceedings of the 14th IEEE Visualization 2003 (VIS'03)*, page 5, Washington, DC, USA, 2003. IEEE Computer Society.

[61] J. R. Saylor. Photobleaching of disodium fluorescein in water. *Experiments In Fluids*, 18(6):445–447, April 1995.

[62] H Schlichting and K Gersten. *Boundary Layer Theory.* Springer, 8th revised edition, 2000.

[63] M. K. Sharp, R. D. Kamm, A. H. Shapiro, E. Kimmel, and G. E. Karniadakis. Dispersion in a curved tube during oscillatory flow. *Journal Of Fluid Mechanics*, 223:537–563, February 1991.

[64] R. Smith. Contaminant dispersion in oscillatory flows. *Journal Of Fluid Mechanics*, 114(JAN):379–398, 1982.

[65] V. M. Spitzer, D. Whitlock, A. L. Scherzinger, and M. J. Ackerman. The visible-human (male and female). *Radiology*, 197:533–533, November 1995.

[66] J. T. Stuart. Double boundary layers in oscillatory viscous flow. *Journal Of Fluid Mechanics*, 24:673–&, 1966.

[67] J. K. Sveen. An introduction to matpiv v.1.6.1. Eprint no. 2, **ISSN** 0809-4403, Dept. of Mathematics, University of Oslo, 2004. http://www.math.uio.no/~jks/matpiv.

[68] G. Taylor. Dispersion of soluble matter in solvent flowing slowly through a tube. *Proceedings Of The Royal Society Of London Series A-Mathematical And Physical Sciences*, 219(1137):186–203, 1953.

[69] X. D. Tian and P. J. W. Roberts. A 3d lif system for turbulent buoyant jet flows. *Experiments In Fluids*, 35(6):636–647, December 2003.

[70] T.-V. Truong and P.A. Monkewitz. Preliminary laboratory study of drug dispersion in csf. Technical report, Laboratory of Fluid Mechanics, EPFL, 2002.

[71] S. Tsangaris and N. Athanassiadis. Diffusion in oscillatory flow in an annular pipe. *Zeitschrift Fur Angewandte Mathematik Und Mechanik*, 65(4):T252–T254, 1985.

[72] W. C. Ummenhofer, R. H. Arends, D. D. Shen, and C. N. Bernards. Comparative spinal distribution and clearance kinetics of intrathecally administered morphine, fentanyl, alfentanil, and sufentanil. *Anesthesiology*, 92(3):739–753, March 2000.

[73] J. W. van Bodegom, J. W. Kuiper, R. R. van Rijn, C. van Kuijk, A. W. Zwamborn, and J. L. Grashuis. Vertebral dimensions: Influence of x-ray technique and patient size on measurements. *Calcified Tissue International*, 62(3):214–218, March 1998.

[74] M. P. Vercauteren, H. C. Coppejans, V. L. Hoffmann, V. Saldien, and H. A. Adriaensen. Small-dose hyperbaric versus plain bupivacaine during spinal anesthesia for cesarean section. *Anesthesia And Analgesia*, 86(5):989–993, May 1998.

[75] M. Versluis, N. Georgiev, L. Martinsson, M. Alden, and S. Kroll. 2-d absolute oh concentration profiles in atmospheric flames using planar lif in a bi-directional laser beam configuration. *Applied Physics B-Lasers And Optics*, 65(3):411–417, September 1997.

[76] G. M. Villegas and J. Fernández. Permeability to thorium dioxide of intercellular spaces of frog cerebral hemisphere. *Experimental Neurology*, 15(1):18–&, 1966.

[77] E. J. Watson. Diffusion in oscillatory pipe-flow. *Journal Of Fluid Mechanics*, 133(AUG):233–244, 1983.

[78] J. R. Womersley. Oscillatory motion of a viscous liquid in a thin-walled elastic tube .1. the linear approximation for long waves. *Philosophical Magazine*, 46(373):199–221, 1955.

[79] T. L. Yaksh, K. A. Horais, N. A. Tozier, J. W. Allen, M. Rathbun, S. S. Rossi, C. Sommer, C. Meschter, P. J. Richter, and K. R. HIldebrand. Chronically infused intrathecal morphine in dogs. *Anesthesiology*, 99(1):174–187, July 2003.

# Curriculum Vitae

## Contact Information

Radboud Nelissen
Avenue Vinet 33/4
1004 Lausanne
Switzerland

March 22nd, 1977
*Mobile:* +41(0)76 5081751
*Work:* +41(0)21 6933365
*E-mail:* radboud.nelissen@epfl.ch

## Education

| | |
|---|---|
| 2004 – present | PhD. at the École Polytechnique Fédérale de Lausanne (EPFL), Switzerland, Laboratory of Fluid Mechanics (LMF).<br>*Title*: “Fluid Mechanics of Intrathecal Drug Delivery”<br>*Advisor*: Prof. P.A. Monkewitz |
| 1996 – 2002 | MSc. at the University of Twente, Enschede, The Netherlands, Faculty of Applied Physics, Chair of Fluid Dynamics and Heat Transfer.<br>*Title*: “The Optical and Acoustic Analysis of Ultrasound Contrast Agents”<br>*Advisors*: Prof. D. Lohse and Dr. M. Versluis |

## Scientific Contributions

### Conference Presentations

[C1] Nelissen, R., Borhani, N., Buchser, E., Monkewitz, P., “An Experimental Investigation of Mixing Phenomena in Intrathecal Drug Delivery (ITDD)”. Summer Bioengineering Conference (SBC), Amelia Island Plantation, Florida, USA, June 2006 (presenting author).

[C2] Nelissen, R., Koene, E., Hilgenfeldt, S., Versluis, M., “Mie Scattering Of Coated Microbubbles”. Pan American/Iberian Meeting of Acoustics, Cancun, Mexico, November 2002.

[C3] Versluis, M., Nelissen, R., Schmitz, B., Lohse, D., “Shrimpoluminescence”. 54th APS Division of Fluid Mechanics annual meeting, San Diego, USA, November 2001.

### Invited Talks

[T1] European Continuing Medical Training (ECMT), “Latest Perspectives On Intrathecal Drug Delivery for the Management of Chronic Pain”, Lausanne, Switzerland (January 2008, December 2006, December 2005).

[T2] Annual Meeting of the Leonard Euler Center Swiss ERCOFTAC Pilot Center, Institute of Fluid Dynamics (IFC), ETH Zentrum, Zurich, Switzerland (2005).

## Posters

[P1] CTI Medtech Event, Inselspital Berne, Kinderklinik, Bern, Switzerland (2007, 2006, and 2005).

[P2] Nelissen, R., Buchser, E., Borhani, N., Durrer, A., Menoud, C., Monkewitz, P., Rutschmann, B., Acone, S., Albrecht, E., “An Experimental Investigation into Drug Dispersion in the Intrathecal Space”. 11th World Congress on Pain, International Association for the Study of Pain (IASP), Sydney, Australia (August 2005).